Sapienza - Università di Roma

DOTTORATO DI RICERCA IN

TECNOLOGIE DELL'INFORMAZIONE E DELLE COMUNICAZIONI

Curriculum in Radar and Remote Sensing

Ciclo XXX

Settore Concorsuale di afferenza: 09/F2 - TELECOMUNICAZIONI

Settore Scientifico disciplinare: ING-INF/03

Assessment of the ionospheric impact on Synthetic Aperture RADAR imaging

Presentata da: Elvira Musicò

Coordinatore Dottorato	**Relatore**
Prof.ssa Maria Gabriella Di Benedetto	Dott.ssa Giorgiana De Franceschi
	Co-Relatore
	Dott. Roberto Seu

Esame finale anno 2017

Abstract

Synthetic Aperture Radar (SAR) is the key-technology for the Earth's Observation from space, enabling the imaging of our planet under any atmospheric condition and, being an active instrument, all day long, as it is independent on the sunlight. At least a pair of SAR images, of the same portion of the Earth's surface, can be used to form a phase difference image that is called "interferogram". This technique, known as the Interferometric Synthetic Aperture RADAR (InSAR), is among the most used techniques for geophysical applications, providing maps of, e.g., surface deformation with high accuracy (mm level). The ionosphere affects space-borne SAR measurements especially at lower frequencies: free electrons and ions modify phase and group velocities as well as the intensity and polarization of the SAR transmitted electromagnetic waves crossing the ionospheric plasma. Such modifications introduce errors in SAR products, and, vice versa, they can provide information on the ionospheric conditions during the image acquisition. These errors are function of the Total Electron Content (TEC), i.e. the columnar concentration of free electrons along the satellite-target path. TEC is a highly variable quantity influenced by several helio-geophysical parameters, such as the solar activity and the geomagnetic field conditions; moreover, it depends on the latitude, on the season and on the time of the day.

This thesis has a twofold scope: evaluating the ionospheric impact on InSAR imaging and assessing the capability of InSAR to retrieve ionospheric information. To the scope, mid-latitude, night-time case studies, are selected to investigate on the correlation between TEC temporal and spatial variability derived from InSAR and from a dense regional network of GNSS (Global Navigation Satellite Systems) receivers over Italy. To retrieve the TEC variability from InSAR, the correlation is investigated between the integral of the azimuth shifts and the interferometric phase in the absence of ground motions (e.g. earthquakes) and/or heavy rain events. If correlation exists, the tropospheric contribution to the interferometric phase is assumed constant and the TEC variability from In-SAR can be retrieved. This assumption is further supported by the correlation results between the TEC from InSAR and from GNSS, allowing also the use of TEC from GNSS to mitigate the phase advance introduced by the ionosphere. Moreover, the careful characterization of the geomagnetic and ionospheric conditions, carried out for the case studies under investigation, shows that a particular electron density formation in the ionosphere named sporadic E layer, looks like the main responsible of the "strikes" occurrence.

The novelty of this work lies in trying to go beyond the current approaches in dealing with the ionospheric effects on SAR, usually based on the use of global ionospheric models, and to provide insights about the possibility to retrieve ionospheric information from SAR.

Keywords: Ionosphere, TEC, SAR, ALOS-PALSAR, phase advance, azimuth shift

Acknowledgements

Index

List of figures

List of tables

1 INTRODUCTION

Remote sensing plays an increasingly important role in study and monitoring the Earth's surface and atmosphere. Optical remote sensing systems need sunlight to make observations because they capture the radiances coming from the Earth and/or from the atmosphere illuminated by the Sun. Moreover, the presence of clouds limits the observation capability, because they are impenetrable by the visible, ultraviolet, and infrared light. On the contrary, active remote sensing systems, that use the microwave bandwidth, can observe Earth's surface independently on presence of the Sun and in any atmospheric conditions. In this kind of systems, the antenna transmits the radio signal and records the echo backscattered by the target. From the characteristics of the backscattered signal, it is possible to extract information about the electrical properties and the position of the scatters. This kind of system is called RADAR (RAdio Detection And Ranging), and provides an image, that is a matrix of complex numbers defined by the amplitude and phase of the backward diffused echoes. Among the RADAR systems, the Synthetic Aperture Radar (SAR) is particularly important to detect the geophysical parameter of interest. SAR, indeed, exploiting the Doppler effect due to the motion of the platform (airplane or satellite), allows obtaining high spatial resolution images along the direction of flight. Furthermore, SAR allows obtaining high spatial resolution also in the range direction (the direction perpendicular to flight path), by transmitting chirp signals. At least two SAR images, a "master" and a "slave" acquired over the same area, must be used to generate an interferogram, i.e. a phase difference image. This widely used technique is the Interferometric Synthetic Aperture RADAR (InSAR) and it allows retrieving information about the targets displacement between the acquisition times. The atmosphere (troposphere and ionosphere) crossed by the electromagnetic signal influences the accuracy of low frequency space-borne SAR measurements, leading to an additional phase contribution to the interferogram and, consequently, to an error in the displacement measurement [1]. This additional atmospheric phase is the sum of two different terms: the tropospheric phase delay and the ionospheric phase advance [2]. The ionospheric introduced error is a function of the Total Electron Content (TEC) which quantifies the columnar density of free electrons along the satellite-target path. [3]

1.1. State of the Art

In 1999, Liu et al. simulated the degradation of SAR image due to the ionosphere assuming two ionospheric scenarios: a linear distribution and a Gaussian distribution of TEC over the synthetic aperture [4]. In the same period, Gray et al. demonstrated that along-track changes in the ionospheric medium can affect not only the phase but also can lead to an azimuth shift of the pixel in the SAR image [5] [6] [7]. For a single SAR image, the azimuth shifts are a marginal error, but in the case of InSAR image, they become more important. If the ionosphere changes between master and slave acquisitions, a coregistration offset is induced [8]. This effect, known as "azimuth streaking", is responsible of the appearance of streaks on SAR coregistration images and it is proportional to the ionospheric TEC

1

gradients [9]. Furthermore, it was demonstrated that along-track tropospheric changes can add only a constant azimuth shift ([5], [6] , [7]) of the pixel location and can therefore be neglected [10]. Several studies to correct these two ionospheric effects on SAR (the Faraday rotation will not discuss in this study) have been carried out:

- the "range split-spectrum" method ([11], [12], [13]) that makes use of a bandpass filter to separate the ionospheric contribution (that is frequency dependent) to the interferometric phase from the non-dispersive term;
- the "range group-phase delay difference" method ([10], [14]), which identifies the ionospheric error exploiting the sign difference between the ionospheric phase and group delay.
- the "azimuth shift" method that exploits the relationship between the azimuth displacement and the derivative of InSAR ionospheric phase along the azimuth direction to identify and/or to estimate the ionospheric effect ([7], [15] and [9]);

The first two methods may present some criticalities when dealing with low range bandwidth. On the other side, GNSS techniques provide an external information that can be of great support to SAR. This has been also stressed during the 10th International Workshop on "Advances in the Science and Applications of SAR Interferometry and Sentinel-1 InSAR", FRINGE 2017 (http://fringe.esa.int/), in which the need to join the SAR and GNSS communities has arisen. This link between the two communities enables deeper investigations of these effects and the evaluation of the possible use of InSAR to support ionospheric studies.

This thesis is the result of the synergic collaboration between SAR experts and ionosphere experts in creating a bridge able to address both aspects.

1.2. Objectives

Even though the interest about the ionospheric effect on SAR is growing fast in the recent years, especially in view of the future Earth's observation mission (Table 3-2), most of them do not use independent measurements, like those derived from GNSS signals, to correct the interferometric phase. The GNSS signals are considered an excellent means to study and characterize the ionospheric medium as they allow determining TEC with very high temporal resolution (from 30 to 1 seconds).

In this thesis, an original approach to study the ionospheric effect on SAR, based on accurate ionospheric characterization by means of regional GNSS network data is proposed. To mitigate or even correct the errors induced by the ionosphere, it is necessary to assess the ionospheric variability with spatial and temporal resolutions as higher as possible [16]. Then, high spatial resolution maps of TEC temporal variation are produced and the relationship between TEC temporal variations measurements from regional GNSS networks, considered as the reference "true" ionosphere, and from InSAR is investigated to deliver information potentially useful to:

1. develop a method able to mitigate the ionospheric error on InSAR image;
2. assess the possibility of using the interferometric measurements to improve the ionospheric TEC evaluation.

The thesis is divided into seven chapters, among which the first four chapters are propaedeutic to introduce the objectives of the undertaken research. Chapter 2 describes the main features of the ionized atmosphere, with particular focus on the mid-latitudes. Chapter 3 gives an overview of the instruments and of the techniques used. In particular, section 3.1 introduces the SAR system and the image formation together with the InSAR principles and techniques. Section 3.2 deals with the use of GNSS receivers to study the morphology and the dynamics of the ionosphere in terms of TEC. Chapter 4 describes the ionospheric effects on InSAR images. Chapter 5 describes in details the methodology adopted and chapter 6 describes the results obtained. Finally, chapter 7 critically discusses the results, highlighting the advancement provided and the new issues emerged.

2 THE IONOSPHERE

This chapter summarizes the basic principles of the ionospheric physics, focusing mainly on the mid-latitude ionosphere. In the specific, the physical aspects of the ionosphere formation are introduced in sections 2.1, 2.2 and 2.3. Then, its structure and regular variations are provided in sections 2.4 and 2.5 (including subsections). Finally, emphasis is given to the ionospheric disturbances that may affect the propagation of trans-ionospheric waves at mid-latitudes, as they are of interest in this study (section 2.6, including subsections).

Generally, it is assumed that the upper atmosphere behaves like an ideal gas in hydrostatic equilibrium. Increasing the altitude, the pressure and density of neutral components decrease. The pressure variation with the height can be described by the hydrostatic equation:

$$\frac{dP}{dh} = -nmg,$$

2-1

where P is the pressure, h is the height, n is the number of molecules, m is the mass of each molecule and g is the acceleration of gravity.

Exploiting the ideal gas law:

$$P = nKT,$$

2-2

in which K is the Boltzmann constant[1], T is the temperature, it is possible to rewrite 2.1 as follows:

$$\frac{dP}{dh} = -PH,$$

2-3

in which $H=KT/mg$ is the scale height.

The ionosphere is the upper part of the Earth's atmosphere, starting from about 50 km of altitude, where the concentration of free electrons and ions is such to modify the propagation of radio waves. The ionosphere is produced by the solar radiation, which dissociates and ionizes the gas mixture present in the upper atmosphere. The coexistence of electric charges and atmospheric neutral gases makes the ionosphere a partially ionized[2], collision and low energy (with thermal energy of few eV) plasma, in which the electronic density, N_e, varies with altitude, latitude, seasons, hours of day and solar activity. N_e is assumed as a characteristic parameter of the ionosphere due the quasi-neutrality of the plasma (it is completely analogous to referring to ions or electrons). N_e is the result of a dynamic equilibrium between electronic production processes, loss and transport of electrons [17] and it is possible to describe its variations through the continuity equation:

---

[1] K=1.38064852 × 10^{-23} J/K
[2] Plasma is defined as an ionized gas characterized by a collective behaviour that tends to maintain, in a stationary state, the neutrality of charge.

$$\frac{\partial N_e}{\partial t} = q - L - \vec{\nabla} \cdot (N_e \vec{w}) ,\qquad\qquad 2\text{-}4$$

where q is the rate of electron production (number of electrons produced per unit of volume and per unit of time), L is the loss rate (number of electrons lost per unit of volume and per unit of time) and the last term is the and transport of electron where $\vec{w}$ is the electron drift velocity. To better understand what are the processes that affect the morphology and the variability of the ionosphere, it is necessary to explain the terms that appear to the right in equation 2-4.

2.1. Electronic production

Electronic production, expressed by the variable q, is the result of the effect of two distinct sources of ionization: *i)* photoionization by solar radiation in ultraviolet and X bands, *ii)* ionization by collision with energy particles.

If a solar photon of energy $h\nu >> E_{ion}$ (where $h=6.63\cdot10^{-34}$ is the Planck constant, ν is the frequency of incident radiation and E_{ion} is the ionization energy of the atom or the molecule) hits an atom or a molecule of the atmosphere, an electron can be lost. This process, known as photoionization, is the most common in producing free electrons in the atmosphere, especially at low and mid-latitudes. The photon-atom interaction can be sketched as a collision between two bodies, so the production rate of an ion-electron pair can be expressed as the product of four terms:

$$q = \eta n \sigma I ,\qquad\qquad 2\text{-}5$$

where η is the ionization efficiency, σ is the absorption cross section, I is the intensity of ionizing radiation at a certain atmospheric point, n is the concentration of atoms or molecules that can be ionized by I.

Starting from equation 2-5, Chapman, in 1931, developed an expression for the photoionization rate as a function of altitude, z, and solar zenith angle, χ, also known as *Chapman's production function*, able to predict the daytime variation of an ionospheric layer.

Chapman's theory is based on the following assumptions:

- atmosphere composed of a single gas, whose density varies according to barometric formula 2-3 with a constant scale height, H;
- atmosphere stratified;
- absorption of solar radiation proportional to the density of gas particles present;
- constant absorption coefficient, i.e. monochromatic radiation and only one absorbent component.

Under these assumptions, the photoionization rate $q\,(z)$ becomes:

$$q(z) = q_{m0} exp(1 - z - sec\chi \cdot e^{-z}),\qquad\qquad 2\text{-}6$$

where q_{m0} is the maximum of electronic production when the Sun is on the vertical, z is given by the difference between the height, h, and the one in which q_{m0} is located, h_{mo}, normalized with respect to H, $z = (h-h_{mo})/H$.

2.2. Electron loss for recombination and attachment

The two main processes of electron loss in the ionosphere are recombination and attachment. Recombination can be described as follows:

$$X^+ + e^- \rightarrow X,$$
2-7

where X^+ is a generic positive ion and e^- is the electron.
The loss rate, L, due to the recombination is:

$$L = \alpha[X^+]N_e = \alpha N_e{}^2,$$
2-8

In which α is the recombination coefficient, $[X^+]$ is the concentration of positive ions, that was here set equal to N_e to keep the plasma properties of the ionosphere.
By imposing equilibrium in equation 2-4 and neglecting the term of transport, the production factor is given by:

$$q = \alpha N_e{}^2.$$
2-9

From this equation, it can be easily derived that at low ionospheric altitudes, where the recombination is the prevailing mechanism of plasma loss, the electron density is:

$$N_e = \left(\frac{q}{\alpha}\right)^{1/2}.$$
2-10

The attachment of electrons by neutral atoms or molecules, M, is another factor of loss:

$$M + e^- \rightarrow M^-$$
2-11

In this case, the loss rate is given by the product of the attachment coefficient, β, with the electron density:

$$L = \beta N_e.$$
2-12

2.3. Electron transport

The last term that appears to the right in the continuity equation 2-4 is due to the variation of electronic density caused by the ionospheric plasma motion. Assuming that electron production and loss terms are negligible compared to vertical transport of electrons, then equation 2-4 becomes:

$$\frac{\partial N_e}{\partial t} = -\frac{\partial}{\partial h} \cdot (N_e \vec{w}) \ . \qquad \text{2-13}$$

In this case, it can be assumed that this derivative is entirely due to the diffusion of gas and hence:

$$\vec{w} = -\frac{D}{N_e}\frac{\partial N_e}{\partial h}, \qquad \text{2-14}$$

where D is the diffusion coefficient.

2.4. Ionospheric Layers

The variation of the electron density profile with the altitude changes during the hours of the day and with the solar activity (Fig. 2-1). It typically has the absolute maximum at about 350 km of altitude, and presents relative maxima at lower altitudes. This allows to conventionally dividing the ionosphere into two large regions called:
• topside ionosphere: beyond the absolute maximum of electronic density;
• bottomside ionosphere: below that maximum.
Due to the presence of relative maxima in the electronic density profile, the bottomside ionosphere can be divided into three other regions commonly referred to as D, E, F layer. Each layer has its own maximum plasma frequency (known as critical frequency) [18], which is the highest frequency that will be reflected from the layer. The main characteristics of each layer are described below.
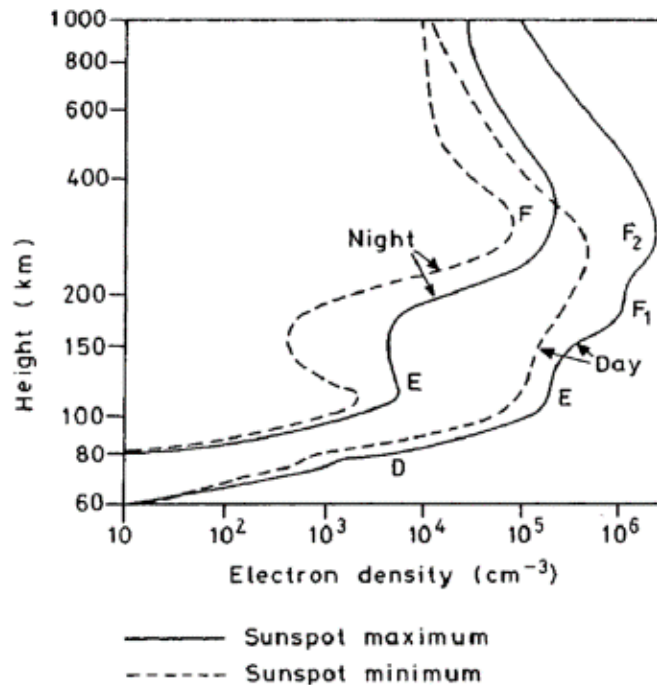
Fig. 2-1 Night and daily electron density profiles, at mid-latitude, for two different solar activity (sunspot minimum and sunspot maximum). The solid lines correspond to the profiles, daily and night, in the presence of maximum solar activity, while the dashed lines show the same profiles as the minimum solar activity [18].

2.4.1 D layer

The D layer usually ranges between 50 and 90 km and it is characterized by a much lower electron density, than the molecular one, and by a collision frequency between free electrons and molecules relatively high. This means that the dynamic and chemistry of this region is strongly dominated by the neutral component. In this region between 50 and 85 km the temperature of the neutral component decreases and then slowly rises above the 85 km.

N_e at 60 km and 80 km is, respectively, about 10^8 and 10^9 m^{-3}. At high latitudes, however, during the central hours of a winter day, electron density below 75 km is so low that it cannot be measured. One of the methods to investigate the D region is based on the analysis of the absorption of radio waves crossing it. The absorption depends on the integral of the product between N_e and the collision frequency ν across the region D. The global distribution of absorption shows, for example, that at mid-latitude it is higher in winter than in summer (winter anomaly). This is mainly due to the:

- influence of magnetic storms, the intensity of which is greater in the winter [19]:
- consequences of some atmospheric phenomena such as, the warming of stratospheric regions

The ionic composition of D layer is rather complicated. There are both positive and negative ions. The latter, in particular, are particularly important during the night hours. Positive ions are dominated by the presence of O_2^+ and NO^+, which through a series of chain reactions give rise to additional positive ions. While negative ions are dominated by the presence of O_2^- and NO_3^-.

2.4.2 E layer

In the E region, between 90 and 140 km, the temperature grows rapidly with the altitude. Above 80 km, there is a significant molecular oxygen dissociation, O_2, in atomic oxygen, O. The E region can be described as the regular E layer and the sporadic E layer, (Es). In the first, the trend of ionization follows the solar photoionization and, therefore, shows the maximum critical frequency, f_0E, around local noon. Positive ions that dominate E region are O_2^+, NO^+

Sometimes a thin layer occurs in the ionospheric E region, between 100 and 125 km, where the behaviour of the neutral atmosphere has an important role in the dynamics of the ionospheric plasma [20]. It is characterized by an anomalous high electron density that often exceeds the maximum normally located at about 350 km.

2.4.3 F layer

F layer extends conventionally from 140 km to the protonosphere (a region located above the topside ionosphere dominated by the presence of H^+ ions) and is characterized by the presence of two maxima in the electron density profiles. By consequence, this region is conventionally divided into two layers according to the two maxima, known as F1 and F2 regions. The F1 region, between 140 and 220 km of altitude, has a temperature, ranging

from 500 K, at 140 km, to over 1000 K, at 220 km. In this layer, the most important atmospheric molecule is the nitrogen N_2, which is ionized by ultraviolet solar radiation (wavelengths from 275 to 796 Å). For this reason, F1 region exists only during daytime. Above 140 km, the most important ions are NO^+ and O^+ mostly present above 170 km. The maximum of ionic production is around 180 km, which coincides with the height of maximum electronic density of F1 layer. Both the daily and seasonal trends of the critical frequency, f_0F1, are qualitatively analogous to those observed in the E region, i.e., with maximum, respectively, around midday and summer.

In the ionospheric layer F2, above 220 km, there is the maximum electron density around 350 km, although the peak of electron production is in the F1 region. This is attributable both to the fact that the factor of electronic loss decreases with the height and to the fact that between the protonosphere and the ionosphere there is a plasma flow. The dominant gas species at these altitudes is atomic oxygen, O, although N_2 and O_2 have quite important roles in the process of interchange between ion and atom, which is the basis of the electron loss due to recombination. The dominant ion specie of the F2 region is O^+. Unlike the D, E and F1 regions, F2 layer is also present during the night-time (Fig. 2-1). The F2 region also differs in the seasonal trend of f_0F2, at mid-latitudes it assumes highest values in winter and lowest in summer. The F layer is the of paramount importance for the radio-communications.

2.5. Ionospheric behaviour

The ionosphere behaviour is determined by the variation of the ionisation sources and by the physical-chemical changes of the neutral component. Since the ionosphere strongly depends on solar Extreme Ultraviolet (EUV) radiation (wavelengths between 10nm – 120 nm), four main variations can be defined and taken into account:

- daily variation, due mainly to the changing solar zenith angle;
- seasonal variation during the year;
- solar cycles variation (the solar activity vary on several time scales, the principal one being the 11-year cycle [18]) and disturbances originated in the lower atmosphere or in the near-Earth space;
- variations with the height.

Fig. 2-2 and Fig. 2-3 summarize these four changes for the mid-latitude ionosphere, respectively during solar maximum and minimum, as indicated by the T parameter values (an ionospheric index related to the level of solar activity [21]). These figures clearly demonstrate that the critical frequencies of the ionospheric layers are higher during a solar maximum than a solar minimum. Fig. 2-2 also shows an example of the mid-latitude seasonal anomaly: f_0F2 is higher in winter than in summer, despite the larger solar zenith angle.
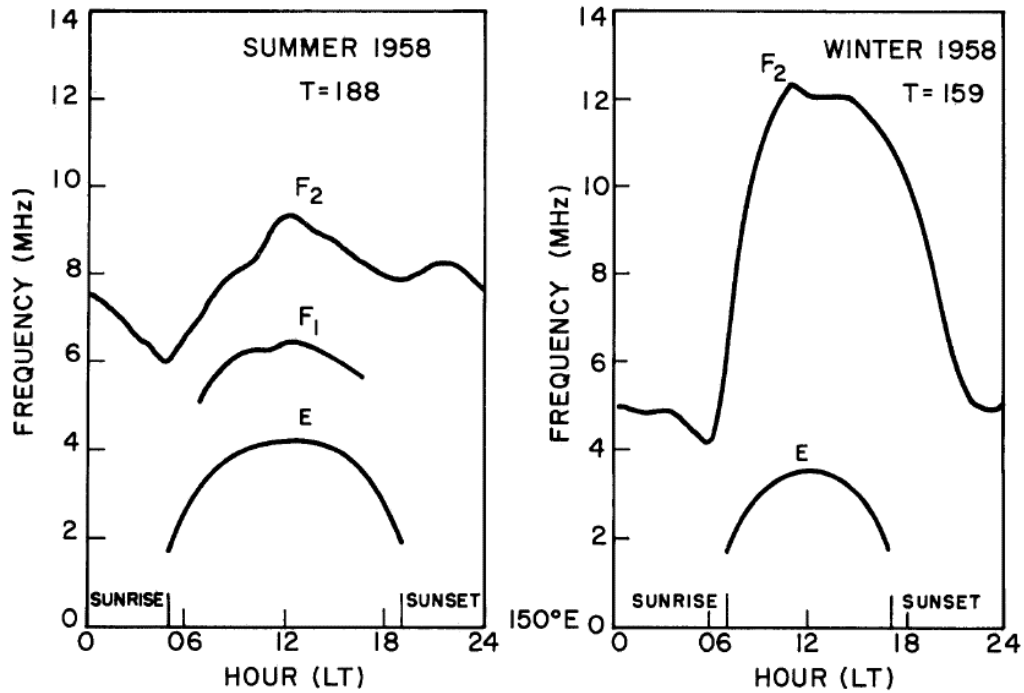
Fig. 2-2 Daily variation of the critical frequencies of three ionospheric layers (E, F1, F2) recorded at Canberra station (mid-latitude), during the solar maximum of 1958. Left panel shows measurements carried out in June and right panel shows January measurements [21].
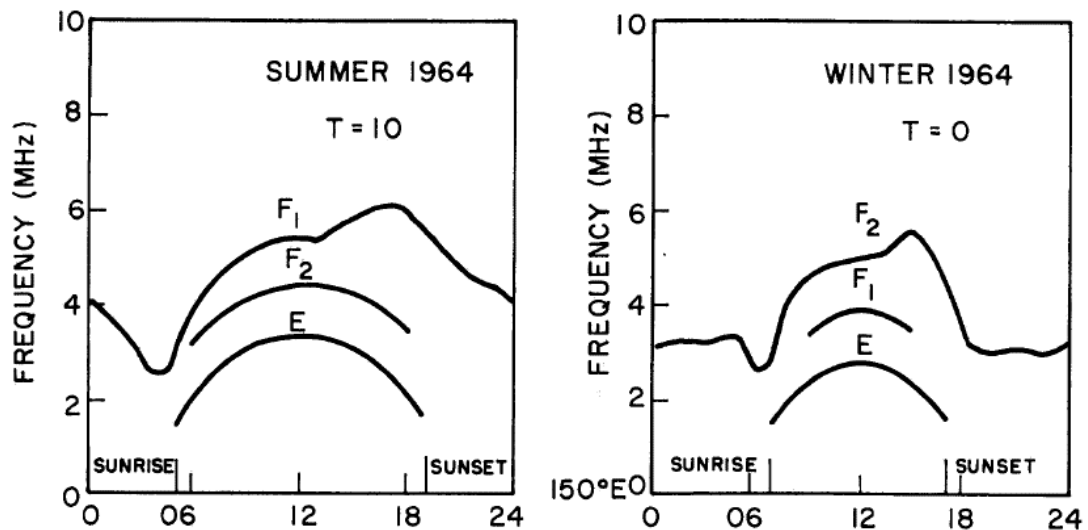
Fig. 2-3 Daily variation of the critical frequencies of three ionospheric layers (E, F1, F2) recorded at Canberra station (mid-latitude), during the solar minimum of 196. Left panel shows measurements carried out in June and right panel shows January measurements [21].

10

2.6. Mid-Latitude Ionospheric Disturbances

In the past, the research about equatorial and polar ionosphere has dominated the scientific activity in the field, because it was commonly thought that the mid-latitude ionosphere was not particularly interesting, with known morphology and well-understood processes. However, in over the last fifteen years this belief has changed, especially thanks to the new insights derived from the use GNSS receivers to study the ionosphere. Such studies reveal significant ionospheric variations of TEC occurring at mid-latitude, where TEC results to change from factors of 3 to 10 over the duration of a magnetic storm [22].

The mid-latitude ionosphere is defined as:

1. The region between the auroral ionosphere (high-latitude side) and the equatorial ionosphere (low-latitude side).
2. The region of plasma sources for the polar region and the magnetosphere.

This ionospheric region is governed by the inner magnetospheric electric field and the dynamic properties of the thermosphere.

Spatial ionospheric disturbances at mid-latitudes can be summarized into three types [22]:

- large scales (50–200 km), features associated with equatorial convective storms can propagate poleward to mid-latitudes;
- medium scale (100 km), TID, sometimes associated with magnetic storms. The prevailing direction is towards the part of the ionosphere illuminated by the Sun: from north to south in the northern hemisphere and in the opposite direction in the southern. In some cases, an east-west component is observed [23];
- small scales (<1 km), irregularities occur on background gradients with several possible origins.

2.6.1 Sporadic E layer

Sometimes at altitudes around 100 km a very dense and thin ionized layer, known as sporadic E layer (Es), can occur [24]. Es formation mechanisms cannot be explained according to Chapman theory [25]. In this region, the behaviour of the neutral atmosphere has an important role in the dynamics of the ionospheric plasma [20]. Es formation is subjected to the presence of zonal neutral wind ("wind shear" mechanism) [26]. This mechanism involves the horizontal component of the geomagnetic field and a vertical gradient in the zonal wind, which through the drag and Lorentz force constrain ions in a thin region in the E layer.

Different dynamical processes produce vertical gradient in the zonal wind:
- tidal [27], i.e. atmospheric waves of thermal origin with a period of 8 or 12 or 24 hours [28],
- planetary waves [29] with periods of about days and of planetary scale [28],
- Atmospheric Gravity Waves (AGWs) [30], that are medium-scale waves, with a period that at mid-latitudes ranging from several minutes to about one day [31].

At mid-latitude, the Es frequently occurs during summer [25], [32].

2.6.2 Traveling Ionospheric Disturbance

The traveling ionospheric disturbances (TIDs) are a wavelike perturbation in the ionospheric electron density [33]. There are three kinds of classical TID's [34]:

- quasi-periodic large-scale TID's, that have high speeds, long periods and appear as shortened wave trains of only a few cycles at most. They are associated with strong magnetic storms and a connection with auroral sub storms has been demonstrated,
- quasi-periodic medium scale TID's, that have low speeds, short period and appear as a wave train of a half-dozen cycles or more, produced by AGWs in thermosphere,
- non periodic medium scale TID's, which occur as isolated traveling irregularities in the electron density.

TIDs likely caused by AGW propagation can play an important role in causing the persistence of the Es layer as shown in [35]. Observations have also indicated the existence of a new kind of mid-latitude TIDs, that usually occur during night and tend to move in the southwest direction [36]. The development of such TIDs is commonly attributed to the Perkins instability and associated with mid-latitude spread F [37]. It is accompanied by large electric fields and can cause large total electron content TEC fluctuations.

3 SAR AND GNSS

This chapter describes two systems sensitive to the presence of the ionosphere along the signal ray path: the Global Navigation Satellite System (GNSS) and the Synthetic Aperture Radar (SAR) system.

3.1. Synthetic Aperture Radar

SARs are able to acquire data in any atmospheric conditions, independently on the sunlight and all day long. These kind of radars, typically, are on board a platform (an airplane or a satellite) and, predominantly, work in microwave frequencies range (Table 3-1).
Spaceborne SAR missions are increased in the last ten years. Table 3-2 shows the past and the future spaceborne SAR missions. For what concerns the ionospheric impact, it is worth mentioning the NISAR (NASA-ISRO Synthetic Aperture Radar, https://nisar.jpl.nasa.gov/nisarmission/), a mission carrying a double frequency SAR that will be launched in 2020.

Table 3-1: SAR bands

Band	Frequency Range (GHz)	Wavelength (cm)
P	0.3 - 1	30 - 100
L	1 - 2	15 -30
S	2 - 4	7.5 -15
C	4 - 8	3.7 - 7.5
X	8 - 12	2.4 - 3.7

The SAR observation geometry can be described as follows. The antenna points to the planet surface in a direction that is perpendicular to the motion of the platform and inclined with respect to the nadir [38]. The direction along the platform motion is called "azimuth direction" (or "along-track"), while the direction along the line of sight (LOS) is the slant direction and its projection on the ground is the ground range direction (or "across-track") [38].
Fig. 3-1 exemplifies the typical SAR geometry showing the azimuth and the range directions, the slant path, the look angle and the swath (the strip acquired by SAR).
During the motion of the platform, the SAR's antenna transmits pulses and receives the backscattered echoes from the ground. The portion of the Earth's surface hits by the pulses transmitted by SAR's antenna is called "target". As the antenna receives the backscattered
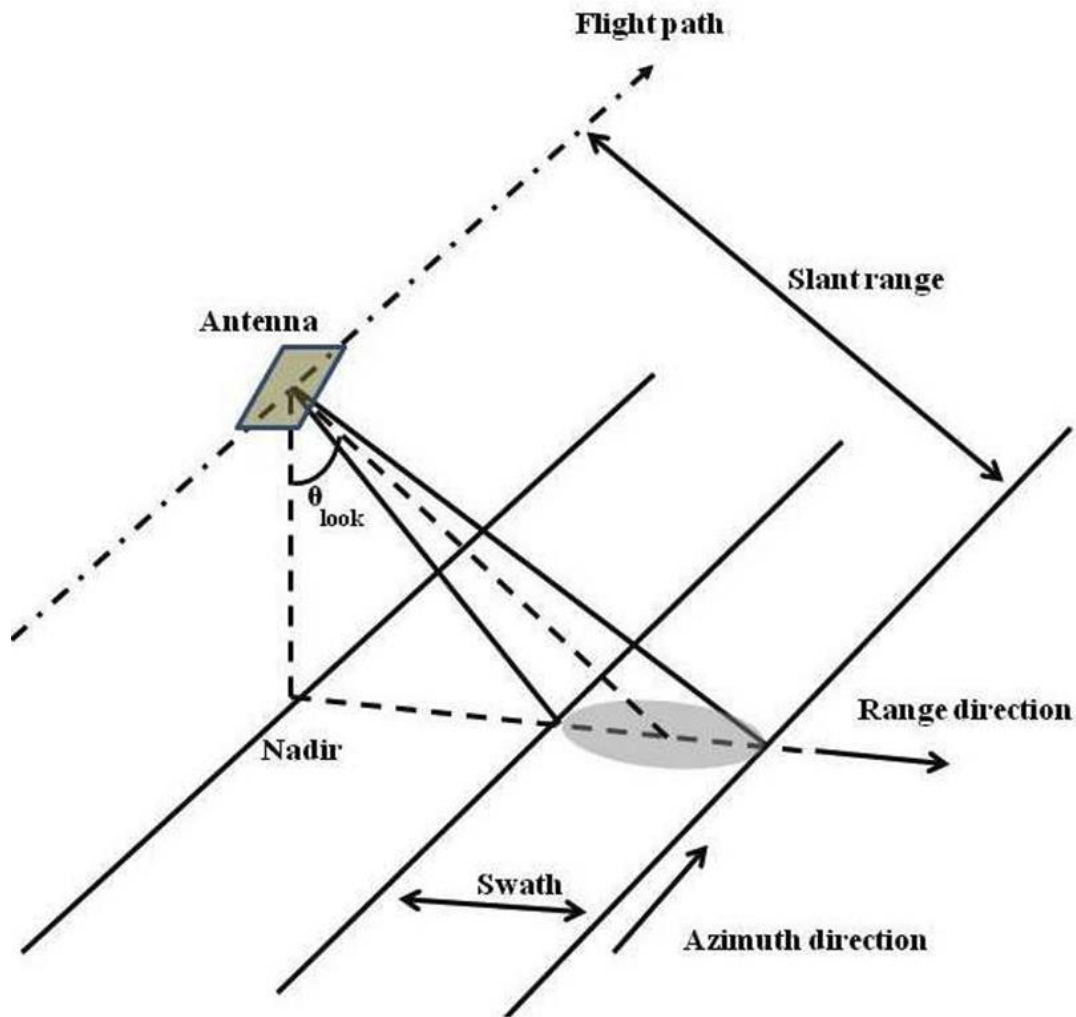
Fig. 3-1 SAR imaging geometry
(https://media.asf.alaska.edu/uploads/about%20sar%20and9%20insar/nasa_illustration_b
asic_sar_look_angle_more.jpg)

echoes in a different position than the transmission, it is possible to assume that these echoes derive from different portions of the same antenna. This fact allows the radar having a "synthetic aperture" that is much longer than the physical antenna length. The advantage of the synthetic aperture mainly comes from the capability of a larger azimuth resolution than in a static configuration. To reach a range resolution of meters, short pulses (nanoseconds) must be transmitted. However, since the duration of a pulse is also related to its energy, pulses longer than nanoseconds are needed to detect the target [39]. To solve this problem, modulated frequency pulses ("chirps") are then transmitted [40]:

$$f(t) = rect\left[\frac{t}{\tau}\right] \cdot cos\left(\omega t + \frac{\alpha}{2}t^2\right)$$
<div align="right">3-1</div>

where τ is the duration of the transmitted pulse, $\omega=2\pi f_c$ is the angular frequency (f_c is the central frequency of the transmitted bandwidth) and α is the chirp rate.

Then, by associating to each pixel the relative contribution of the backscattered signal ("focusing"), it is possible to form an image, i.e. a complex matrix defined by the amplitude and the phase of the backscattered signal. The amplitude determines the part of the incident wave that is backward diffused to the sensor, while the phase depends on several factors such as the sensor-target geometric distance, the presence of the atmosphere and the noise produced by the acquisition system.

As SAR satellites are in near-polar orbits, they acquire image in two different orbits: ascending when the satellite travels northwards and descending, when the satellite travels southwards (Fig. 3-2).
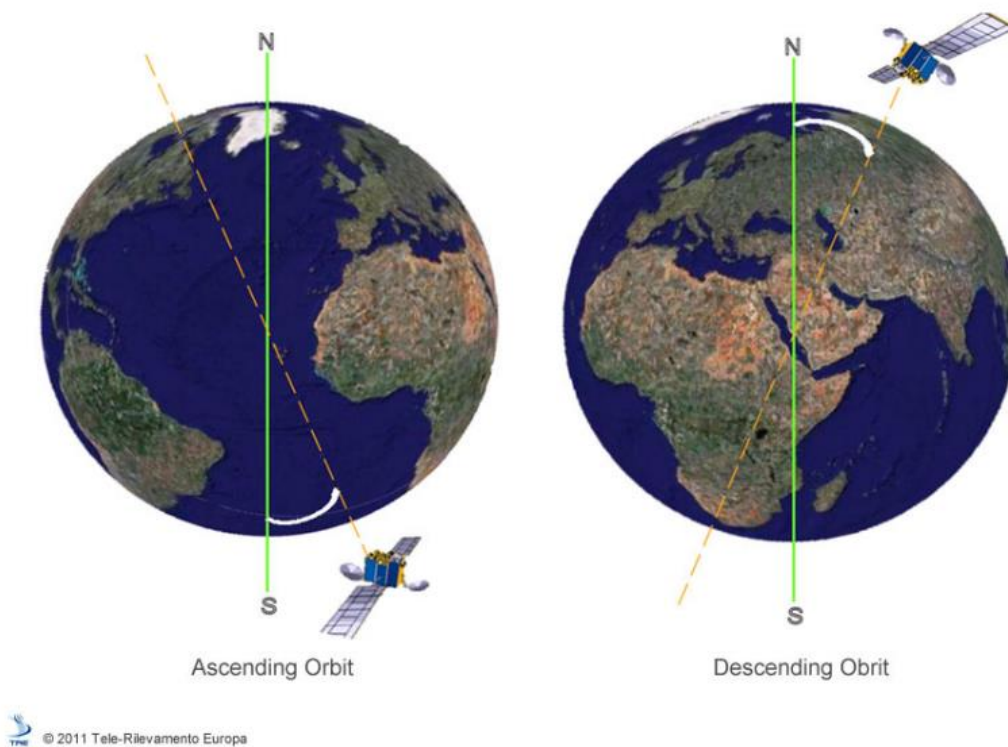
Fig. 3-2 Ascending and descending orbits

Table 3-2: Spaceborne SAR systems

Name	Band	Start mission	End mission
SEASAT	L	June 27, 1978	October 10, 1978
ERS-1	C	July 17, 1991	March 10, 2000
JERS-1	L	February. 11, 1992	October 12, 1998.
ERS-2	C	April 20, 1995	September 5, 2011.
RADARSAT-1	C	November 4, 1995	29 March 2013
ENVISAT-ASAR	C	March 1, 2002	May 9, 2012laun
ALOS-PALSAR	L	January. 24, 2006	May 12, 2011
SAR-Lupe	X	December 19, 2006	Operating
COSMO-SkyMed	X	June 8, 2007	Operating
TerraSAR-X and	X	June 15, 2007	Operating
RADARSAT-2	C	December 14, 2007	Operating
RISAT-2	X	April 20, 2009	Operating
TanDEM-X	X	June 21, 2010	Operating
HJ-1C	S	November 18, 2012	Operating
RISAT-1	C	April 26, 2012	Operating
KOMPSAT-5	X	22 August 2013	Operating
Sentinel-1	C	April 3, 2014	Operating
ALOS2-PALSAR2	L	May 24, 2014	Operating
PAZ	X	End 2017	
SAOCOM 1/2	L	2018	
RADARSAT Constellation	C	2018	
NISAR	L/S	2020	
BIOMASS	P	2021	

3.1.1 Acquisition Mode

A modern SAR works in three different acquisition modes:

- StripMap, in which the antenna is pointed at the same angle while the swath is illuminated. Therefore, the image is a strip limited in range but not in azimuth direction;
- Spotlight, in which the radar beam is steered in azimuth direction to illuminate the same scene for a longer time. This entails an increase in the synthetic aperture size and an increase in the azimuth resolution, but, also, a decrease in the size of the illuminated scene;
- ScanSAR, in which the radar beam is steered in range direction to increase the swath dimension in range by illuminating different sub swath. This means that each target is illuminated from a smaller synthetic aperture and so the azimuth resolution is worst.

In this work, the SAR data are acquired in StripMap mode, as it is a good compromise between resolution and amplitude of the illuminated area.

3.1.2 Interferometric SAR technique

SAR Interferometry (InSAR) is a technique based on the analysis of the phase differences between two (or more) SAR images acquired on the same area. These images can be acquired on the same area from slightly different look angles, or simultaneously, with two antenna mounted on the same platform (the so-called "bistatic radar"), or even at different times (the so-called "repeat-pass interferometry mode").
The cross-multiplying, pixel by pixel, of the first SAR image (commonly called "master") with the complex conjugate of the second (commonly called "slave") forms the interferometric image (interferogram) [38]:

$$Ae^{i\Delta\varphi} = A_M e^{i\varphi_M} \cdot A_S e^{-i\varphi_S} = A_M A_S e^{i(\varphi_M - \varphi_S)} \qquad \text{3-2}$$

In this formula, the interferometric amplitude (A) is the amplitude of the master image (A_M) multiplied by the amplitude of the slave (A_S) and the interferometric phase $\Delta\varphi$ is the difference between the phase of the master image φ_M and the phase of the slave one φ_S.
In the repeat pass mode (Fig. 3-3), considering that the two images are acquired in different orbits, they must be precisely aligned (with at least an accuracy of 0.1 pixel) to match the pixels in the first image with the pixels in the second one [1]. To do this, the master is used as reference and the slave is corrected accordingly. This process, known as "co-registration", enables the formation of the interferogram. The resulting interferometric phase is the sum of different contribution:

$$\Delta\varphi = \frac{4\pi}{\lambda}\Delta R + \Delta\varphi_f + \frac{4\pi}{\lambda}B + \Delta\varphi_{atm} + \Delta\varphi_{diel} + \Delta\varphi_r + 2n\pi. \qquad \text{3-3}$$

where λ is the wavelength.
   The first term ($4\pi\Delta R/\lambda$) is the surface displacement between the two acquisitions, along the LOS direction. The others are the contributions that affect the correct estimation of the surface displacement. The second term ($\Delta\varphi_f$) is due to topography and can be removed by using a Digital Elevation Model (DEM) [1]. The third term ($4\pi B/\lambda$) is due to the shift in the orbital trajectory between the two image acquisitions (Fig. 3-3). This is known as "geometric baseline" (indicated with B) and can be estimated and removed by using precise orbits [1]. The fourth term, $\Delta\varphi_{atm}$, is the phase produced by the passage of the signal through the atmosphere (troposphere and ionosphere). $\Delta\varphi_{diel}$ is due to variations in dielectric property of the ground pixel, between two acquisitions and $\Delta\varphi_r$ is the phase noise difference. This term can be removed by averaging the adjacent pixels (the so-called "multi-look" technique [38]) [1].
The last term $2\pi n$ is associated to the phase wrapping ambiguity (the phase has module 2π) [1]. This term can be removed by unwrapping the phase, i.e. by adding or subtracting an integer multiple of 2π to each pixel starting from a reference point.
Therefore, taking into account that $\Delta\varphi_{diel}$ is null if the dielectric properties of the ground

pixels are assumed reasonably constant between master and slave passages, the interferometric phase (equation 3-3) becomes:

$$\Delta\varphi = \frac{4\pi}{\lambda}\Delta R + \Delta\varphi_{atm} \qquad\qquad 3\text{-}4$$

By consequence, the atmosphere introduces an error in the displacement measurement and its mitigation is a crucial step to improve the measurement accuracy.
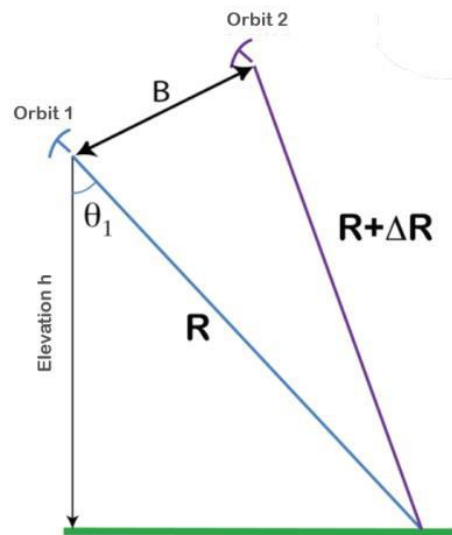
Fig. 3-3 Repeat-pass interferometry mode R is the satellite-target distance for the first orbit, R+ΔR is the satellite-target distance for the second orbit, θ₁ is the look angle for the first satellite and B is the baseline
(http://seom.esa.int/landtraining2015/files/Day_4/D4P1a_LTC2015.pdf)

3.1.3 Multiple-Aperture Interferometry (MAI)

InSAR technique is able to retrieve information only along the satellite's LOS direction. To extract information in the along-track direction, the LOS must be changed slightly forward and backward with respect to the nominal radar squint direction. This allows constructing forward- ($\Delta\varphi_f$) and backward-looking ($\Delta\varphi_b$) interferograms:

$$\Delta\varphi_f = -\frac{4\pi x}{\lambda}\sin(\theta_S + \beta)$$
$$\Delta\varphi_b = -\frac{4\pi x}{\lambda}\sin(\theta_S - \beta)\ ; \qquad\qquad 3\text{-}5$$

where x is the displacement in the along-track direction, θ_S is the squint angle and β is its angular variation. The β angle is a function of the antenna length, l, of the normalized squint, n (for half aperture, $n = 0.5$) and of the wavelength $\beta = \lambda n/2l$.

For small θ_S and β, the phase difference between these two interferograms gives information about along track (or azimuth) displacement (Fig. 3-4) [41], [42]:

$$\Delta\varphi_{MAI} = \Delta\varphi_f - \Delta\varphi_b = -\frac{4\pi x}{\lambda} 2sin(\beta)cos(\theta_S) \approx \frac{4\pi n}{l}x \qquad\qquad 3\text{-}6$$

This technique in known as Multiple-Aperture Interferometry (MAI).
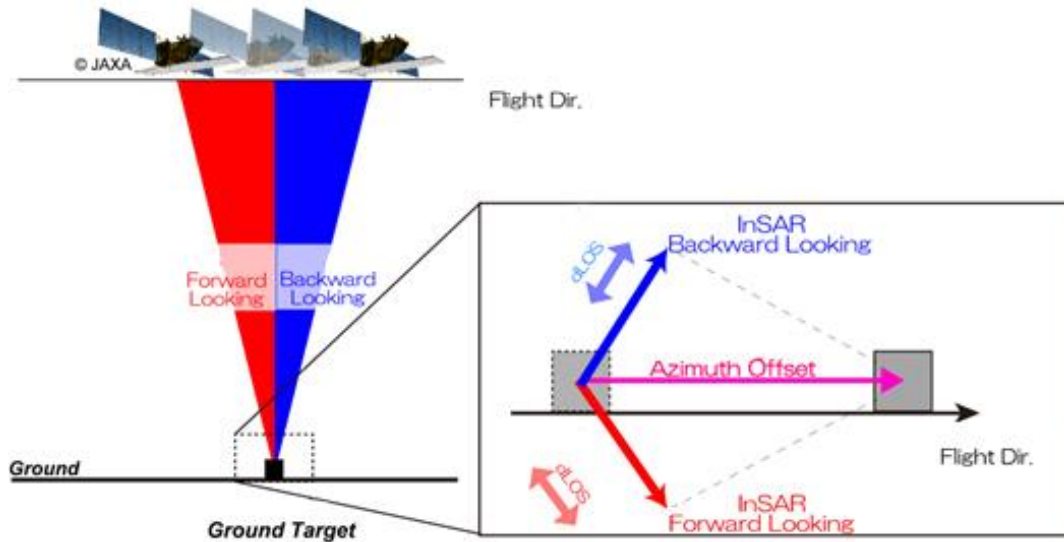
Fig. 3-4 Illustration of MAI technique. (extracted from http://www.gsi.go.jp/cais/MAI-e.html)

3.2. Global Navigation Satellite System (GNSS)

The US DoD (Departmente of Defense) developed, in the 1970s, the first global navigation satellite system. Its name was GPS (Global Positioning System) and was composed by 24 satellites orbiting, around the Earth, at an altitude of approximately 20.200 km. Each satellite passes over the same area of the Earth twice a day. After the GPS (currently having 32 satellites), three other systems have been developed:

- GLObal NAvigation Satellite System (GLONASS) by Russia, which has 25 satellites at a height of about 19,140 km;
- GALILEO by European community, which has 24 operational satellites plus six spares, at an altitude of about 23.222 km. It is foreseen to be completed and fully operational by 2020;
- BeiDou Navigation Satellite System (BDS or Beidou-2), which is expected to start the operations on 2020.

All these systems are commonly named Global Navigation Satellite System (GNSS). In this context, "global" means that the system covers the whole globe. Besides this, regional navigation satellites systems exist (RNSS), like the Japanese Quasi-Zenith Satellite System (QZSS) and the Indian Regional Navigation Satellite System (IRNSS).

In general, a GNSS system is composed by three segments:

- the *space segment*, which consists of the satellites constellation. Orbital features are such that at any time of the day and from any point on the Earth's surface it is

possible to receive signals at the same time by at least four satellites. The number of satellites allows redundant measurements;

- the *control segment*, which consists of a network of ground stations, whose position is known with great precision, and which have the task to monitor the whole system and ensure its own operation. In the specific, navigational update to each satellite, including the synchronization of the atomic clocks carried on-board and the adjustment of the ephemeris of each satellite's internal orbital model, is provided on a regular basis, together with other information, like inputs about space weather conditions and so on;
- the *user segment*, consisting of all civilian and military users able to receive the GNSS signals and, therefore, to determine their coordinates in a suitable reference system.

Each GNSS satellite transmits the carrier wave, the ranging code (i.e. a binary sequence to univocally identifying the satellite) and the navigation message, in which the time information (time-of-week and week number) is carried. The GNSS receiver generates its own code and compare it with the transmitted one, in order to measure the difference between the transmission time and the reception time of the signal (Fig. 3-5)
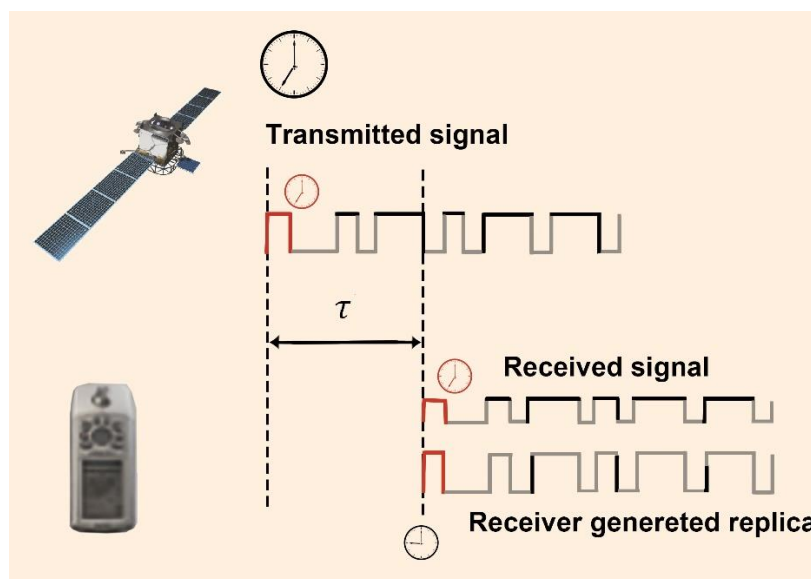
Fig. 3-5 Example of transmitted ranging code and sequence generated by the receiver [43]

Leveraging on timing information, the receiver-satellite distance R_i^s (range) is calculated by measuring the travelling time τ_i^s of the signal emitted by the satellite (s) to the receiver (i). Indicating with c the speed of light and with t the time of the clock in the receiver, R_{0i}^s is given by:

$$R_{0i}^s(t) = c \cdot \tau_i^s \qquad\qquad 3\text{-}7$$

If $r_{r=}(x_r;\ y_r;\ z_r)$ is the position of the receiver (unknown) and $r^s = (x^s;\ y^s;\ z^s)$ is the position of the satellite, assuming that the clocks in the receiver and in the satellite are synchronized and there are no measurement errors, $R_{0i}{}^s$ is given by:

$$R_{0i}^{s}(t) = \|r_r(t) - r^s(t - \tau_i^s)\| =$$

$$[(x_r(t) - x^s(t - \tau_i^s))^2 + (y_r(t) - y^s(t - \tau_i^s))^2 + (z_r(t) - z^s(t - \tau_i^s))^2]^{\frac{1}{2}}.\quad \text{3-8}$$

Therefore, the receiver can be in any point of a sphere, centered on the satellite and with a radius equal to the measured range. If a second satellite is simultaneously available, then the receiver can be also in any point of a second sphere. Intersecting these two spheres, it results that the receiver can be in any point of a circle. Taking in to account a third satellite and intersecting the three spheres available, the receiver can be in only two point of the space. As the Earth itself is more or less a sphere, only one of the two points lies on the Earth's surface. Therefore, knowing the position their distance from the receiver of at least three satellite, it is possible to find the position of the receiver solving a geometric problem known as trilateration technique (
Fig. 3-6). However, the clocks in the receiver and in the satellite are not synchronized. This produce a clock error dt_i and therefore an error in the range measurement:

$$R_i^s(t) = R_{0i}^s(t) + c \cdot dt_i + \varepsilon_{err};\quad\quad\quad \text{3-9}$$

in which ε_{err} includes all the other errors. To overcome the synchronization problem, a fourth satellite is needed to found the position of the receiver.

Fig. 3-6 Trilateration technique (http://gisgeography.com/wp-content/uploads/2016/10/GPS-Trilateration.png)
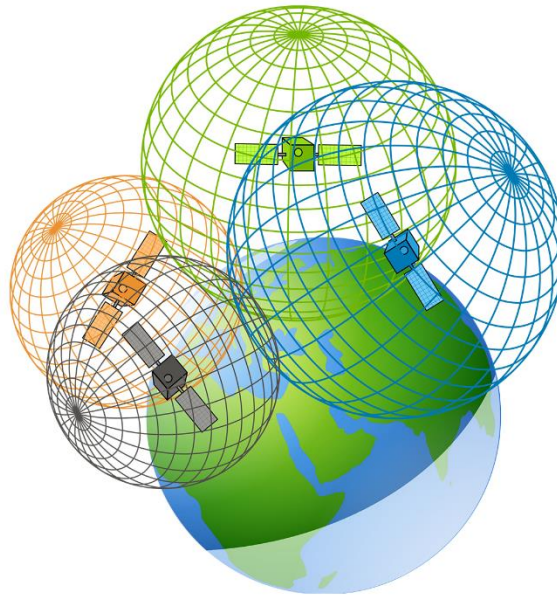
Thus the geometric distance remains to be affected by the various types of error (ε_{err}) that can be enclosed in five major categories according to the cause that produces them: clocks, orbits, the atmospheric delay and multipath. The first two errors are minimized by the GNSS ground control system that continually monitors the satellite orbit and clock. The multipath, i.e. the reflection of the signal from any object (terrain, buildings, etc.) can be minimized by using suitable antenna (choke-ring). The atmosphere changes the speed with which the signal propagates, causing a delay called atmospheric delay. Two atmospheric layers affect the GNSS signals propagation: the troposphere and the ionosphere. The troposphere layer extends from the Earth's surface to an altitude of about 15 km. In the troposphere, the propagation delay is independent on the transmitted signal frequency, as it is a non-dispersive medium, but it depends on temperature, pressure and humidity [44]. The ionospheric delay is explained in detail in Chapter 4.

4 IONOSPHERIC EFFECTS ON LOW FREQUENCY SAR

Small, medium and large-scale ionospheric plasma structures embedded in the ambient ionosphere cause several effects on electromagnetic waves crossing them. Among the others, the ionospheric delay and the phase shift, both caused by medium and large-scale electron density structures that are more likely to occur at mid-latitudes, are here described as of interest in treating SAR data.

4.1. Ionospheric delay

The velocity of an electromagnetic signal travelling in a free space is equal to the speed of light, c. However, when an electromagnetic wave crosses a medium, its velocity v changes by a factor n ($v = c/n$.), called refractive index and depending on the optical properties of the medium. The ionospheric refractive index can be calculated by using the Appleton-Hartree equation [18]:

$$n^2 = 1 - \frac{X}{1-jZ-\left[\frac{Y_T^2 \, sin^2 \vartheta}{2(1-X-jZ)}\right] \pm \left[\frac{Y_T^4 \, sin^4 \vartheta}{4(1-X-jZ)^2}+Y_L^2 \, cos^2 \vartheta\right]^{1/2}} ,$$
4-1

in which $X=\omega_P^2/\omega^2$, $Y_T= \omega_T/\omega$, $Y_L= \omega_L/\omega$ and $Z = v/\omega$ are dimensionless quantities. The angular plasma frequency, ω_P, is equal to $(N_e \cdot e^2/\varepsilon_0 m)^{1/2}$, where e and m are the charge and mass of an electron, respectively, N_e is the electron density and ε_0 is the electric permittivity of free space. The terms ω_L and ω_T are respectively the longitudinal and transverse components of electron gyrofrequency (the natural frequency at which free electrons circle around the magnetic field lines), ϑ is the angle between the propagation direction and the geomagnetic field, v is the electron collision frequency and ω is the angular wave frequency.

In the case of L-band signal, the effect of collision and magnetic field on the refractive index can be neglected as $\omega>>\omega_T$, $\omega>>\omega_L$ and $\omega>>v$. Then, by expanding in Taylor series the square root of equation 4-1, the refractive index becomes:

$$n = 1 - \frac{1}{2}X = 1 - \frac{1}{2}\frac{\omega_p^2}{\omega^2} = 1 - \frac{\zeta \, Ne}{f^2},$$
4-2

where f is the frequency of the electromagnetic wave and ζ is a constant ($\zeta =e^2/8\pi^2\varepsilon_0 m=40.3$ [m^2/s^3]). Therefore the satellite-receiver ray path, R', is given by the following generalized form [45]:

$$R' = \int_{satellite}^{reciever} n \, ds = \int_{satellite}^{reciever} \left(1 - \frac{\zeta Ne}{fc^2}\right) ds = R - \frac{\zeta}{fc^2}\int_{satellite}^{reciever} Ne \, ds$$
4-3

where R is the satellite - receiver geometric distance.

The difference between measured and geometric distance is the delay experienced by signals traveling through the ionosphere. This is known as ionospheric delay.

The integral of the electron density along the ray path, known as TEC, is the total number of free electrons in a cylinder with a cross section of $1m^2$ and a height equal to the slant signal path:

$$TEC = \int_{satellite}^{reciever} Ne\ ds \qquad 4\text{-}4$$

This quantity is measured in Total Electron Content Unit (TECu), with 1 TECu equivalent to 10^{16} electrons/m^2.

4.2. Phase and azimuth shifts

Phase shift
The most significant consequence of the ionospheric delay experienced by a SAR signal is a shift in the phase of a SAR image, φ_{iono}, known as "phase advance". Indeed, if f_c is the central frequency of the SAR signal then, taking into account only the ionospheric delay and neglecting any other effects, the interferometric phase of a SAR image is given by:

$$\varphi = \frac{2\pi f_c}{c}\ 2R' = \frac{4\pi f_c}{c}\left(R - \frac{\zeta}{f_c^2}TEC\right) = \frac{4\pi f_c}{c}R + \varphi_{iono} \qquad 4\text{-}5$$

where

$$\varphi_{iono} = -\frac{4\pi}{c}\cdot\frac{\zeta}{f_c}TEC \qquad 4\text{-}6$$

In the InSAR technique (in repeat pass mode), at least two images are acquired at different times, therefore the ionosphere induces a phase advance ($\Delta\varphi_{iono}$) corresponding to [10]:

$$\Delta\varphi_{iono} = -\frac{4\pi}{c}\cdot\frac{\zeta}{f_c}\Delta TEC \qquad 4\text{-}7$$

where ΔTEC is the variation of the Total Electron Content between the two time acquisitions.

Azimuth shift
As the satellite moves during the signal acquisition with a velocity v, the antenna receives backscattered signal from the same target at different positions in the azimuth direction. Considering a target in azimuth position $x_p = 0$, the satellite-target distance R becomes function of the antenna azimuth position, x, as follows [9]:

$$R(x) = \sqrt{R_0^2 + x^2} \approx R_0 + \frac{1}{2}\frac{x^2}{R_0} \qquad 4\text{-}8$$

24

where R_0 is the distance at the closest approach (i.e. the minimum distance between the satellite and the target). Thus, the phase φ_0 of the received signal changes during the flight path according to:

$$\varphi_0(x) = \frac{4\pi f_c}{c} R(x) \approx \frac{4\pi f_c}{c} R_0 + \frac{2\pi f_c}{c} \frac{x^2}{R_0} \ . \qquad \text{4-9}$$

If the azimuth position of the target varies of Δx, then the phase of the received signal, $\hat{\varphi}(x)$, is as follows:

$$\hat{\varphi}(x) = \frac{4\pi f_c}{c} R_0 + \frac{2\pi f_c}{c} \frac{(x-\Delta x)^2}{R_0} = \varphi_0(x) + \frac{4\pi f_c}{c} \frac{\Delta x^2}{R_0} - \frac{4\pi f_c}{c} \frac{\Delta x}{R_0} x. \qquad \text{4-10}$$

Therefore, a displacement in the azimuth position of the target gives a phase equal to the phase of the target located at $x_p = 0$ plus two additional terms: one constant and one dependents from the antenna azimuth position.

As the phase $\varphi_0(x)$ is related to the Doppler frequency f_d by the following formula [7]:

$$\varphi_0(x) = 2\pi \int f_d(t)dt \qquad \text{4-11}$$

a variation Δx of the target azimuth position produces a shift in the Doppler frequency according to:

$$f_{dtot}(t) = \frac{1}{2\pi} \frac{\partial \hat{\varphi}(x)}{\partial t} = \frac{1}{2\pi} f_d(t) - \frac{2f_c}{cR_0} v\Delta x \qquad \text{4-12}$$

where $f_{dtot}(t)$ is the resulting Doppler frequency after the changing Δx.

Since the ionosphere produces a phase shift on the SAR image, ionospheric variations along the azimuth direction produce a shift in the Doppler frequency given by:

$$f_{dtot}(t) = \frac{\partial \varphi(x)}{\partial t} = f_d(t) + \frac{\partial \varphi_{iono}(x)}{\partial t} = f_d(t) + \frac{\partial \varphi_{iono}(x)}{\partial x} \cdot \frac{\partial x}{\partial t} =$$

$$f_d(t) + v \cdot \frac{\partial \varphi_{iono}(x)}{\partial x} \qquad . \qquad \text{4-13}$$

Therefore, by combining equation 4-12 and 4-13:

$$v \cdot \frac{\partial \varphi_{iono}(x)}{\partial x} = -\frac{2f_c}{cR_0} v\Delta x \qquad \text{4-14}$$

and by considering the relation 4-6 between φ_{iono} and TEC, it is possible to affirm that TEC variations along the azimuth direction cause an offset Δx in the azimuth position of the pixel in respect to the actual one [6] [46]:

$$\Delta x = \frac{2\,\zeta}{f^2}\frac{\partial TEC}{\partial x}$$

<div align="right">4-15</div>

For a single SAR acquisition, azimuth shifts are of secondary importance compared to other errors, but they become relevant when InSAR technique is applied [8]. If the azimuth shifts are different between the master and the slave acquisitions, a coregistration offset is produced and the so called "streaks" can be observed [6] [47].

5 DATA AND METHODS

The ionospheric temporal fluctuations could lead to a misinterpretation of the geophysical parameter retrieved by InSAR image.

In this chapter, the data analysis strategy applied to retrieve the TEC temporal variation (ΔTEC_{SAR}) from the interferometric phase is introduced. Details are also given on the ΔTEC evaluation from the GPS data provided by RING (Rete Integrata Nazionale GPS, http://ring.gm.ingv.it//) network by using the hypothesis of a "frozen" ionosphere within a time interval of 5 minutes around the corresponding ALOS passages.

5.1. TEC temporal variation from InSAR image

If no meaningful movements of the ground occur in the period between the two passages (such as those due to an earthquake for instance), the interferometric phase is due only to the atmospheric (ionospheric $\Delta\varphi_{iono}$ plus tropospheric $\Delta\varphi_{tropo}$) contribution and equation 3-4 becomes:

$$\Delta\varphi = \Delta\varphi_{atm} = \Delta\varphi_{tropo} + \Delta\varphi_{iono} \; ; \qquad \text{5-1}$$

To retrieve ΔTEC from the interferometric phase $\Delta\varphi$, $\Delta\varphi_{tropo}$ must be assumed as constant in formula 5-1. To identify when such condition is verified, a method based on the correlation between the integral of the azimuth shifts (Δx), and the interferometric phase is applied. The main steps of this approach are detailed below.

As introduced by [6] and further investigated by [10], the azimuth gradient of the tropospheric phase ($\frac{\partial \Delta\varphi_{tropo}}{\partial x}$) results into a negligible shift in the Doppler frequency (see eq. 4-15). By consequence, the integral of equation 4-15 is proportional only to ΔTEC:

$$\int \Delta x \, dx \propto \Delta TEC \qquad \text{5-2}$$

The integral in left side of equation 5-2 can be calculated by using a numerical integration. Starting from an $M_{\Delta x} \times N_{\Delta x}$ array of shifts, where $M_{\Delta x}$ and $N_{\Delta x}$ are the number of pixels in azimuth and range respectively, the integral is given by:

$$\begin{cases} \Delta x(1, j_{\Delta x}) \approx \Delta\varphi_{iono}(1, j_{\Delta x}) \propto \Delta TEC(1, j_{\Delta x}) & if \; i_{\Delta x} = 1 \\ \Delta x(i_{\Delta x}, j_{\Delta x}) + \sum_{n_{\Delta x}=2}^{i_{\Delta x}} [\Delta x(n_{\Delta x} - 1, j_{\Delta x})] \approx \Delta\varphi_{iono}(i_{\Delta x}, j_{\Delta x}) \propto \Delta TEC(i_{\Delta x}, j_{\Delta x}) & if \; i_{\Delta x} > 1 \end{cases}$$

$$\forall \; i_{\Delta x} = 1 \dots M_{\Delta x} \; and \; j_{\Delta x} = 1 \dots N_{\Delta x} \qquad \text{5-3}$$

where $\Delta\varphi_{iono}(i,j)$ is the ionospheric contribution to the interferometric phase at the pixel *(i,j)* and $\Delta TEC(i,j)$ is the TEC differences between master and slave passages at the pixel *(i,j)*. If correlation between the integral of azimuth shifts, equation 5-3, and the interferometric phase $\Delta\varphi$, equation 5-1 stands, then $\Delta\varphi_{tropo}$ can be assumed as constant (C_{tropo}). This follows from from equation 5-2, in which the integral of the azimuth shifts is only proportional to ΔTEC. After the verification of the applicability of the constants troposphere approximation, the TEC temporal variation (between master and slave acquisition times) can be derived, for each master-slave couple of images, from the interferometric phase as:

$$\Delta TEC_{SAR} = \frac{c \cdot f_c}{4\pi\zeta}\Delta\varphi + C_{tropo} \qquad\qquad 5\text{-}4$$

As in this investigation focus is given only to the correlation factor, the proposed analysis is independent on the integration constant and the scaling factor arising from the system of equations 5-3.

For this thesis, SAR images acquired in single receiver mode over six different epochs have been considered to produce five interferograms (Table 5-1). The images are acquired by ALOS-PALSAR, whose characteristic are summarized in (Table 5-2), operating in Fine Beam Dual (FBD) mode (bandwidth equal to 14 MHz), except for that one of April 8th 2010, that is acquired in Fine Beam Single (FBS) mode (bandwidth equal to 28 MHz). To overcome the differences arising when using such different bandwidths, the images acquired in FBD mode are oversampled by a factor 2. The selected images belong to the frame 820 of the ground track 638 taken over central Italy. The azimuth shifts Δx are estimated by using the MAI technique set with the parameters reported in Table 5-3 and applying the Goldstein filter [48]. The interferograms are unwrapped using the minimum cost flow (mcf) method [49] .

Table 5-1: Date of the master/slave images and relative parameters used in this thesis θm and θs are the incidence angle of the master and the slave image *Bt* stands for the temporal baseline and *B* stands for perpendicular baseline.

Case #	Acquisition time master	Acquisition time slave	θm (°)	θs (°)	Bt (days)	Bp (m)
1	July 1st, 2007	August 16th, 2007	38.72	38.74	46	279.586
2	July 1st, 2007	October 1st, 2007	38.72	38.72	92	536.456
3	August 16th, 2007	October 1st, 2007	38.74	38.72	46	256.816
4	April 8th, 2010	May 24th, 2010	38.75	38.73	46	-2.9173
5	May 24th, 2010	July 9th, 2010	38.73	38.73	46	56.9519

Table 5-2: PALSAR characteristics [50]

Item	Specifications
Centre frequency	1270 MHz / 23.6 cm
Chirp band width	28 MHz (single polarisation) 14 MHz (dual polarization)
Transmission power	2 kW (peak power)
Pulse Repetition Frequency	1500 – 2500 Hz (discrete stepping)
Image modes	Single polarization. (HH or VV) Dual polarization. (HH+HV or VV+VH)
Bit quantisation	3 or 5 bits (5 bits standard)
Off-nadir angle	Variable: 9.9 – 50.8 deg. (inc. angle range: 7.9 - 60.0)
Look direction	Right
Data rates	240 Mbps
Radiometric accuracy	< 1 dB relative (within scene) < 1.5 dB absolute (between orbits)

Table 5-3 Parameters used for MAI technique.

	Parameter	Value
	normalized squint parameter	0.5
	azimuth multilook	20
	range multilook	8
Goldstein filtering	exponent for non-linear fitting	0.8
	filtering FFT window size	64
	coherence parameter estimation window size	7
	range step	4
	azimuth step	4
	minimum fraction of points required to be non-zero in the filter	0.9

5.2. TEC temporal variation from GNSS

The GNSS satellite signals received by suitable network of ground-based receivers are an excellent means to study and characterize the ionospheric environment and its variability in space and time. Due to the dispersive nature of the ionosphere, starting from code or carrier phase measurements provided by GNSS receivers on different frequencies, it is possible to calculate TEC along each slant path, according to the following formula:

$$TEC = \frac{1}{40.3}\left(\frac{L1^2 L2^2}{L_2{}^2 - L_1{}^2}\right)(P_2 - P_1) - \varepsilon. \qquad\qquad 5\text{-}5$$

Equation 5-5 represents the so-called "geometry-free combination" in which L_1 and L_2 are two carrier frequencies of the transmitted signal, P_1 and P_2 are the corresponding pseudoranges (satellite-receiver optical path) and ε represents all the frequency-dependent biases induced by the receiver, satellite, multipath etc. In the case of GPS signals, considered in this thesis, L_1 =1575.42 MHz and L_2 =1227.60 MHz. Each TEC value is measured along the satellite-receiver path and, therefore, is called "slant TEC" (sTEC). Thus, for each satellite, TEC measurements take place at different elevation angles and so are related to different ionospheric sectors. To obtain TEC values independent on the geometry of the GNSS constellation and of the receiver's network, sTEC must be converted into the vertical TEC (vTEC). This can be done by assuming that the ionosphere is a thin, ionized layer located at the height H above at the Earth's surface where the electron density maximizes (Single Thin Layer approximation, Fig. 5-1) [56]:

$$vTEC = sTEC\ cos(z'), \qquad\qquad 5\text{-}6$$

where

$$sin(z') = \frac{R_E}{R_E + H}\ sin(z). \qquad\qquad 5\text{-}7$$

In the above formula, z and z' are the zenith angles at the receiver and at the ionospheric pierce point IPP (intersection between the LOS and the thin layer ionospheric), respectively, while R_E is the Earth's radius.
The minimization of the biases ε in equation 5-5 is a very delicate issue of the TEC determination from GNSS: it is necessary to apply a calibration procedure [51] to obtain reliable TEC values. In this thesis, the GOPI software (http://seemala.blogspot.it/2011/04/rinex-gps-tec-program-version-22.html) has been adopted for the TEC calibration. GOPI software provides, for each satellite-receiver link, TEC values projected to the vertical (hereafter TEC_{GNSS}), assuming that the thin ionized layer is at H=350 km above at the Earth's surface [52]. In order to reduce the impact of multipath, observations at elevation angles lower than 20° are masked out [53]. The use of a very dense network of GNSS receivers allows an ionospheric mapping with high spatial

resolution. To the scope, data acquired by RING network, having about 180 stations covering the Italian territory (Fig. 5-2), have been used.

Since the ALOS images are acquired at mid-latitude and during night-time, the ionosphere can be considered as "frozen" during a time interval of some minutes. [54] [55]. This means that the ionospheric plasma does not change significantly in its main characteristics (electron densities, dynamics) during time interval considered and corresponding data can be accumulated to improve the spatial resolution of the TEC mapping. A reasonable time interval of 5 minutes is here selected.
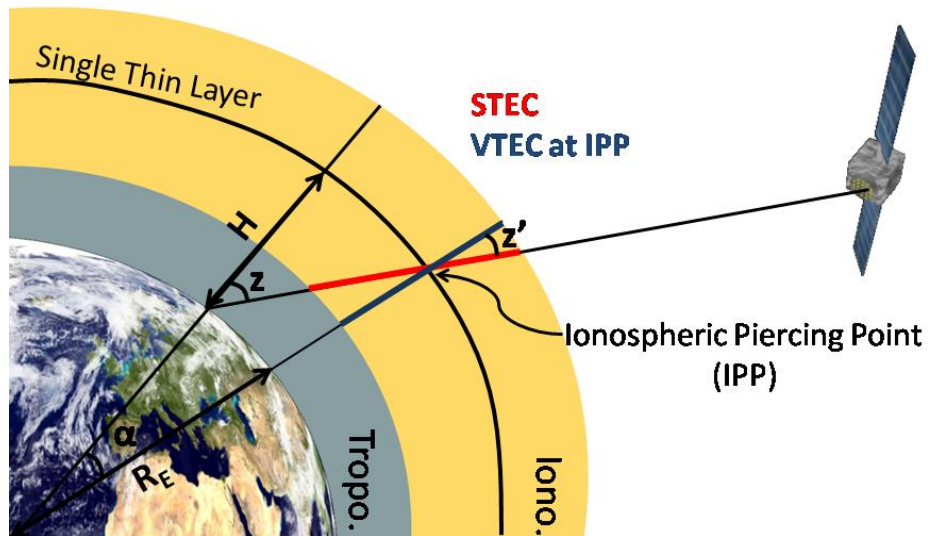
Fig. 5-1 Vertical TEC from slant TEC using single thin layer approximation.
http://gnss.be/ionosphere_tutorial.php
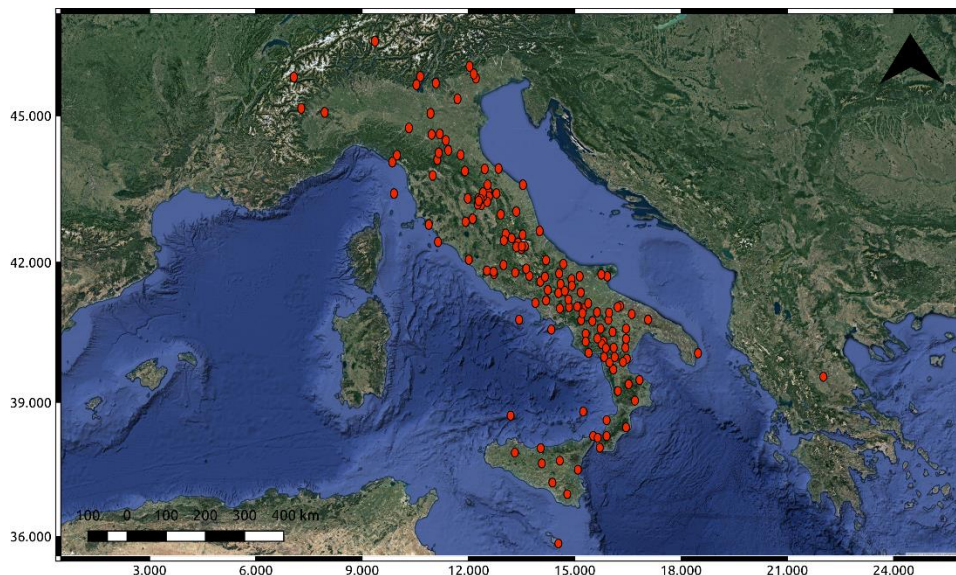
Fig. 5-2 RING (Rete Integrata Nazionale GPS) network (http://ring.gm.ingv.it/).

To obtain TEC_{GNSS} maps, representing the TEC distribution during the time of each ALOS passage, TEC values (30 sec sampling rate) at all IPP's (between 30°- 60° N and 5°- 20°E) during, 5 minutes around the ALOS passages are considered. These values at the IPP's are

then interpolated with the natural neighbour method [56]. Such method has been proven to be very effective in depicting strong TEC variability as occurring at equatorial regions [57]. The interpolation allows a mapping of the TEC_{GNSS} differences that is independent on the IPP geometry, being different at each considered times of the ALOS passages.

Hence, maps of interpolated TEC_{GNSS} are obtained over a regular grid of 0.01° in latitude x 0.01° in longitude. From these maps, only the portion of the ionosphere crossed during the image acquisition have been selected. To do this, the LOS for each pixel of the SAR image has been calculated, by using the satellite position vector in ECR (Earth-Centered Rotational) and then the intersection with the ellipsoid WGS84, projected at the height H=350 km (Fig. 5-3a), is calculated. The TEC_{GNSS} maps have been first interpolated over the whole geographical range indicated above and then the portion of interest has been selected to minimize border effects due to the interpolation. The resulting portion of the ionosphere crossed by ALOS-PALSAR signals (within the black rectangle) and the corresponding image area at ground (within the red rectangle) are plotted in (Fig. 5-3b).
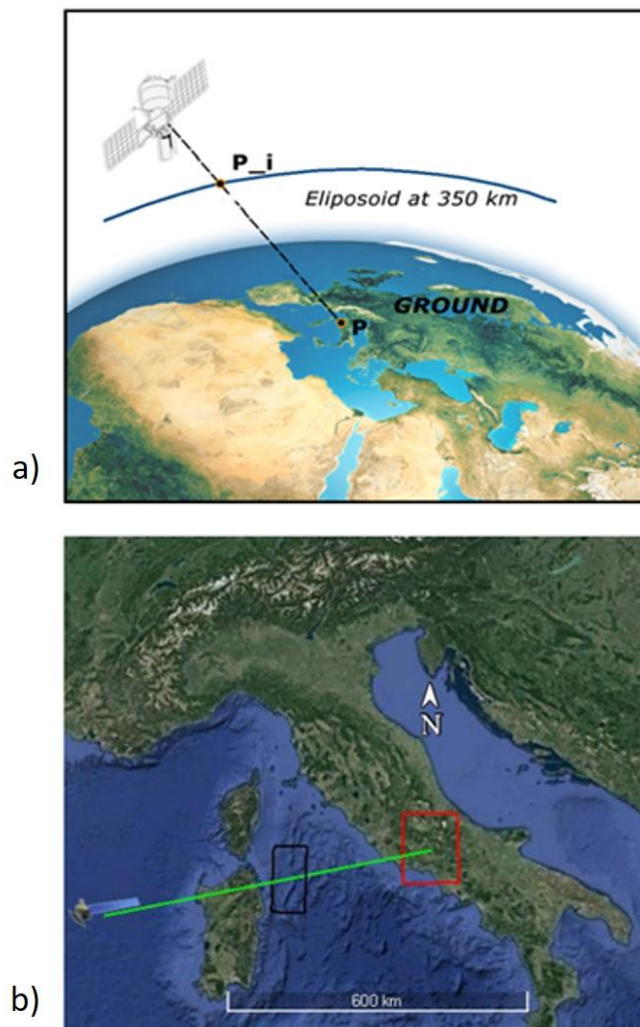
Fig. 5-3 Ionosphere crossed by SAR signal. Panel a sketches how to found the intersection P_i between the SAR signal and the ellipsoid project at 350 km (altitude of the thin ionospheric shell) given a point P at ground level Panel b shows the portion of the ionosphere (black rectangle) at 350 km crossed by ALOS-PALSAR signals and the corresponding image area at ground (red rectangle).

Being located at 350 km, the TEC_{GNSS} map so obtained has a size smaller than that of the InSAR image, located at ground. Moreover, the ΔTEC_{SAR} map resolution ($8.33° \cdot 10^{-4}$ in latitude x $8.33° \cdot 10^{-4}$ in longitude) is larger than the TEC_{GNSS} map ($0.01°$ in latitude x $0.01°$ in longitude). To overcome these discrepancy in the mapping resolution, TEC_{GNSS} map is resampled by applying a linear interpolation on both latitude and longitude directions to estimate TEC_{GNSS} values with increased spatial resolution up to $8.33° \cdot 10^{-4}$ for both the coordinates. To better compare ΔTEC_{SAR} map with TEC_{GNSS} temporal variation map, each grid point (Lat_{GNSS}, $Long_{GNSS}$) is expressed as function of the coordinates of the georeferenced InSAR image (Lat_{SAR}, $Long_{SAR}$). The new coordinates (Lat'$_{GNSS}$, Long'$_{GNSS}$) are obtained according to the following relations:

$$Lat'_{GNSS} = Lat_{GNSS} + (Lat_{SAR} - Lat_{GNSS})$$
$$Long'_{GNSS} = Long_{GNSS} + (Long_{SAR} - Long_{GNSS}) \qquad \text{5-8}$$

Finally, to account for the TEC temporal variation (pixel by pixel) between two ALOS passages, map of ΔTEC_{GNSS} are calculated according to the following formula:

$$\Delta TEC_{GNSS} = \left(TEC_{GNSS(M)} - TEC_{GNSS(S)} \right) - \left(TEC_{GNSS(Mp)} - TEC_{GNSS(Sp)} \right) \qquad \text{5-9}$$

where $TEC_{GNSS(M)}$ and $TEC_{GNSS(S)}$ are the TEC_{GNSS} maps relative to the master (suffix M) and slave (suffix S) passages of ALOS, respectively. $TEC_{GNSS(Mp)}$ and $TEC_{GNSS(Sp)}$ are the TEC_{GNSS} values at the coordinates of the pixel (p) choose to unwrap the interferogram.
In the following section, the analysis results are shown for the case studies under investigation.

5.3. Characterization of the geomagnetic and ionospheric conditions

A detailed characterization of the geomagnetic and ionospheric conditions is important to understand the impact of the ionosphere on SAR. The characterization of the geomagnetic conditions is provided in terms of Dst, Kp and AE/AL indices, while the ionospheric conditions are given by investigating ionograms provided by the ionosonde in Rome, being the closest available to the investigated area.

5.3.1 Geomagnetic conditions

To monitor the Earth's magnetic field response (both globally and locally) to the perturbations coming from the Sun, geomagnetic indices are used [58] [59].
These indices, derived by continuous and systematic recordings of the Earth's magnetic field components, allow describing the variations of the magnetic field both in quiet and perturbed conditions. Evidence of these "perturbations" are the magnetic storms showing typically three phases [59]:

- the sudden storm commencement and initial phases, being characterized by an increase of the horizontal component of the Earth's magnetic field due to the compression induced by the arrival of the shock. This is typical of the geomagnetic storm induced by Coronal Mass Ejections (CMEs). However, not all the geomagnetic storms have an initial and sudden commencement phase.
- the main phase, during which the horizontal component of the Earth's magnetic field is depressed;
- the recovery phase, during which the Earth's magnetic field returns to the conditions preceding the arrival of the disturbance and that can last for several days after the peak of the storm.

To highlight the possible presence of ionospheric irregularities during the SAR passages, the following indices have been selected as most significant: Kp, DsT, AU and AL.

Kp index is an indicator of the disturbance level of the Earth's magnetic field on a planetary scale. It is a three-hourly index given by the average of values recorded by 13 reference observatories located at sub-auroral latitudes. The Kp index scale ranges from 0 to 9 but each unity (except the extremes of the interval) is divided into three subunits in order to obtain a discrete scale of 28 values. The values of Kp are used by the American NOAA (National Oceanic and Atmospheric Administration) to define the scale of intensity of geomagnetic storms according to Table 5-4. An example of Kp is reported in figure Fig. 5-4 in which minor storm (G1) level is reached on October 25[th,] 2017.

Table 5-4 NOAA scale of geomagnetic storms

Scale	Description	Physical measure
G0	Quiet conditions	Kp<5
G1	Minor storm	Kp=5
G2	Moderate storm	Kp=6
G3	Strong storm	Kp=7
G4	Severe storm	Kp=8, including 9-
G5	Extreme stor	Kp=9
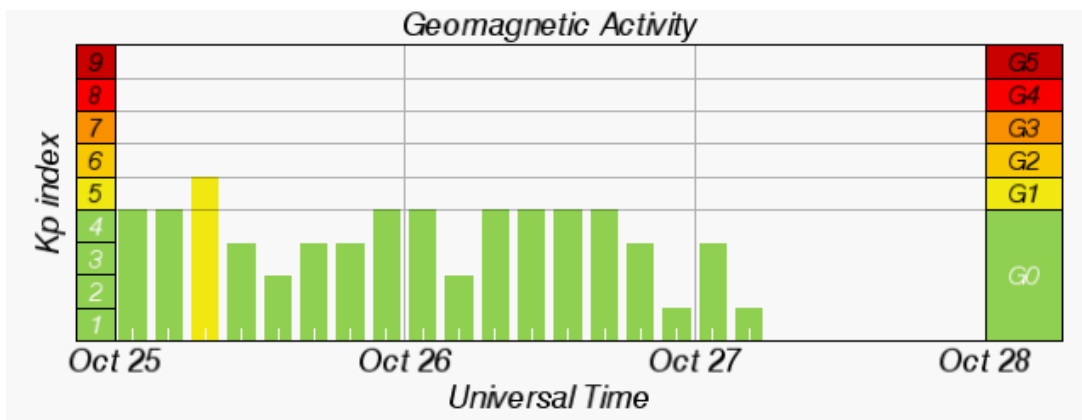
Fig. 5-4 Example of Kp (extracted from *http://www.swpc.noaa.gov/communities/space-weather-enthusiasts*)

Dst is a direct measure of the horizontal component of the Earth's magnetic field, which provides information on current systems in the equatorial plane enabling to monitor the level of magnetic storm on a global scale. Dst, calculated by hourly frequency, is obtained using four geomagnetic observers located sufficiently far from both the auroral and the equatorial electrojets (main electric currents which flowing in the ionosphere primarily in the E-region [60]), so that the contribution of each current can be recognized in the variation of the Dst.

Different thresholds of the Dst index correspond to a different level of intensity of magnetic storms, which are then classified as in Table 5-5. An example of a geomagnetic storm, as it appears on Dst index, is reported in Fig. 5-5together with the indication of the different storm development phases

Table 5-5: Classification of magnetic storms based on the value
of the geomagnetic index Dst [61]

Super storms	$D_{st} < -200nT$
Intense storms	$-200nT < D_{st} < -100nT$
Moderate storms	$-100nT < D_{st} < -50nT$
Weak storms	$-50nT < D_{st} < -30nT$

.
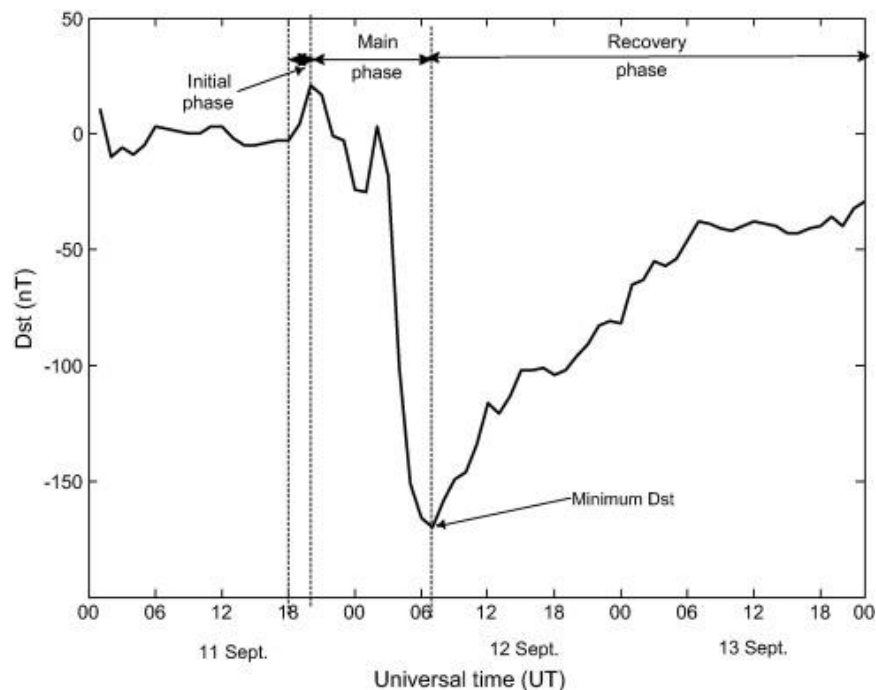
Fig. 5-5 Example of a geomagnetic storm as it appears on Dst index. The phases of the magnetic storm are also reported. (https://ars.els-cdn.com/content/image/1-s2.0-S0273117717306129-gr1.jpg).

The auroral activity indices (AU and AL) are designed to provide a global, quantitative measure of auroral zone magnetic activity. These indices are derived from geomagnetic variations in the horizontal component observed at selected (10-13) observatories along the auroral zone in the northern hemisphere.

In detail, for each given time (UT), at one-minute intervals:

- AU (Auroral Upper) is the uppermost envelope of the superposed geomagnetic horizontal component perturbations at auroral latitudes;
- AL (Auroral Lower) is the lowest envelope of the superposed geomagnetic horizontal component perturbations at auroral latitudes.

From a physical point of view:

- AU is a measure of the directly driven response of the magnetosphere to the changes of the interplanetary medium (solar wind) conditions.
- AL is a measure of the westward auroral electrojet (WEJ) that intensifies during substorms. Thus, AL provides a good tool to follow the evolution and the different phases of a substorm.

Low auroral activity is usually assumed when both AU and AL are below 400 nT in absolute value [62]. An example of AU and AL time profile characterized by geomagnetic storm and substorm conditions is reported in Fig. 5-6.
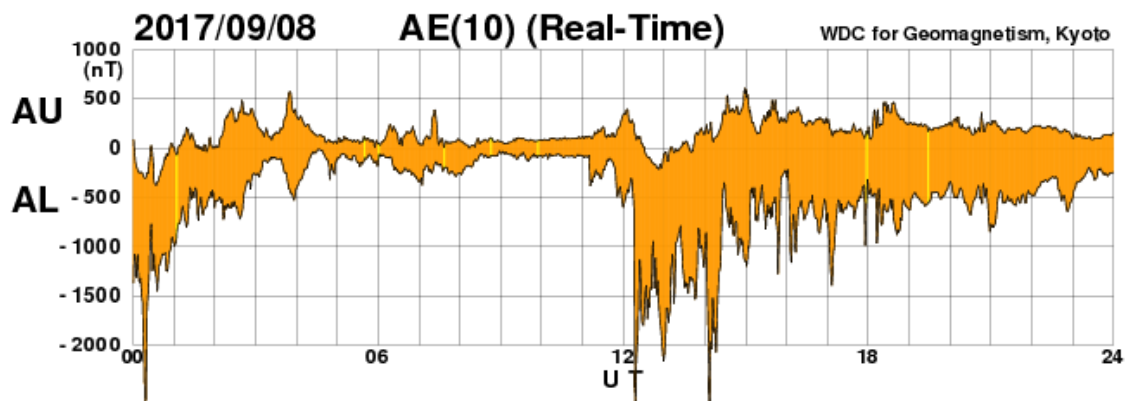
Fig. 5-6 Example of AU and AL values under geomagnetic storm and substorm conditions (extracted from *http://wdc.kugi.kyoto-u.ac.jp/ae_realtime/*).

5.3.2 Ionospheric conditions

Usually, ionospheric conditions are drawn by means of ionospheric indices that use both the solar and ionospheric information. The latter is used to tune the solar data (like the sunspot number R_{12} and the power flux of solar radio noise at wavelength 10.7 cm, $F_{10.7}$) to better represent the ionospheric changes under the solar forcing, e.g. its capability to reflect radio signals [59]. Thus, even if ionospheric indices are able to catch the variability on the longer periods, they may fail in providing the ionospheric behaviour over short time (minutes) and spatial (meters) ranges. This is the reason why the ionospheric characterization has been performed here by using the local information provided by ionosonde, which provides information about the main ionospheric parameters, about the

electron density profile and about the presence of ionospheric irregularities, like the sporadic E-layer. To be specific, an ionosonde is an active radar sounding the ionospheric medium working in the HF range. The transmitter sends short radio pulses with vertical incidence and variable frequency, usually in the range 0.5-25 MHz, while the receiver detects the reflected echo by the ionosphere in the altitude range typically between 100 and 800 km. The ionosphere reflects the transmitted pulses at different heights depending on the frequency of the transmitted signal (radio echo). The ionospheric sounding technique, thus, consists in transmitting a radio pulse vertically and measuring the time elapsed before receiving the echo. A sketch illustrating the principles of ionosonde sounding is reported in Fig. 5-7
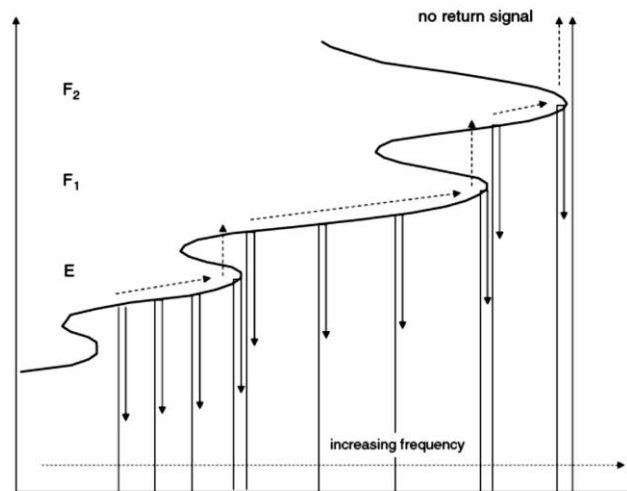
Fig. 5-7 Schematic representation of ionospheric sounding technique [63].

The result of an ionospheric sounding is called ionogram. It corresponds to a plot showing the trend of the virtual height as a function of frequency of the transmitted signal. The virtual height is given by the following equation: $h'=c\Delta t/2$, in with c is the speed of light and Δt is the echo delay, i.e. the time taken by the wave to carry out the Earth-ionosphere-Earth path. In an ideal ionogram, each ionosphere layer is represented by a curve ending with a vertical asymptote at the value $fo=f_N$, where fo is the critical frequency of the considered layer and f_N, is the plasma frequency; therefore $fo=f_N$ is the reflection condition for each ionospheric layer. An experienced operator can use ionograms to establish the most important ionospheric parameters. They are the critical frequency of the E, F1 and F2 layers (*foE, foF1* and *foF2*) and their virtual heights (*h'E*, *h'F1* and *h'F2*), the Maximum Usable Frequency at a distance of 3000 km (MUF(3000)F2), the virtual height (*h'Es*) and critical frequency (*foEs*) of the sporadic E layer. Many efforts have been made to overcome the need of an operator to manually scale the ionograms and software has been implemented for the automatic, real time scaling of ionograms. Two examples of widely used and well tested automatic scaling programs are the Automatic Real-Time Ionogram Scaling with True-height system (ARTIST, [64]), developed at the University of Lowell,

Center for Atmospheric Research and AUTOSCALA [65] [66] developed at the Istituto Nazionale di Geofisica e Vulcanologia.

An example of a typical ionograms is provided in panel a of Fig. 5-8, while an example of how an Es appears on an ionogram is in panel b of the same figure.
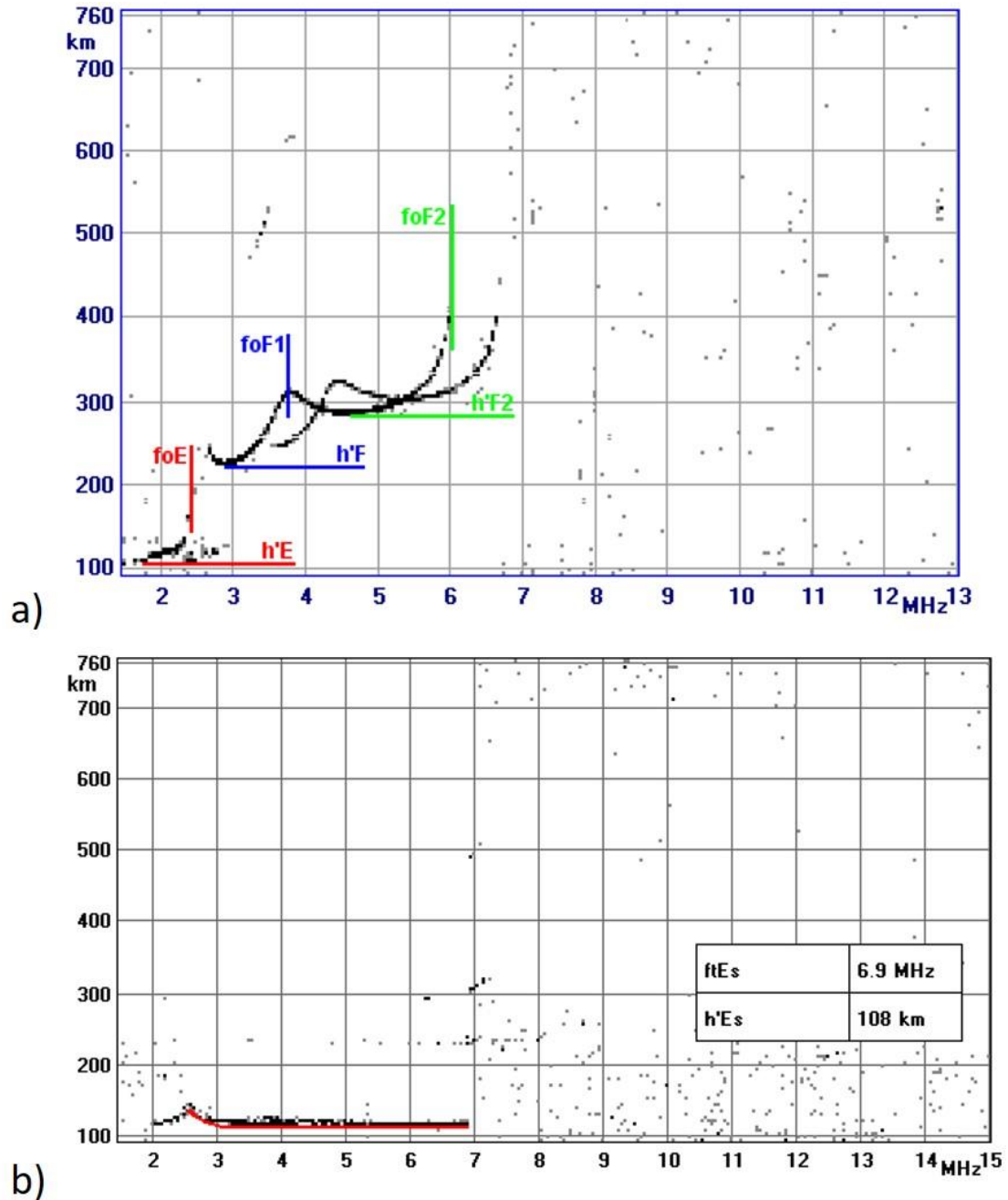
Fig. 5-8 Example of diurnal ionograms. In a) the virtual heights and the critical frequencies of the main ionospheric layers are shown. In b) an example of ionogram with sporadic E layer is shown. Es it is highlighted in red and its critical frequency and virtual height are shown in the table. http://roma2.rm.ingv.it/en/themes/24/ionospheric_sounding

38

6 ANALYSIS OF THE CASE STUDIES: RESULTS AND DISCUSSION

In this chapter, the case studies reported in Table 5-1 are analysed and discussed in detail. For each case study, the geomagnetic and ionospheric conditions are evaluated. The geomagnetic conditions are investigated through the simultaneous use of indices of geomagnetic activities, i.e. AU/AL, Kp and DsT (see section 5.3.1). To support the ionospheric characterization, ionospheric parameters and electron density profiles are used as obtained from the DPS-4 digisonde located in INGV's (Istituto Nazionale di Geofisica e Vulcanologia) headquarter in Rome. The digisonde is a type of ionosonde manufactured by the Lowell Digisonde International (http://www.digisonde.com/). In this work, ionograms from the Rome digisonde are autoscaled by the ARTIST software.

Furthermore, for each case event, a check if the tropospheric effect can be considered as constant is performed to allow retrieving ΔTEC from InSAR observations. As already mentioned in section 5, the correlation factor between the interferometric phase and the integral of the azimuth shifts is the benchmark to understand if the constant troposphere approximation stands. Then ΔTEC_{SAR} is then compared with ΔTEC_{GNSS} aiming then at finding, if feasible, the empirical relationship between the two.

To summarize, the analysis of each case event is composed by the following steps:

Step 1. Characterization of the geomagnetic and ionospheric conditions to assess if ionospheric irregularities are present in the considered area and if they are linked to the forcing from the geospace;

Step 2. Calculation of the azimuth shifts Δx from the InSAR image, to check for the streaking effect;

Step 3. Calculation of the integral of Δx and of the interferometric phase $\Delta\varphi$;

Step 4. Correlation plot between $\Delta\varphi$ and the integral of Δx to check if the tropospheric phase is constant over the image. To do this, the Pearson's correlation factor $R1$ between the two quantities is calculated: in the ideal conditions $|R1|=1$, meaning constant tropospheric phase;

Step 5. Calculation of the TEC difference between master and slave from InSAR, ΔTEC_{SAR};

Step 6. Calculation of the TEC difference from GNSS, ΔTEC_{GNSS}, considering a time window of 5 minutes centered around the times of the ALOS passages corresponding to the master and slave images;

Step 7. Correlation plot between ΔTEC_{SAR} and ΔTEC_{GNSS}, calculation of the Pearson's coefficient $R2$ between the two and ddetermination of the linear relation.

To demonstrate the validity of the proposed method, the correlation between ΔTEC_{SAR} and ΔTEC_{GNSS} is derived also in the cases in which the constant troposphere approximation is not valid, i.e. in the case in which $|R1|$ (step 4) results into not correlation between $\Delta\varphi$ and the integral of Δx. In such case, ΔTEC_{SAR} and ΔTEC_{GNSS} are expected to decorrelate too.

This chapter is organized as follows: sections 6.1 and 6.2 report the assessment of the geomagnetic and ionospheric conditions, respectively, for all the periods taken into account for the analysis (step 1); while sections 6.3 to 6.7 report, for each considered case, the results of the steps 2 to 7. A summary of the results is provided in section 6.8, while section 6.9 reports the first attempt at mitigating the ionospheric information in the InSAR imaging by using the information derived from GNSS. Section 6.10 closes the chapter by critically reviewing the assumption of the 5-minutes window around ALOS passages for the GNSS data selection.

6.1. Overall geomagnetic conditions

The overall geomagnetic conditions affecting the passages of ALOS over Italy on 1 July 1st, 2007; August 16th, 2007; October 1st,200; April 8th, 2010; May 24th, 2010 and July 9th , 2010 (Table 5-1) are described.

July 1st 2007 is characterized by very low geomagnetic activity, as reported in Fig. 6-1. In fact, the AU and AL time profiles (upper plot) report no meaningful auroral activity in correspondence with the time of the ALOS passage (magenta line). In the specific, both AU and AL are below 400 nT in absolute value [62]. In addition, the DsT index time profile (middle plot) indicates very low geomagnetic activity, as it is in the range -20 to 20 nT [61] and no signatures of geomagnetic storms are present in correspondence with the ALOS passage. Such quiet conditions are also confirmed by Kp index (bottom plot), being very low in the considered period (Kp<5). The rising of AU/AL and Kp indices starting from mid-day of July 3rd is due to a fast stream of solar wind, however not affecting the ionospheric condition in the considered case studies.

During August 16th 2007 no signatures of geomagnetic storm are present in correspondence with the ALOS passage (Fig. 6-2, magenta line), although the plots of the geomagnetic index show that, starting from mid-day of August 10th, the Earth enters in a high-speed solar wind stream, and this causes high-latitude geomagnetic storms. In fact, AU/AL indices are greater than 400 nT in absolute value, the DsT is below -20 nT and the Kp index is greater than 4. After August 12th, both AU and AL are below 400 nT and also the DsT index time profile is in the range -20 to 20 nT. Such quiet conditions are also confirmed by Kp index that is lower than 4. Small auroral activity is also present between 15 and early 16 August, with no meaningful expected effects at mid-latitudes.

October 1st 2007 is characterized by the exit from intermittent geomagnetic storms (Fig. 6-3), started on September 27th and triggered by a solar wind stream flowing from a coronal hole developed the September 26th. This period of intermittency does not significantly affect the ionospheric condition of the ALOS passage at mid-latitude. These "perturbed conditions" can be seen especially on September 27th and 29th when AL and Kp reach the values of -600 nT and 5, respectively. The DsT too minimizes on September 29th (-40 nT). A solar wind stream flowing from a coronal hole on October 1st also occurred inducing another geomagnetic storm at the end of 2 October (AL= -400 nT; DsT about -30 nT).

Fig. 6-1 Variation of AU/AL auroral (top), DsT (middle) and Kp (bottom) indices, 15 days around the ALOS passage on 01/07/2007 (World Data Center for Geomagnetism of Kyoto). Purple line identifies the time of the ALOS passage.
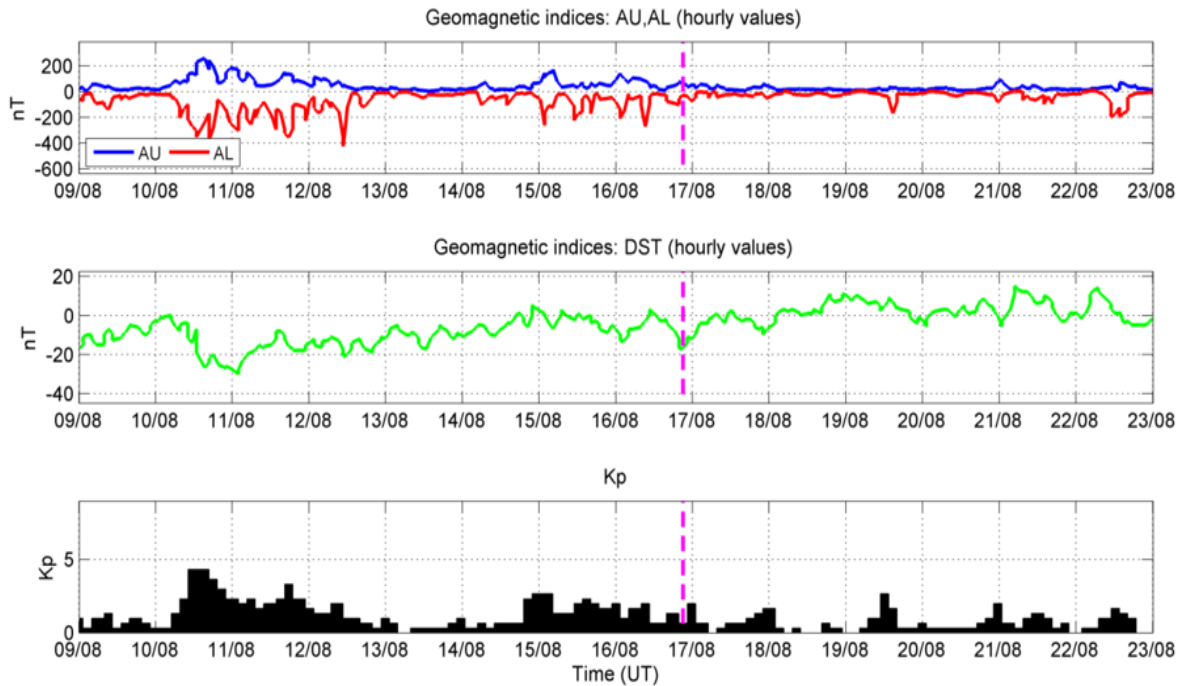
Fig. 6-2 Variation of AU/AL auroral (top), DsT (middle) and Kp (bottom) indices, 15 days around the ALOS passage of 16/08/2007 (World Data Center for Geomagnetism of Kyoto). Purple line identifies the time of the ALOS passage.
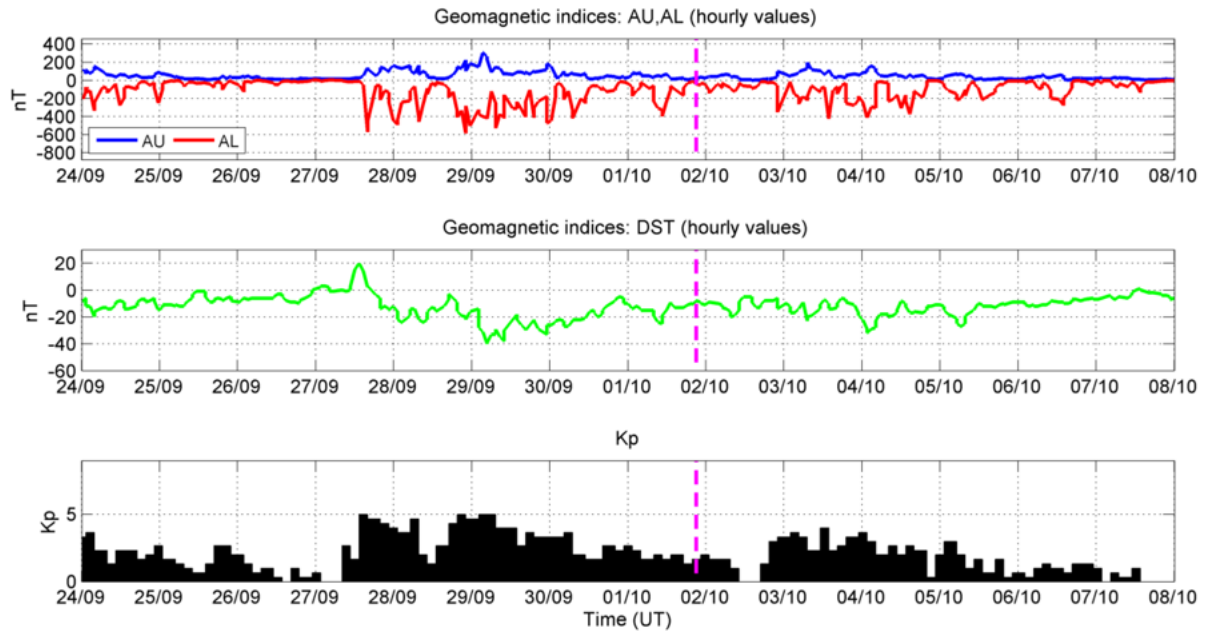
Fig. 6-3 Variation of AU/AL auroral (top), DsT (middle) and Kp (bottom) indices, 15 days around the ALOS passage of 01/10/2007 (World Data Center for Geomagnetism of Kyoto). Purple line identifies the time of the ALOS passage.

April 8th 2010 is in the recovery phase of the magnetic storm occurred around mid-day of April 5th (Fig. 6-4). During the ALOS passage, AU and AL are about 200 nT and -500 nT, respectively, DsT and Kp are about -40nT and 4. The storm of April 5th is due to the solar wind stream and it is characterized by AL equal to about -1200 nT and Kp equal to about 7. The DsT is lower than -50 nT. Around the mid-day of April 11th, a coronal mass ejection hits Earth's magnetic field causing another geomagnetic storm. The AL and is lower than -500 nT. DST is lower -50 nT and. Kp is greater than 5.

From the geomagnetic point of view, May 24th 2010 is characterized by very low geomagnetic activity (Fig. 6-5). In fact, the AU and AL time profiles reports no meaningful auroral activity in correspondence with the time of the ALOS passage (magenta line). In addition, the DsT index time profile indicates very low geomagnetic activity, as it is well in the range -20 to 20 nT and no signatures of geomagnetic storms are present in correspondence of the ALOS, passage. Such quiet conditions are also confirmed by Kp index being very low (Kp<5) in the considered period. On May 29th, the interplanetary magnetic field (IMF) tilted south and opened a crack in Earth's magnetosphere. Solar wind poured in and it has fuelled a geomagnetic storm. The AL and the DsT indices are about -1000 nT and -70 nT, respectively. The Kp index is then greater than 5.

July 9th 2010 is characterized by very low geomagnetic activity (Fig. 6-6). In fact, the AU and AL time profiles report no meaningful auroral activity in correspondence with the time of the ALOS passage (magenta line) and also the DsT and Kp are at low levels.
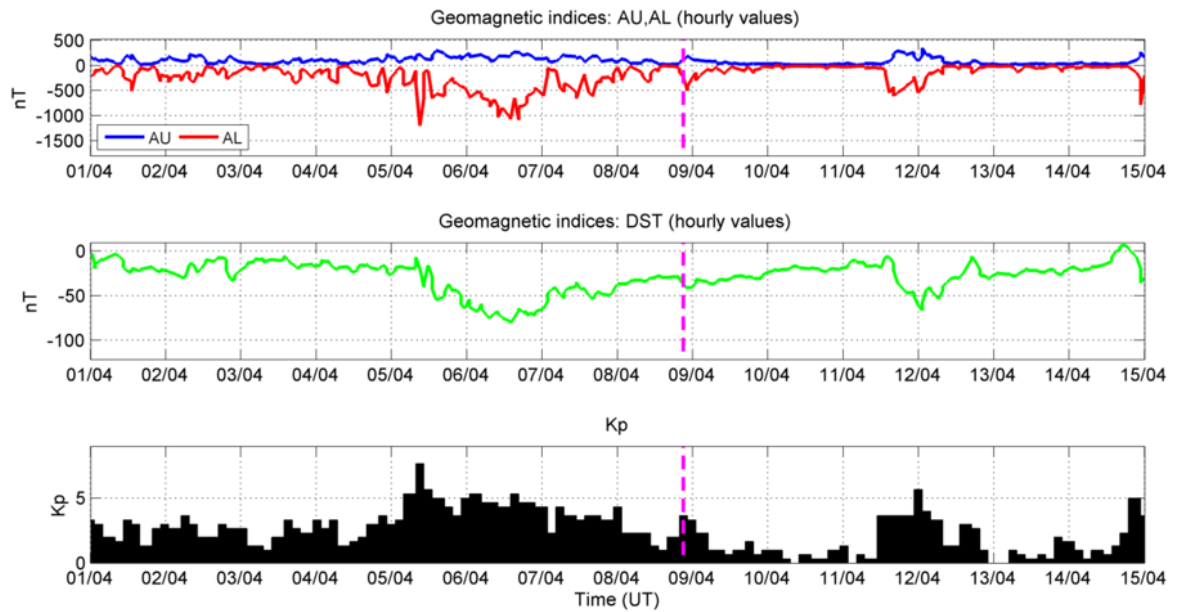
Fig. 6-4 Variation of AU/AL auroral (top), DsT (middle) and Kp (bottom) indices, 15 days around the ALOS passage of 08/04/2010 (World Data Center for Geomagnetism of Kyoto). Purple line identifies the time of the ALOS passage.
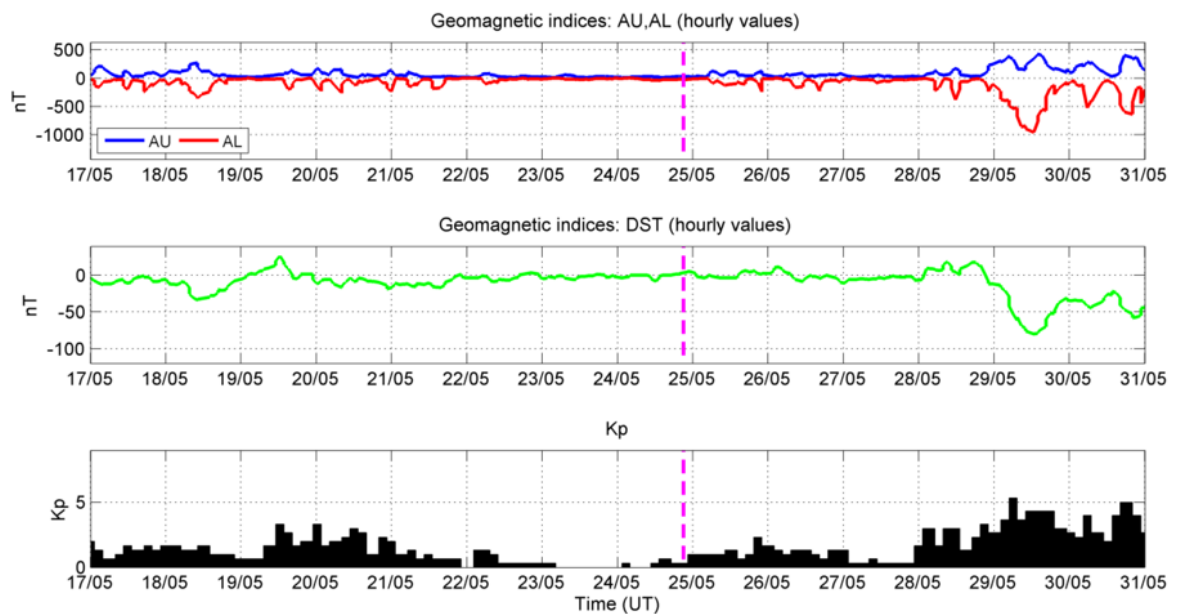
Fig. 6-5 Variation of AU/AL auroral (top), DsT (middle) and Kp (bottom) indices, 15 days around the ALOS passage of 24/05/2010 (World Data Center for Geomagnetism of Kyoto). Purple line identifies the time of the ALOS passage.
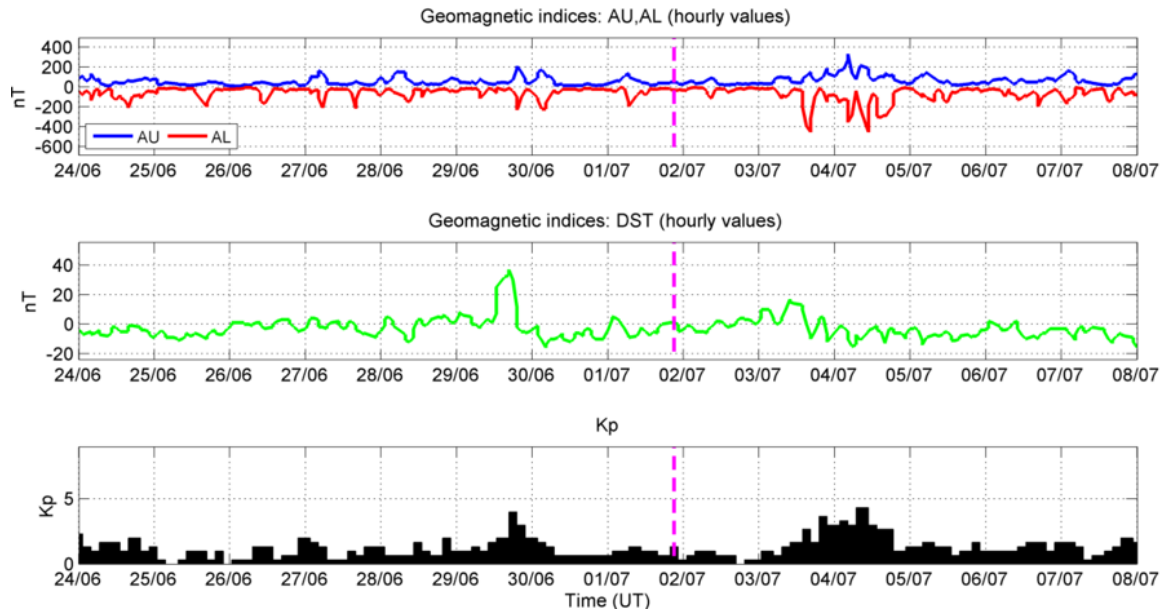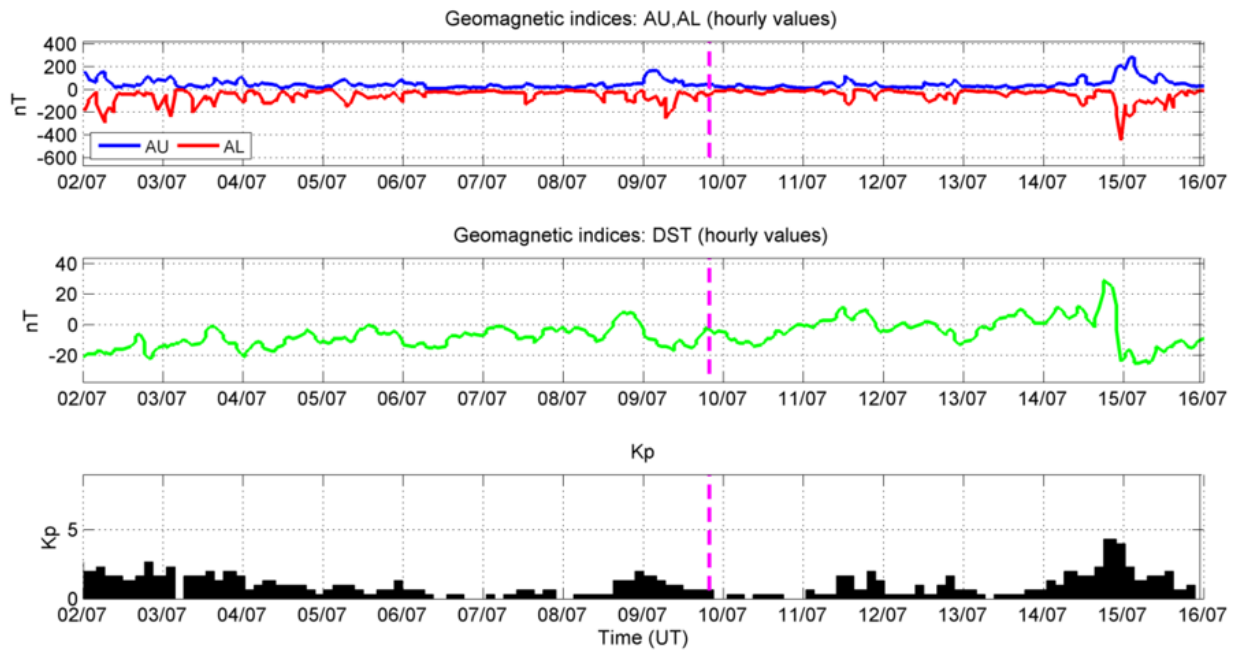
Fig. 6-6 Variation of AU/AL auroral (top), DST (middle) and Kp (bottom) indices, 15 days around the ALOS passage of 09/07/2010 (World Data Center for Geomagnetism of Kyoto). Purple line identifies the time of the ALOS passage.

6.2. Overall ionospheric conditions

After the assessment of the geomagnetic conditions, to characterize the ionospheric environment before, during and after the image acquisition times, four ionograms (from 21:00 to 21:45, i.e. centred around the ALOS passage) have been analysed for each case study. They are obtained from the DPS-4 ionosonde in the Rome observatory in the INGV headquarter (41.8° N, 12.5° E).

The ionograms of July 1st, 2007, are shown in panels a-d of Fig. 6-7. Such ionograms show a critical frequency of the F2 layer (*foF2*) ranging from 5.5 to 6 MHz and a virtual height (*h'F*) of about 250 km. A weak sporadic-E layer, with a critical frequency, *foEs*, of about 3 MHz, occurs during the image acquisition, around 100 km.

August 16th, 2007 is characterized by a *foF2* of about 4.5 MHz, and a virtual height ranging from 212 km to 280 km (Fig. 6-8). During the image acquisition, an Es occurs, at a virtual height, *h'Es*, of about 100 km and with *foEs* of about 5 MHz. The ionograms of October 1st are characterized by the sole presence of the expected night-time ionospheric F-layer as shown in Fig. 6-9, panels a and d. These ionograms are typical of the autumn, nighttime ionosphere at mid-latitude, with *h'F* ranging between 235 and 268 km and foF2 between 2.7 MHz and 2.9 MHz.

April 8th, 2010 is characterized by a *foF2* of about 3.8 MHz, and a virtual height ranging from 275 km to 300 km (Fig. 6-10). During the image acquisition, an Es occurs, having *h'Es* of about 100 km and with *foEs* of about 3.5 MHz.

The ionograms of May 24th (Fig. 6-11), show an Es with a critical frequency ranging between 5.8 MHz (at 21.45 UT) to 9.2 MHz (at 21.00 UT). This *Es* is totally blanketing,

so the vertical electron density profile cannot be retrieved. The ionograms show that there are three multiple reflections.

Ionograms of July 9th are characterized by the sole presence of the expected night-time ionospheric F-layer as shown in Fig. 6-12, panels a and b. The *h'F* is about 216 km and *foF2* decreases over time from 5.6 MHz (at 21:00 UT) to 5.3 MHz (at 21:15 UT). From 21:30 UT an *Es* appears (Fig. 6-12, panel c and d) at an height of about 100 km. The *foEs* increase from 2.2 Mhz (at 21:30 UT) to about 3 Mhz (at 21:45 UT).

Fig. 6-7 Ionograms of July 1st, 2007, obtained by using ionosonde DPS-4 located in Rome. In a) is shown the ionogram at 21:00 UT, in b) at 21:15, in c) at 21:30, in d) at 21:45. The time of ALOS passage is around 21:29. The black line is the modelled vertical electron density profile

Fig. 6-8 Ionograms of August 16th, 2007, obtained by using ionosonde DPS-4 locates in Rome.In a) is shown the ionogram at 21:00 UT, in b) at 21:15 UT, in c) at 21:30 Ut, in d) at 21:45 UT. The time of ALOS passage is around 21:29 UT. The occurrence of Es can be well recognized. The black line represents the modelled vertical electron density profile.

Fig. 6-9 Ionograms of October 1st, 2007, obtained by using ionosonde DPS-4 located in Rome. In a) is shown the ionogram at 21:00 UT, in b) at 21:15 UT, in c) at 21:30 UT, in d) at 21:45 UT. The time of ALOS passage is around 21:29 UT. The black line is the modelled vertical electron density profile.

Fig. 6-10 Ionograms of April 8th 2010, obtained by using ionosonde DPS-4 locates in Rome. In a) is shown the ionogram at 21:00 UT, in b) at 21:15 UT, in c) at 21:30 UT, in d) at 21:45 UT. The time of ALOS passage is around 21:29 UT. The black line represents the modelled vertical electron density profile.
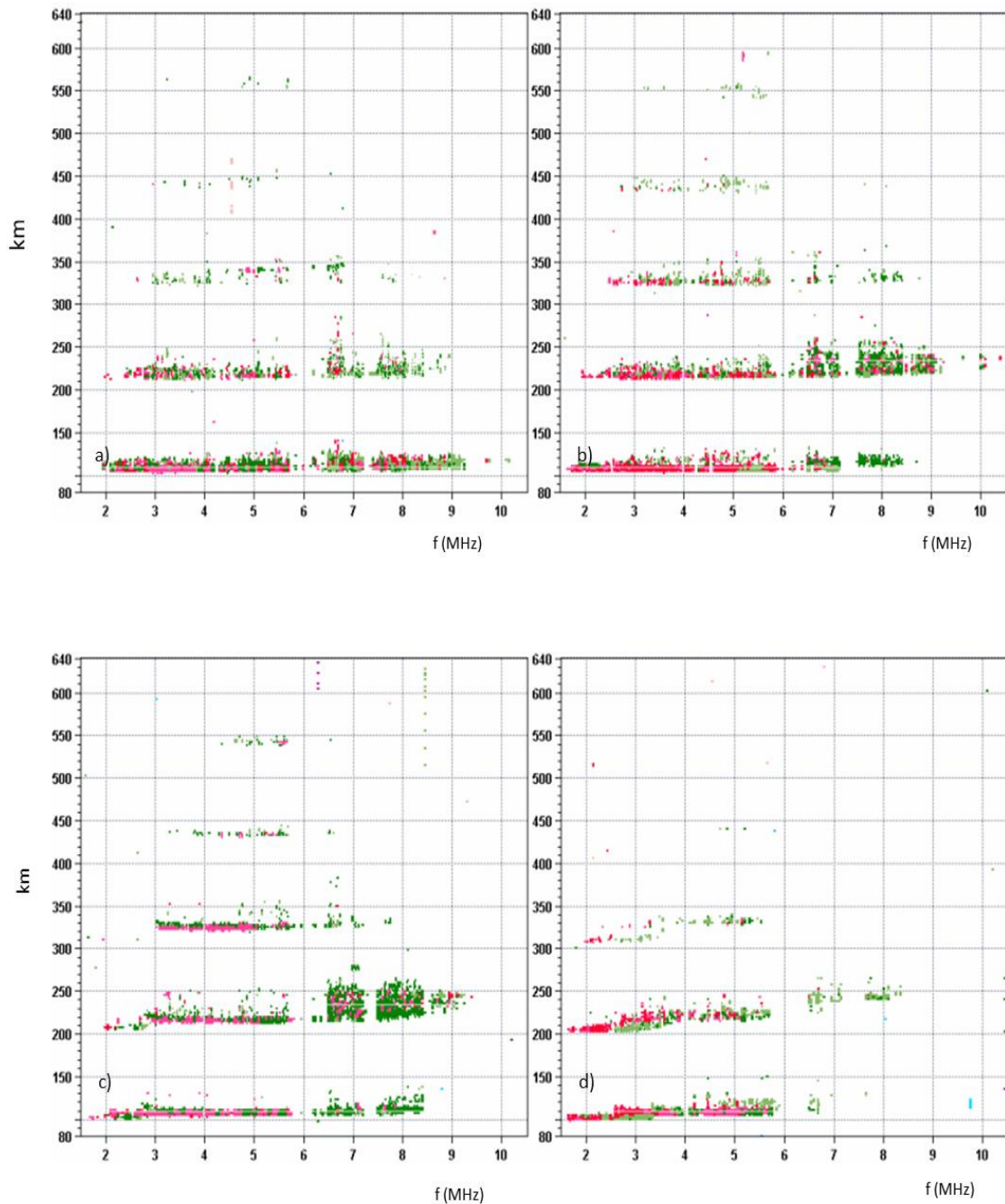
Fig. 6-11 Ionograms of May 24th 2010, obtained by using ionosonde DPS-4 locates in Rome. In a) is shown the ionogram, at 21:00 UT, in b) at 21:15 UT, in c) at 21:30 UT, in d) at 21:45 UT. The time of ALOS passage is around 21:29 UT. The occurrence of blanketing Es can be well recognized.
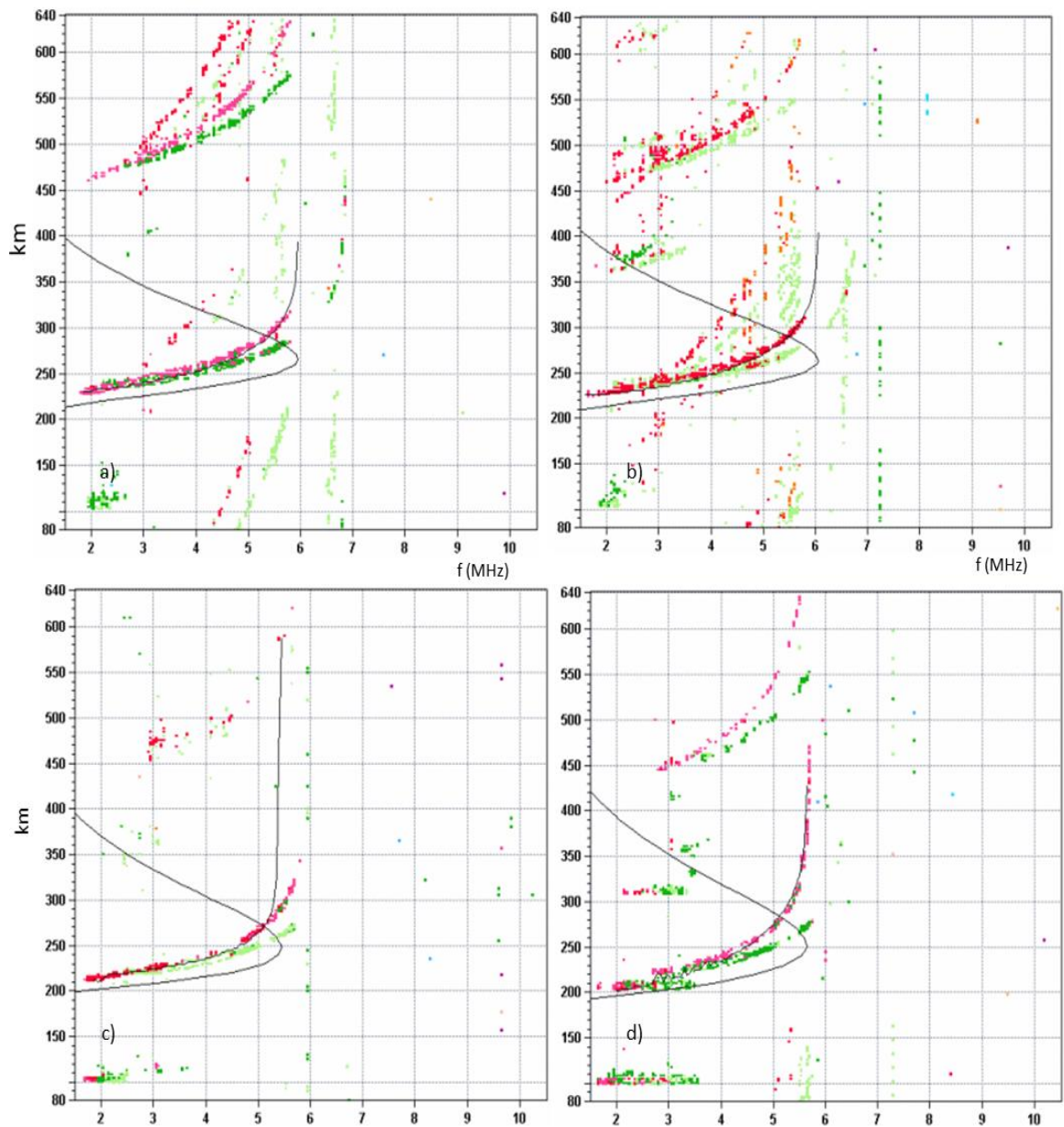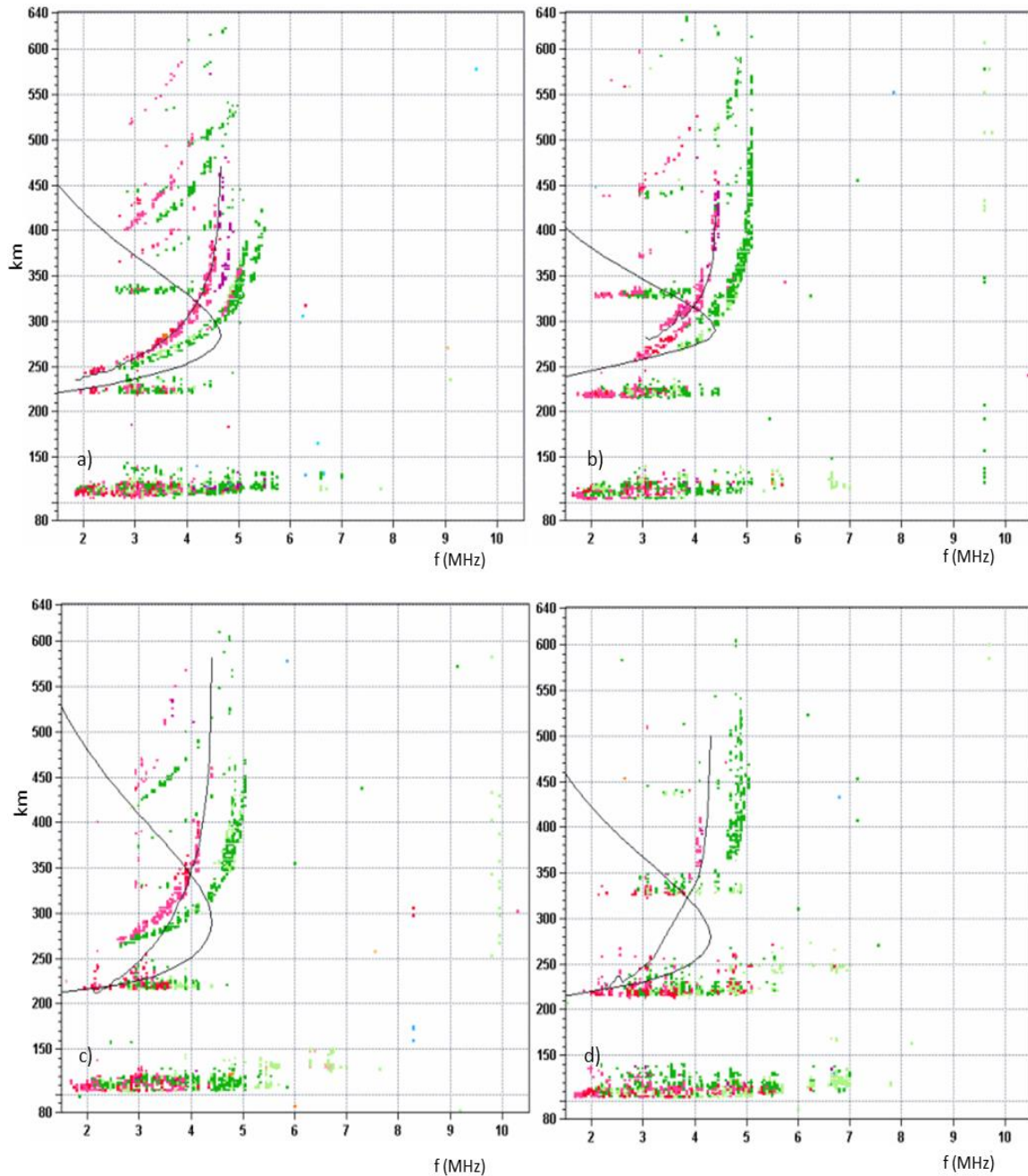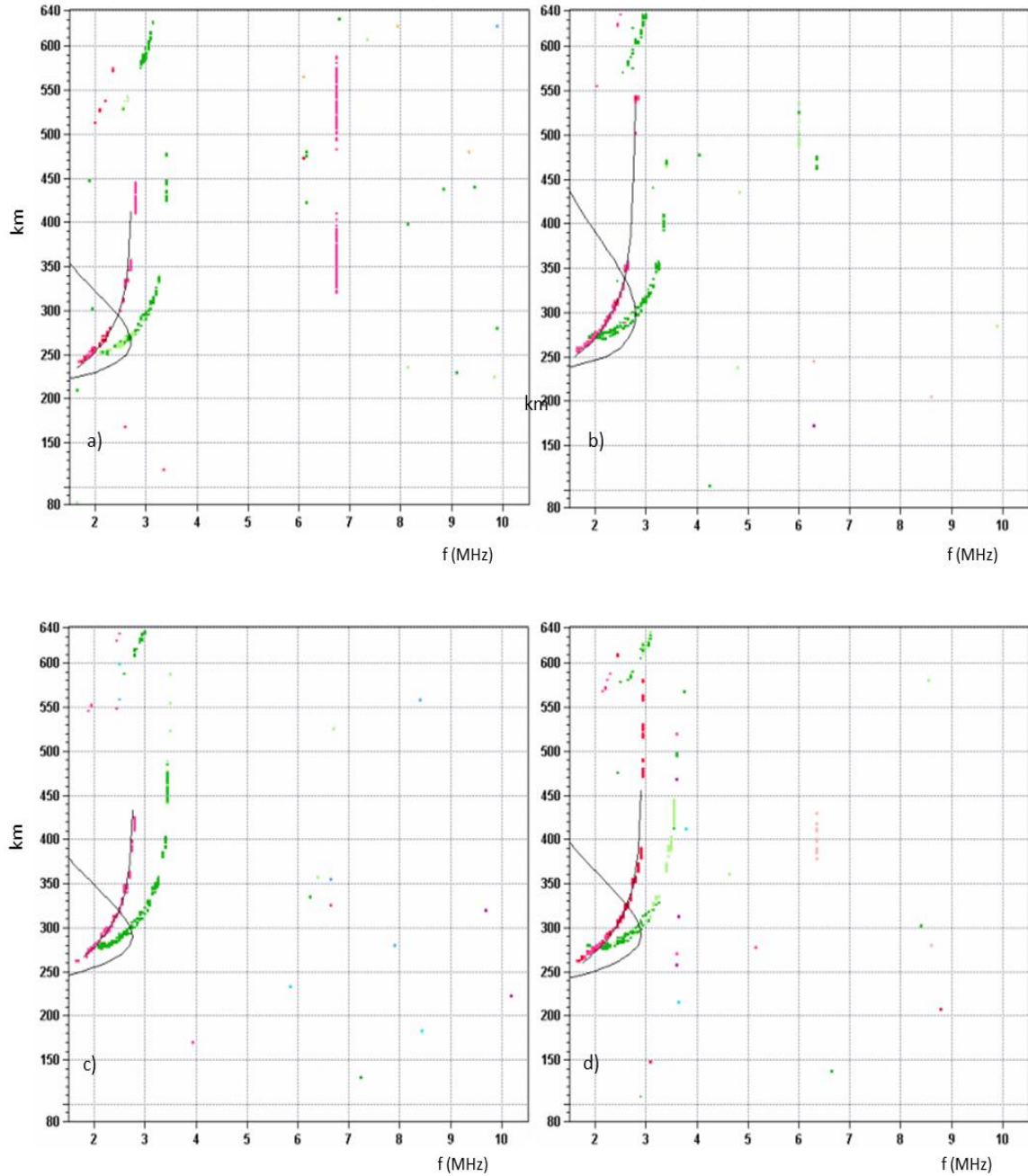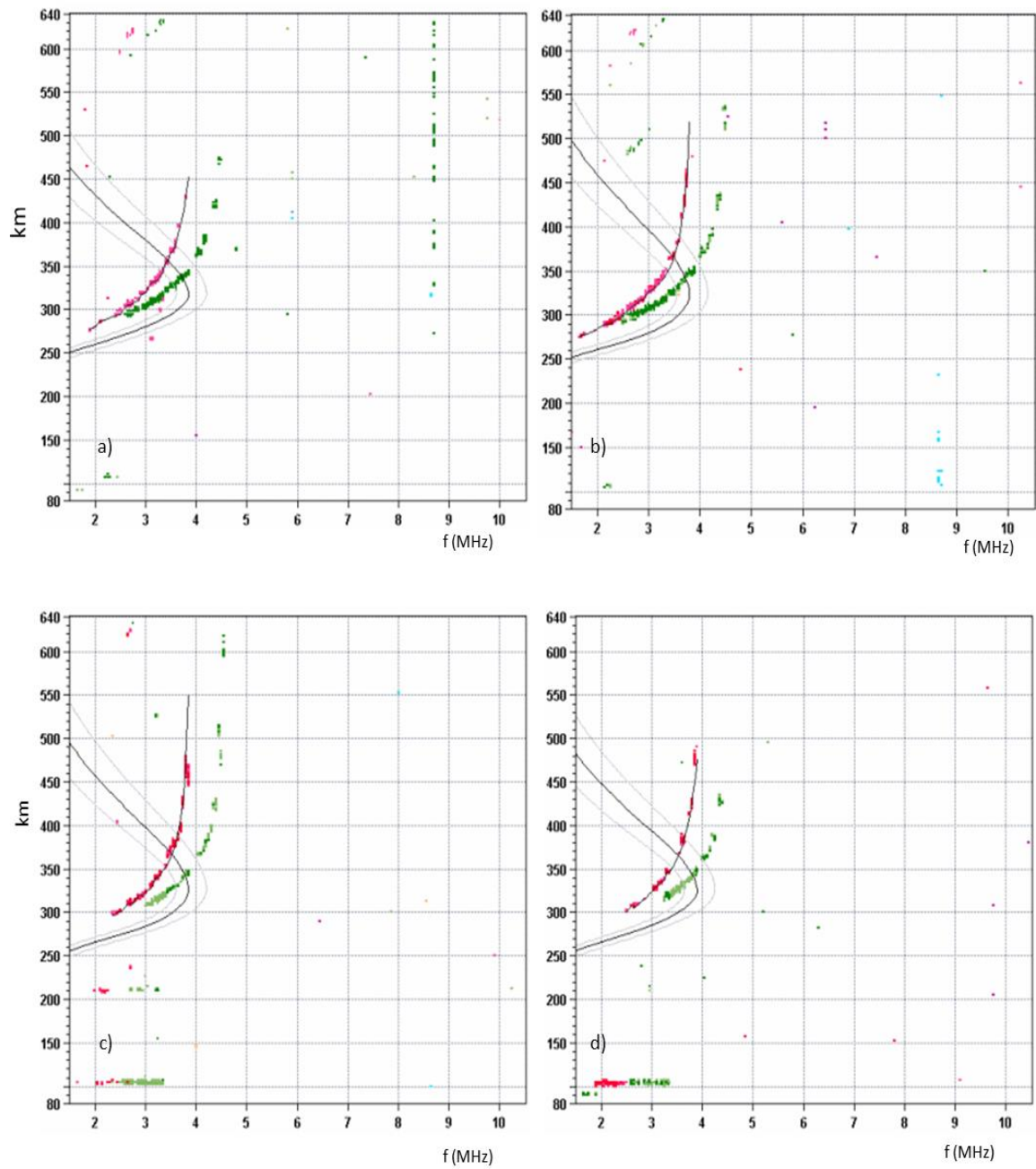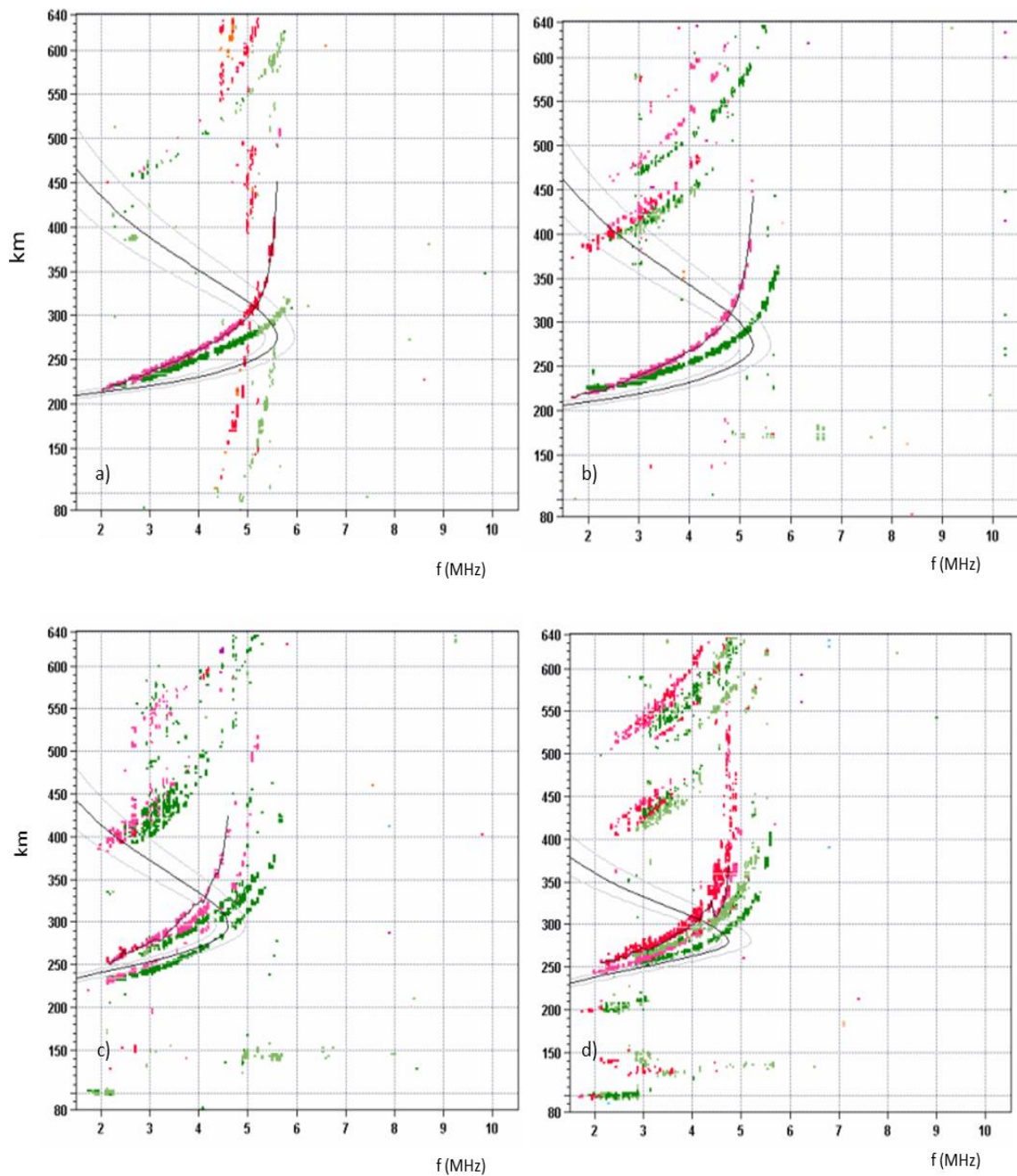
Fig. 6-12 Ionograms of July 9th, 2010, obtained by using ionosonde DPS-4 locates in Rome. In a) is shown the ionogram at 21:00 UT, in b) at 21:15 UT, in c) at 21:30 UT, in d) at 21:45 UT. The time of ALOS passage is around 21:29 UT. The black line represents the modelled vertical electron density profile

6.3. Case 1: 1 July 2007 – 16 August 2007

In this first case study, the master and slave images are acquired the July 1st, 2007 and the August 16th, 2007, respectively, around 21:29 UT. Before retrieving ΔTEC_{SAR}, it is necessary to assess if the tropospheric contribution to the interferometric phase is constant.

6.3.1 Approximation of constant troposphere

If correlation between the integral of the azimuth shifts (Fig. 6-13b) and the interferometric phase (Fig. 6-13 c) stands, $\Delta\varphi_{tropo}$ is constant in equation 5-1.

The georeferenced results of the azimuth shifts, reported in Fig. 6-13a, vary from about -1 m to 1 m. An azimuth streak, due to the ionosphere, can be recognized from about 41.6°N to 42°N (in blue).

The integral of the shifts (Fig. 6-13 b) shows that from 41.8°N to 42°N, negative values (blue) are predominant. Below 41.8°N, the map can be divided in two part around 13.9°E: the left side, in which negative values (blue) are predominant, the right, in which positive (red) values principally. Narrow regions of almost null values (white) are also present.

The unwrapped phase (Fig. 6-13c) is characterized by positive values (red) in the upper part of the map, null (white) and negative (blue) values from the lower boundary of the map to about 41.5°N. The unwrapped phase ranging from about -3.5 rads to 8.0 rads. The Pearson's coefficient obtained by correlating the integral of the shifts and unwrapped phase is $R1$=-0.6 (Fig. 6-14). The deviation from the ideal case ($|R1|$=1) suggests that: i) the impact to the interferometric phase is not fully of ionospheric origin, and ii) the integration numerical error of equation 5-3 is not negligible. Bearing this in mind, ΔTEC_{SAR}, is then retrieved from the interferometric phase by applying equation 5-4.

6.3.2 Comparison between ΔTEC_{SAR} and ΔTEC_{GNSS}

Fig. 6-15a shows ΔTEC_{SAR} values map obtained from the unwrapped phase shown in Fig. 6-13. ΔTEC_{SAR} ranging from about -0.2 TECu to 0.6 TECu and its map is characterized by positive (red) values in the upper part of the map, null (white) and negative (blue) values from the lower boundary of the map to about 41.5°N.

The ΔTEC_{GNSS} values (Fig. 6-15 b) ranging from about -0.45 to 1 TECu and the corresponding map shows:

- Positive (red) values in the upper part of the map, from 41.6°N to 42.1°N and in the central part around 41.6°N and 14.3°E;
- negative (blue) values in lower part of the map from 41.1 to 41.5 and in the upper part, from 41.6°N-13.7°E to 41.9°N-14.3°E.
- null (white) values around the positive areas.

This two independent maps are quite well correlated ($R2$=0.7) and ΔTEC_{SAR} values are about 0.43 times ΔTEC_{GNSS} value (Fig. 6-16). The Root Mean Square Error ($RMSE$) is about ±0.14 TECu.

Fig. 6-13 Azimuth shifts a), integral of the azimuth shifts b) and unwrapped phase c) obtained by using as master (July 1st,2007) and as slave images (August 16th, 2007) The shifts are obtained by using MAI technique. Colorbar for the panel a) expresses the displacement in meters. To compare panel b) with panel c), both the integral of the azimuth shifts and the unwrapped phase are expressed in radians.

52

Fig. 6-14 Scatter plot of Integral of azimuth shifts vs unwrapped phase for the first case study (master: July 1st, 2007 and slave: August 16th, 2007). In red, the regression line is plotted.

Fig. 6-15 ΔTEC$_{SAR}$ (a) and ΔTEC$_{GNSS}$ (b). The colorbars express, in TECu, the TEC variation between July 1st, 2007 and August 16th, 2007.

Fig. 6-16 Scatter plot of ΔTEC_{SAR} vs ΔTEC_{GNSS} for the first case study (master: July 1st, 2007 and slave: August 16th, 2007. In red, the regression line is plotted. Its angular coefficient, m_{rl}, and its intercept q_{rl} are also shown together with the *RMSE*.

6.4. Case 2: 1 July 2007 – 1 October 2007

In this second case study, the master and slave images are acquired the July 1st, 2007 and the October 1st, 2007, respectively, around 21:29 UT. In the next subsections, the condition to consider the tropospheric effect negligible and the comparison between ΔTEC_{SAR} and ΔTEC_{GNSS} are investigated.

6.4.1 Approximation of constant troposphere

In this case study, the azimuth shift ranging from about -0.4 m to 0.6 m. The georeferenced results of the azimuth shifts, reported in Fig. 6-17a, shows three areas: two positives (red) in the upper part of the map (up to about 41.8°N) and in the lower part of the map (below to about 41.4°N), one negative (blue) in the central part of the map. No azimuth streaking, due to the ionosphere, can be recognized. Thus, we expect that no correlation stands between the azimuth shifts and the unwrapped phase.

The integral of the azimuth shifts for the second case study (Fig. 6-17b) is characterized by positive (red) values except for two narrow regions around 41.8°N, where there are two negative (blue) areas, surrounded by two narrow areas of null (white) values.

The corresponding unwrapped phase map (Fig. 6-17c) is characterized mostly by positive values in upper part of the map. Areas with almost null and negative values are present in the lower part of the map.

As expected, the correlation coefficient, between integral of the azimuth shifts and the unwrapped phase, is *R1*=0.2 (Fig. 6-18). This confirms that the tropospheric effect cannot be assumed as constant over the image. In this case, ΔTEC_{SAR} cannot be retrieved with the proposed method. For a confirmation, ΔTEC_{SAR} is anyway calculated and no correlation with ΔTEC_{GNSS} is expected to stand.

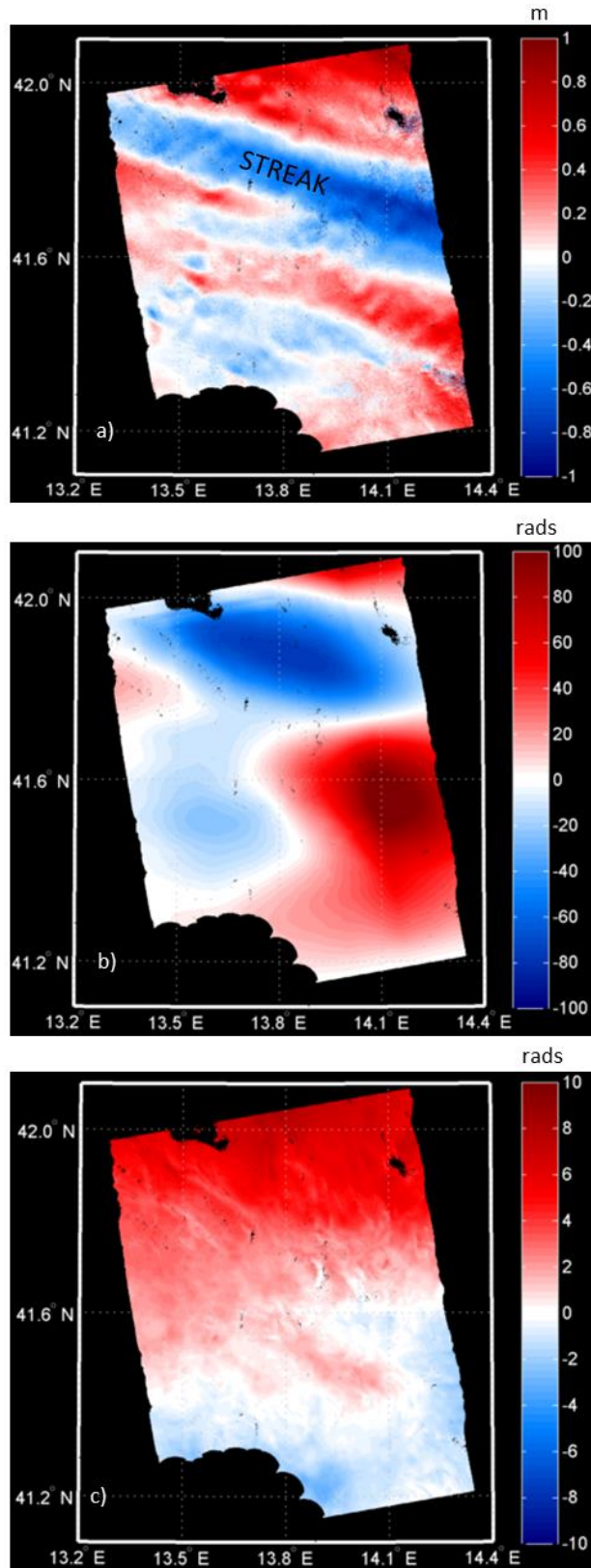Fig. 6-17 Azimuth shifts a), integral of the azimuth shifts b) and unwrapped phase c) obtained by using as master (July 1st, 2007) and as slave images (October 1st, 2007). The shifts are obtained by using MAI technique. Colorbar for the panel a) expresses the displacement in meters. To compare panel b) with panel c), both the integral of the azimuth shifts and the unwrapped phase are expressed in radians.
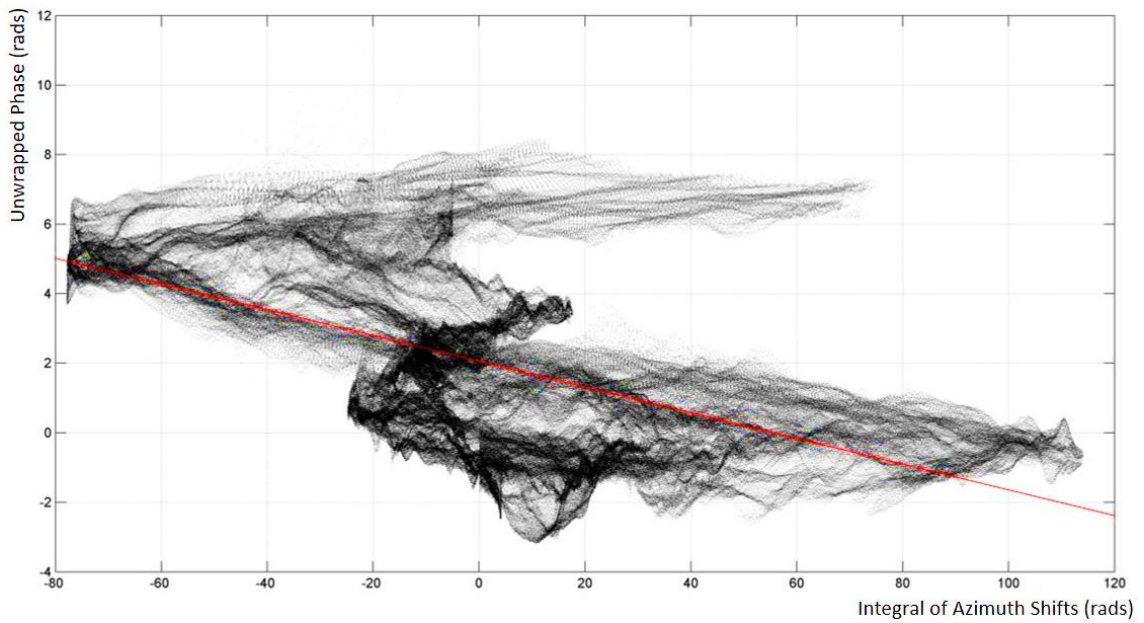
Fig. 6-18 Scatter plot of Integral of azimuth shifts vs unwrapped phase for the second case study (master: July 1st, 2007 and slave: October 1st, 2007). In red, the regression line is plotted.

6.4.2 Comparison between ΔTEC_{SAR} and ΔTEC_{GNSS}

As mentioned before, ΔTEC_{SAR} is anyway derived (Fig. 6-19). ΔTEC_{SAR} values range from about -0.2 TECu to 0.4 TECu and the map (Fig. 6-19a) is characterized by positive (red) values in the upper part of the map, null (white) and negative (blue) values from the lower boundary of the map to about 41.5°N.

In Fig. 6-19b, the corresponding ΔTEC_{GNSS} map is shown. This map is characterized by negative values except in the left upper part and in the right bottom part of the map where positive (red) values surrounded by null (white) values are present.

The ΔTEC_{GNSS} values ranging from about -0.45 to 1 TECu and, as expected, they are uncorrelated with ΔTEC_{SAR} values. In fact, the correlation coefficient, $R2$, is equal to -0.4 (Fig. 6-20).
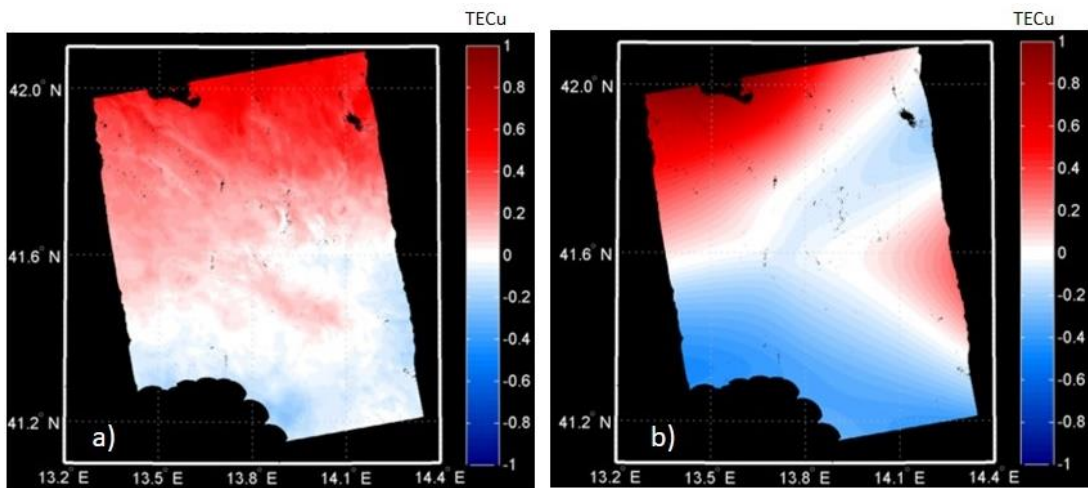
Fig. 6-19 ΔTEC_{SAR} (a) and ΔTEC_{GNSS} (b). The colorbars express, in TECu, the TEC variation between July 1st, 2007 and October 1st, 2007.
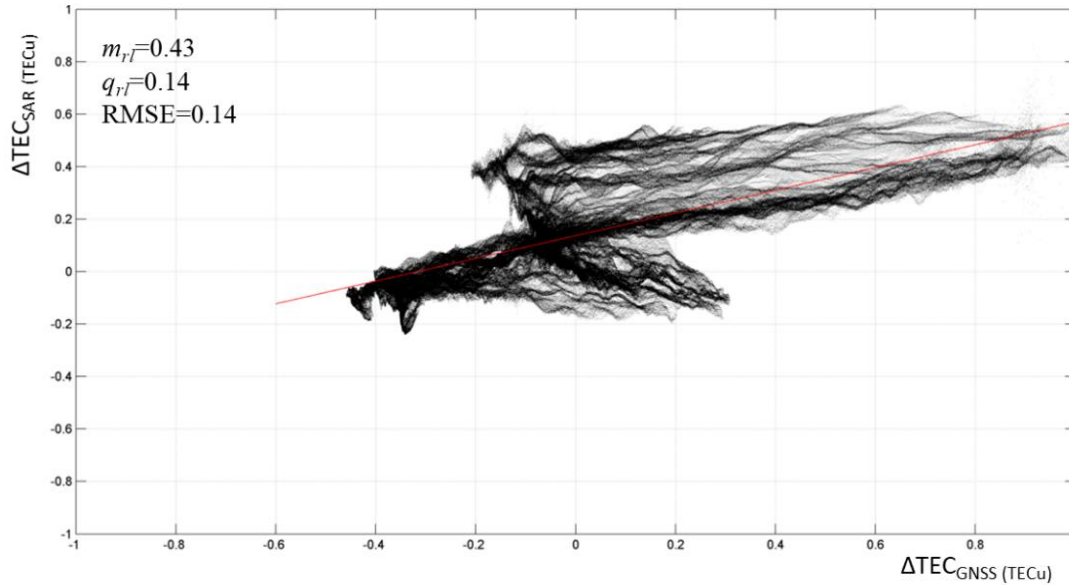

Fig. 6-20 Scatter plot of ΔTEC_{SAR} vs ΔTEC_{GNSS} for the second case study (master: July 1st, 2007 and slave: October 1st, 2007). In red, the regression line is plotted.

6.5. Case 3: 16 August 2007 – 1 October 2007

In this third case study, the master and slave images are acquired on August 16th, 2007 and on October 1st, 2007, respectively, around 21:29 UT. The condition to consider the tropospheric effect as constant over the image and the comparison between ΔTEC_{SAR} and ΔTEC_{GNSS} are investigated.

6.5.1 Approximation of constant troposphere

In this case study, the azimuth shift ranging from about -1 m to 1 m. An azimuth streaks, due to the ionosphere, can be recognized (Fig. 6-21a from about 41.6°N to 42°N (in red). This map has similar patterns (but with opposite sign) with the shifts of Fig. 6-13, except for the area ranging between 41.5°N-13.4°E and 41.3°N-14.3°E. The sign difference is because day August 16th, 2007 is used as slave in Fig. 6-13, and as a master in Fig. 6-21. As expected, above 41.7°N, the integral of the azimuth shifts of the third case study (Fig. 6-21b), shows similar pattern, but opposite in sign, with respect to the first case study (Fig. 6.*23* b). Below 41.7°N, positive (red) values are predominant except for two negative (blue) regions around 41.7°N -13.4°E and 41.6°N -14.2°E. It is noticeable a narrow region of null (white) values that surround the positives area. In this case study, the interferometric phase (Fig. 6-21c) has negative (blue) values, up to 41.8°N, null (white) values in the central part of the map, except for a positive (red) region around 14.2°E. In the bottom part of the map, positive values are present. The correlation coefficient between the integral of the azimuth shifts and the interferometric phase is *R1*=-0.6 (Fig. 6.28). As in the first case event (section 6.3), a deviation from the ideal case (|*R1*|=*1*) is found. Taking into account what already written about such deviation, ΔTEC_{SAR}, is then retrieved from the interferometric phase by applying equation 5-4.

6.5.2 Comparison between ΔTEC_{SAR} and ΔTEC_{GNSS}

Map of ΔTEC_{SAR} values (Fig. 6-23a) is obtained from the unwrapped phase (shown in Fig. 6-21Fig. 6-23c). This map shows negative (blue) values, up to 41.8°N, null (white) values in the central part of the map, except for a positive (red) region around 14.2°E. In the bottom part of the map, positive values are present.

Similarly, ΔTEC_{GNSS} map (Fig. 6-23b) shows negative (blue) values in the upper part, null (white) values in the central part and positive (red) values in the lower part of the map. The correlation coefficient between these two maps is *R2*=0.8 and the corresponding scatter plot is shown in Fig. 6-24. From this plot, it is possible to note that the ΔTEC_{SAR} values are lower than ΔTEC_{GNSS}. This two independent maps are quite well correlated (*R2*=0.8) and ΔTEC_{SAR} values are about 0.24 (m) times ΔTEC_{GNSS} values ±0.06 TECu. (*RMSE*).
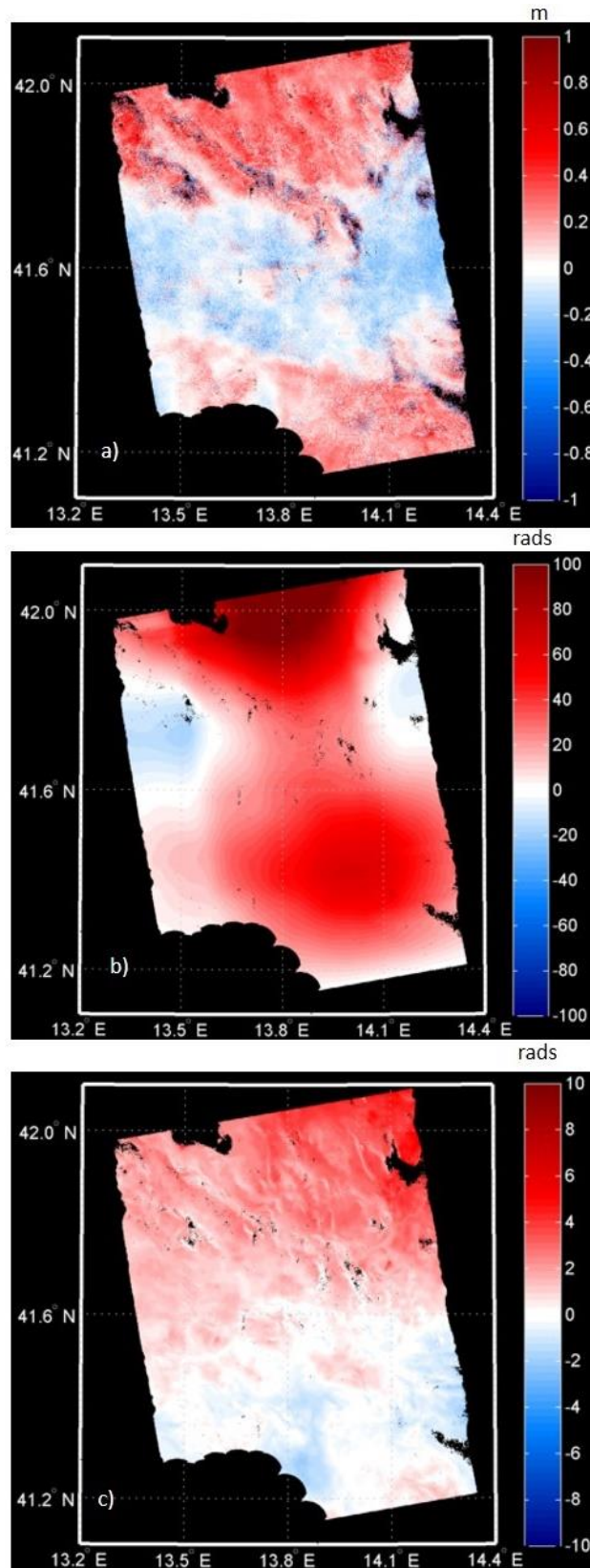
Fig. 6-21 Azimuth shifts a), integral of the azimuth shifts b) and unwrapped phase c) obtained by using as master (August 16th, 2007) and as slave images (October 1st, 2007). The shifts are obtained by using MAI technique. Colorbar for the panel a) expresses the displacement in meters. To compare panel b) with panel c), both the integral of the azimuth shifts and the unwrapped phase are expressed in radians.
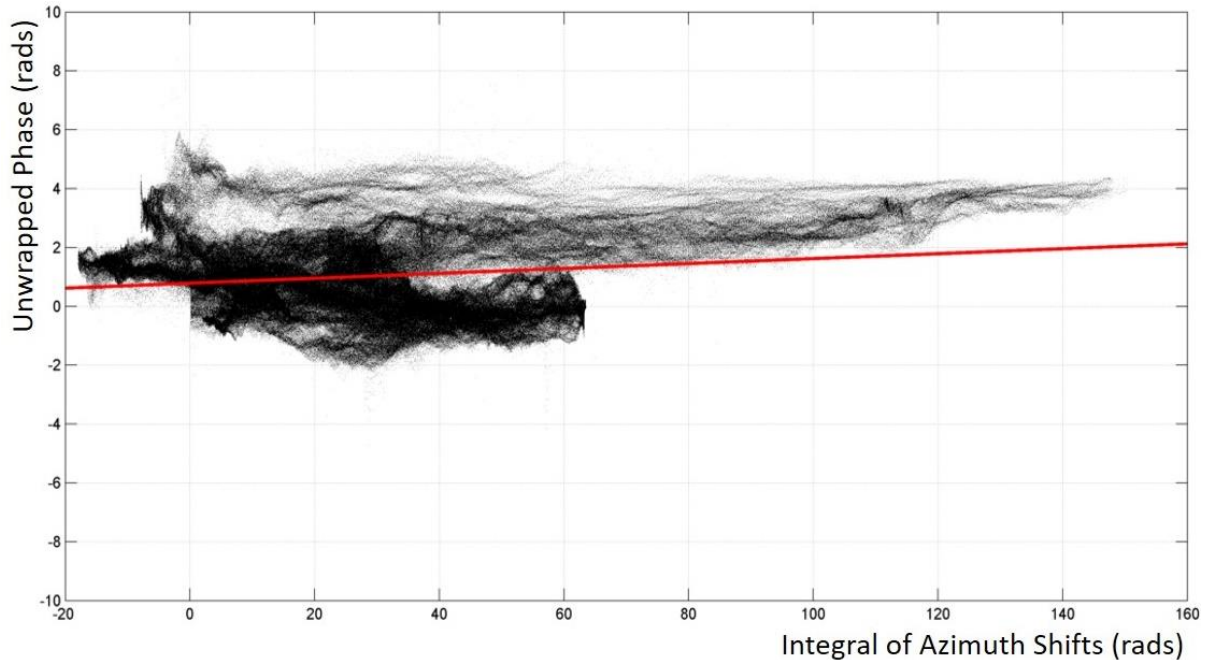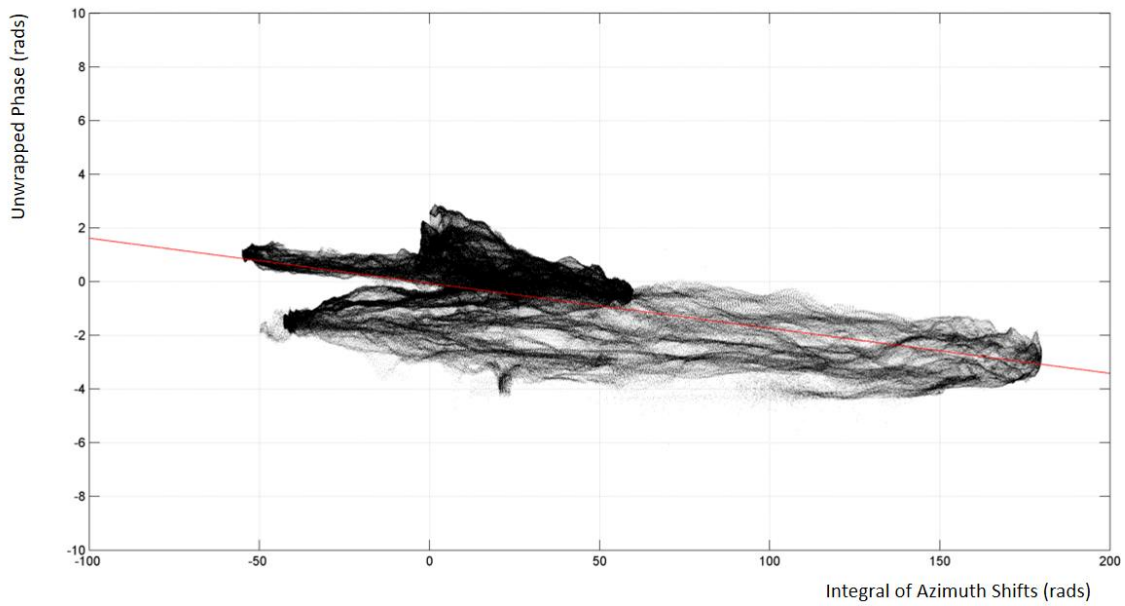
Fig. 6-22 Scatter plot of Integral of azimuth shifts vs unwrapped phase for the third case study (master: August 16th, 2007 and slave: October 1st, 2007). In red, the regression line is plotted.
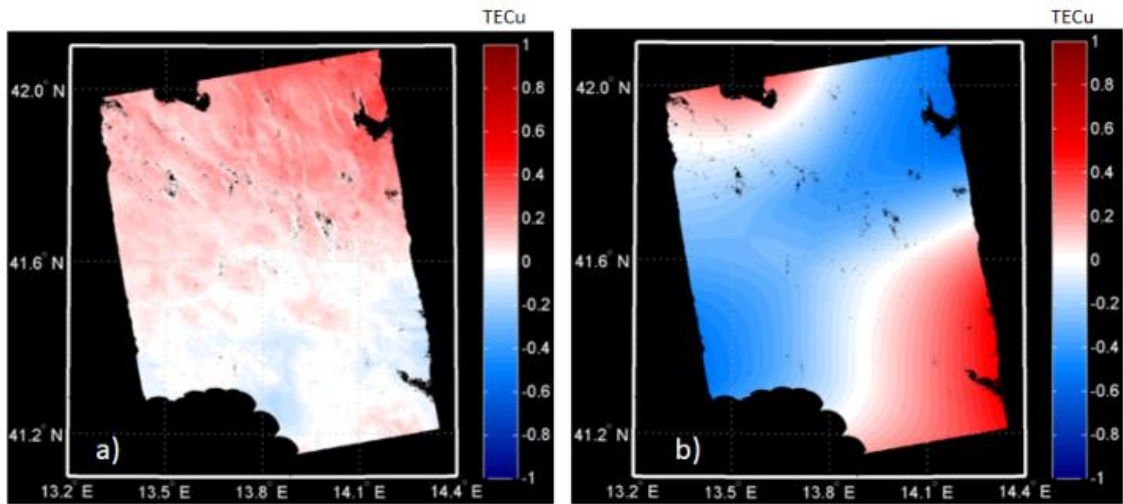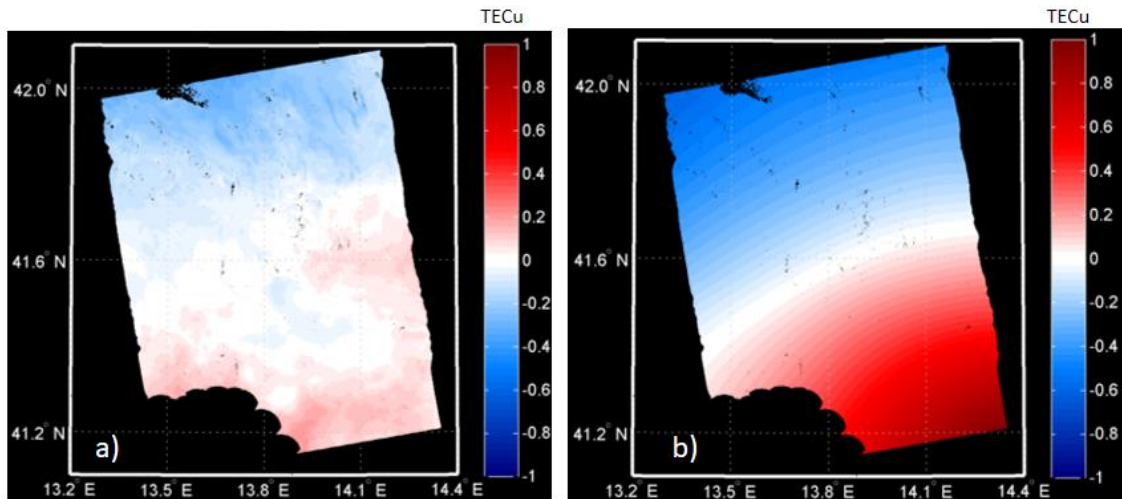

Fig. 6-23 ΔTEC_{SAR} (a) and ΔTEC_{GNSS} (b). The colorbars express, in TECu, the TEC variation between August 16th, 2007 and October 1st, 2007.
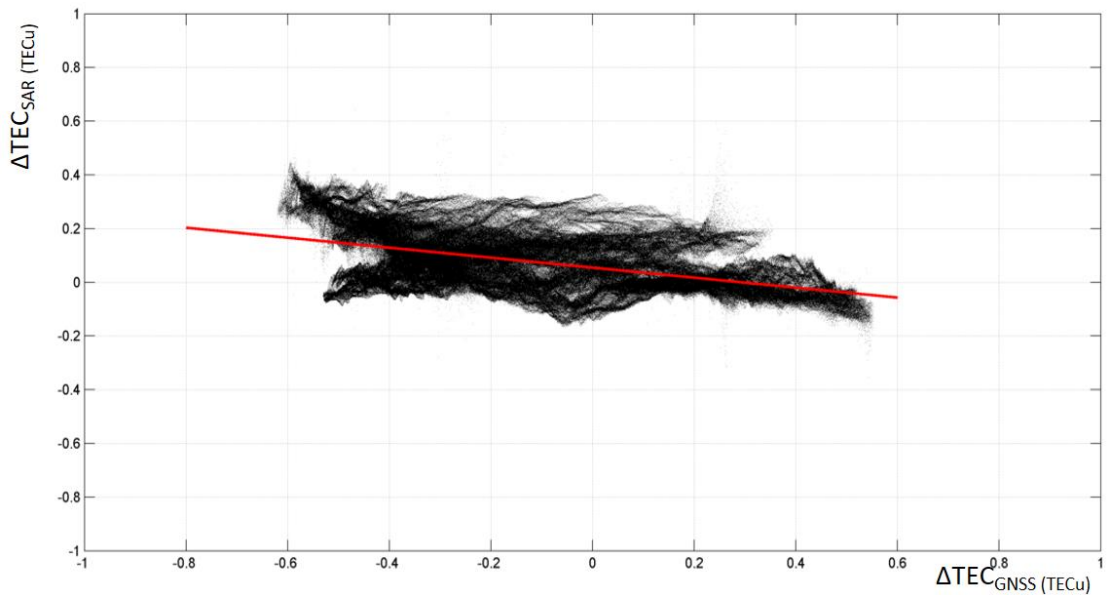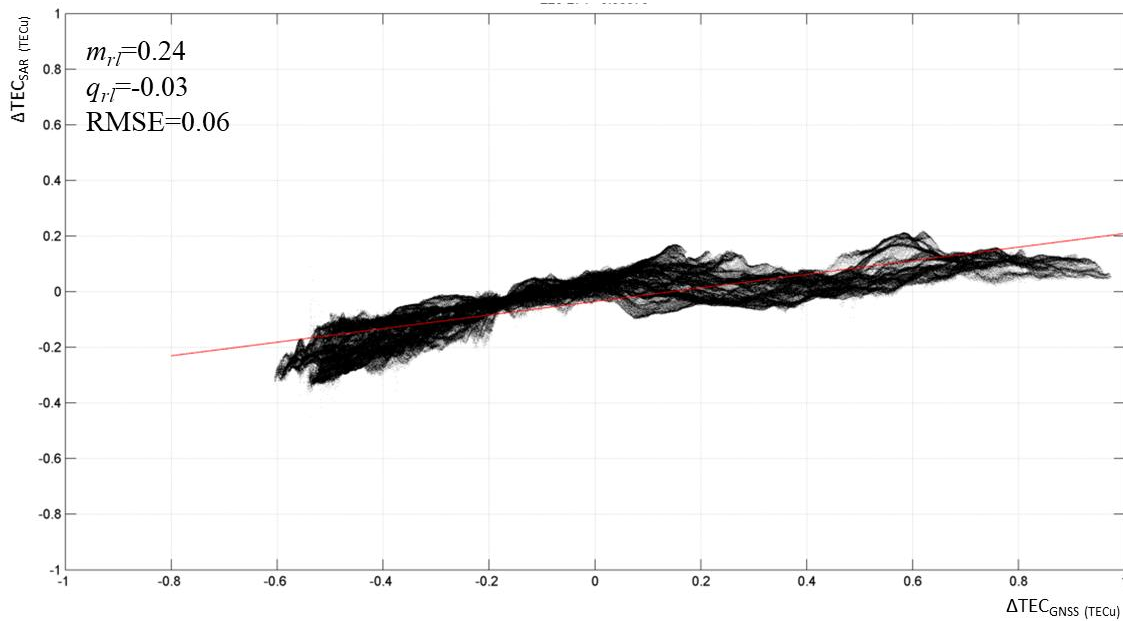
Fig. 6-24 Scatter plot of ΔTEC_{SAR} vs ΔTEC_{GNSS} for the third case study (master: August 16th, 2007 and slave: October 1st, 2007). In red, the regression line is plotted. Its angular coefficient, m_{rl}, and its intercept q_{rl} are also shown together with the *RMSE*.

6.6. Case 4: 8 April 2010 – 24 May 2010

In this fourth case study, the master and slave images are acquired on April 8th, 2010 and on May 24th, 2010, respectively, around 21:29 UT. In the next sections, the condition to consider the tropospheric effect as constant over the image and the comparison between ΔTEC_{SAR} and ΔTEC_{GNSS} are investigated.

6.6.1 Approximation of constant troposphere

In this case study, the azimuth shifts range from about -0.4 m to 0.4 m. The georeferenced results of the azimuth shifts, reported in Fig. 6-25a, shows an azimuth streak characterized by weak intensity /from about 41.8°N, 13.3 °E to 41.4°N, 14.3°E).
The integral of the azimuth shifts in this case study (Fig. 6-25b) is characterized by null (white) values except for:
- negative (blue) narrow regions in the central part and in the left bottom side of the map;
- positive (red) narrow regions in the left and right upper side and in the right bottom side of the map.

The corresponding unwrapped phase map (Fig. 6-25, panel c) is characterized mostly by negative (blue) values except in the area below 41.8°N from 13.8°E to 14.3°E where positive (red) and null (white) values are present.

61

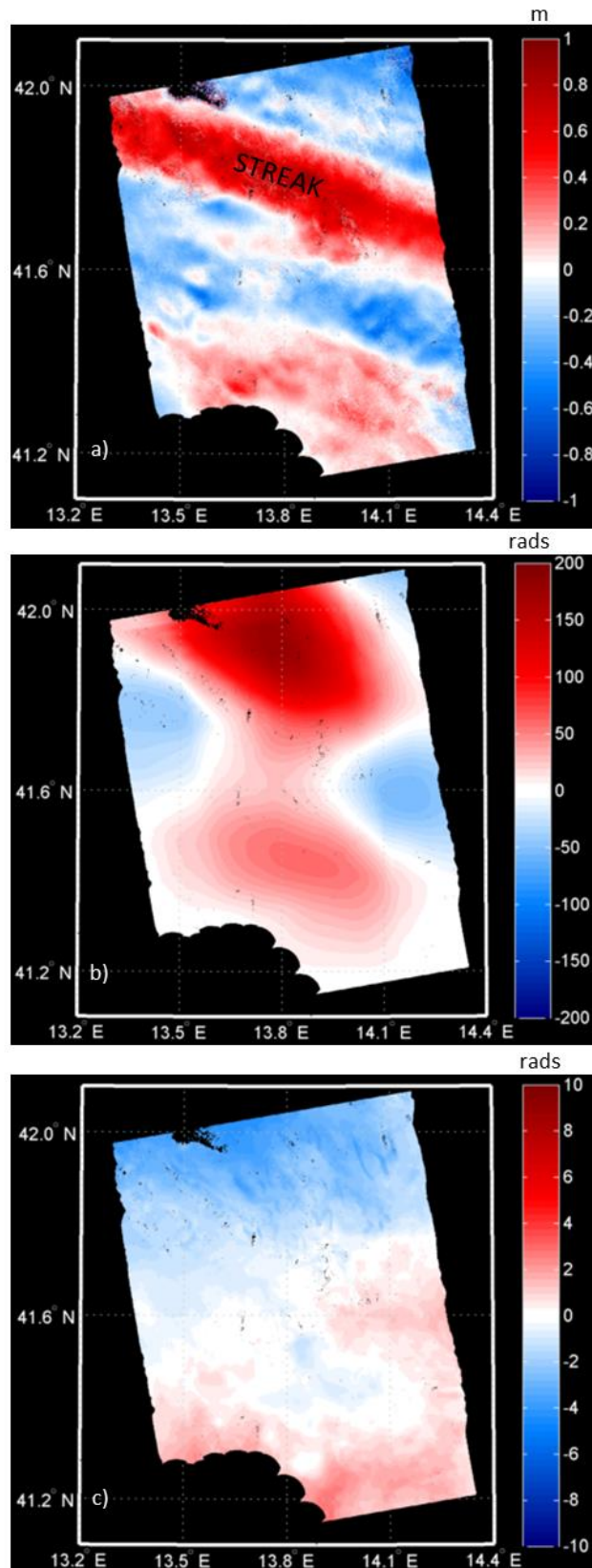Fig. 6-25 Azimuth shifts a), integral of the azimuth shifts b) and unwrapped phase c) obtained by using as master (April 8th, 2010) and as slave images (May 24th, 2010). The shifts are obtained by using MAI technique. Colorbar for the panel a) expresses the displacement in meters. To compare panel b) with panel c), both the integral of the azimuth shifts and the unwrapped phase are expressed in radians.

The correlation coefficient, between integral of the azimuth shifts and the unwrapped phase, is R1= -0.1 (Fig. 6 24), which means that the tropospheric effect cannot be considered as constant over the image, even if streaking is present. As in the second case event, ΔTEC_{SAR} cannot be extracted from the interferogram. For a confirmation, the correlation between ΔTEC_{SAR} and ΔTEC_{GNSS} is anyway calculated.

Fig. 6-26 Scatter plot of Integral of azimuth shifts vs unwrapped phase for the fourth case study (master: April 8th, 2010 and slave: May 24th, 2010). In red, the regression line is plotted.

6.6.2 Comparison between ΔTEC_{SAR} and ΔTEC_{GNSS}

ΔTEC_{SAR} map (Fig. 6-27) is characterized by negative values (blue), except in the area below 41.8°N from 13.8°E to 14.3°E where positive (red) and null (white) values are present.

ΔTEC_{GNSS} values range between -1 to 0.4 TECu (Fig. 6-27). Positive (red) values are in a narrow region between 41.7°N, 13.3°E and 41.3°N, 13.7°. Negative (blue) values are in the upper and lower part of the map. Null (white) are in the central part of the map.

From the scatter plot shown in Fig. 6-28 it is possible to confirm that no correlation (R2=0.2) between ΔTEC_{SAR} and ΔTEC_{GNSS} stands.

Fig. 6-27 ΔTEC$_{SAR}$ (a) and ΔTEC$_{GNSS}$ (b). The colorbars express, in TECu, the TEC variation between April 8th, 2010 and May 24th, 2010.
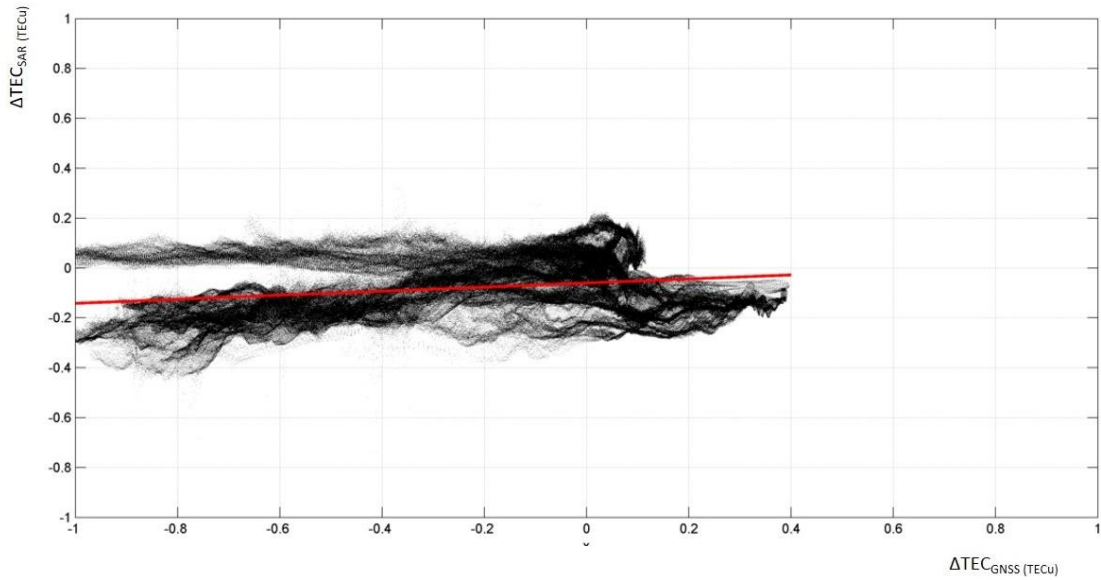
Fig. 6-28 Scatter plot of ΔTEC$_{SAR}$ vs ΔTEC$_{GNSS}$ for the fourth case study (master: April 8th, 2010 and slave: May 24th, 2010). In red, the regression line is plotted.

6.7. Case 5: 24 May 2010 – 9 July 2010

In this last case study, the master and slave images are acquired on May 24th, 2010 and on July 9th, 2010, respectively, around 21:29 UT. The correlation between the integral of the azimuth shifts and the interferometric phase is investigated to test if the tropospheric effect can be assumed as constant over the image. The correlation between ΔTEC_{SAR} and ΔTEC_{GNSS} is then investigated.

6.7.1 Approximation of constant troposphere

In this case study, the azimuth shifts range from about -0.6 m to 0.6 m (Fig. 6-29a). ae positive (red) azimuth streak, can be recognized from about 41.4°N,14.3°E to 41.8°N, 13.3°E. Negative (blue) values are predominant in the others parts of the map. The integral of the azimuth shifts in this case study (Fig. 6-29 b) is characterized by negative (blue) values in the right part of the map and by positive (red) and null (white) values in the remaining parts of the map.

The corresponding unwrapped phase map (Fig. 6-29c) is characterized by negative (blue) values in the lower and in the right central part of the map.

The correlation coefficient, between integral of the azimuth shifts and the unwrapped phase, is *R1*=-0.3 (Fig. 6-30), which means that the tropospheric effect cannot be considered as constant over the image. Also in this case, ΔTEC_{SAR} could not be extracted from the interferogram but correlation between ΔTEC_{SAR} and ΔTEC_{GNSS} is calculated for a further confirmation.

6.7.2 Comparison between ΔTEC_{SAR} and ΔTEC_{GNSS}

ΔTEC_{SAR} map (Fig. 6-31a) is characterized by negative (blue) values in the lower and in the right central part of the map.

ΔTEC_{GNSS} values (Fig. 6-31b) ranging between -0.4 to 1 TECu. ΔTEC_{GNSS} map is principally null except in the lower and upper part, where it is positive (red). A narrow region of negative (blue) values is present in left central part of the map.

The scatter plot (Fig. 6-32) shows that, as expected, there is no correlation (*R2*=-0.5) between ΔTEC_{SAR} and ΔTEC_{GNSS}.
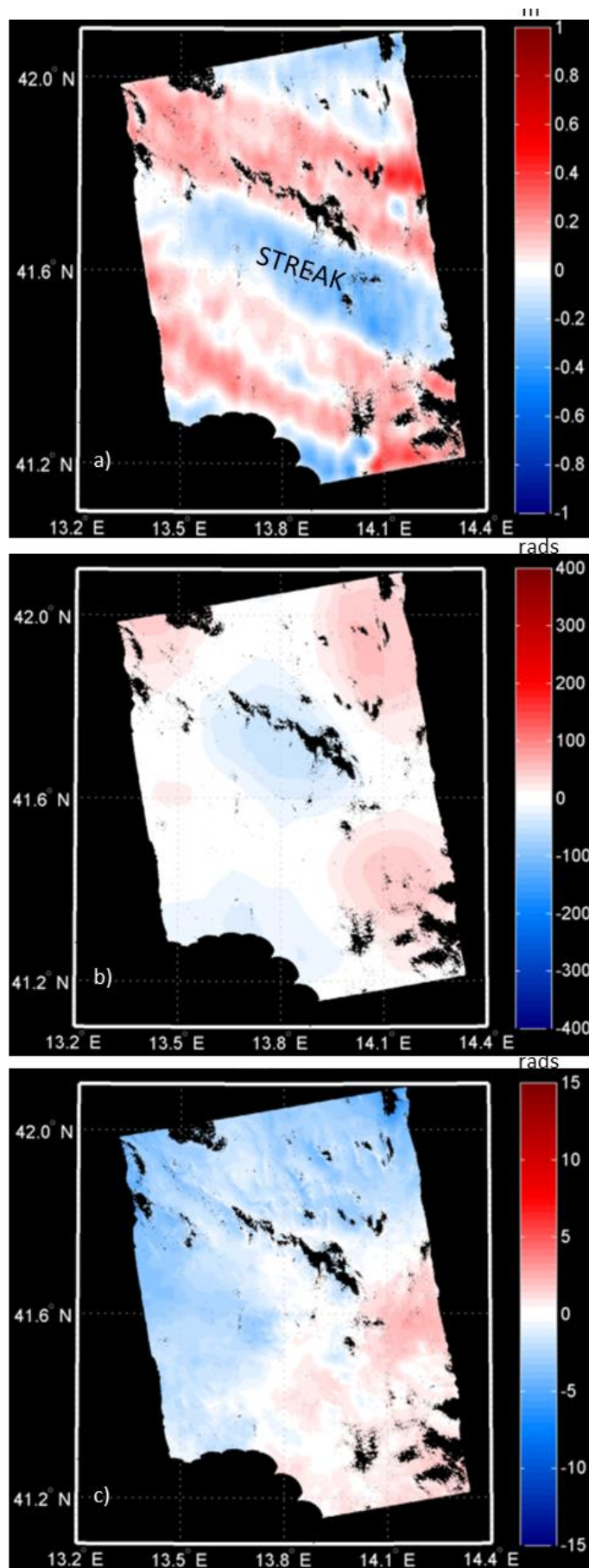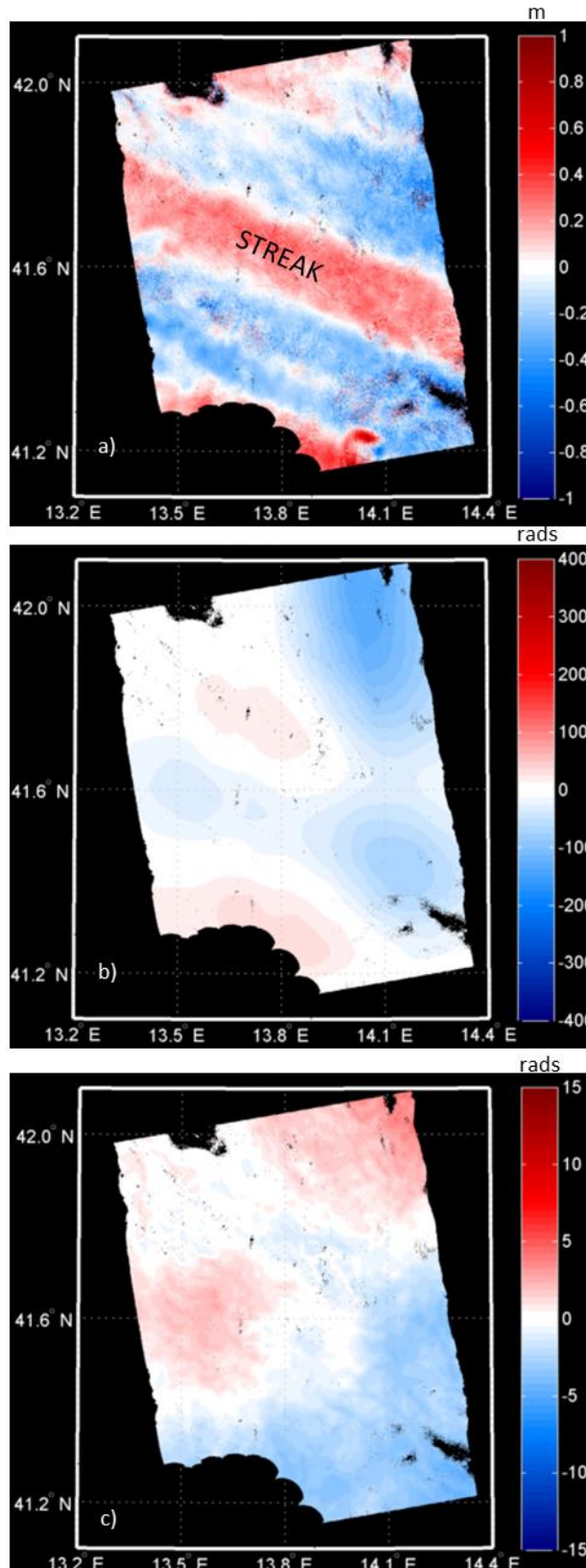
Fig. 6-29 Azimuth shifts a), integral of the azimuth shifts b) and unwrapped phase c) obtained by using as master (May 24th, 2010) and as slave images (July 9th, 2010). The shifts are obtained by using MAI technique. Colorbar for the panel a) expresses the displacement in meters. To compare panel b) with panel c), both the integral of the azimuth shifts and the unwrapped phase are expressed in radians.
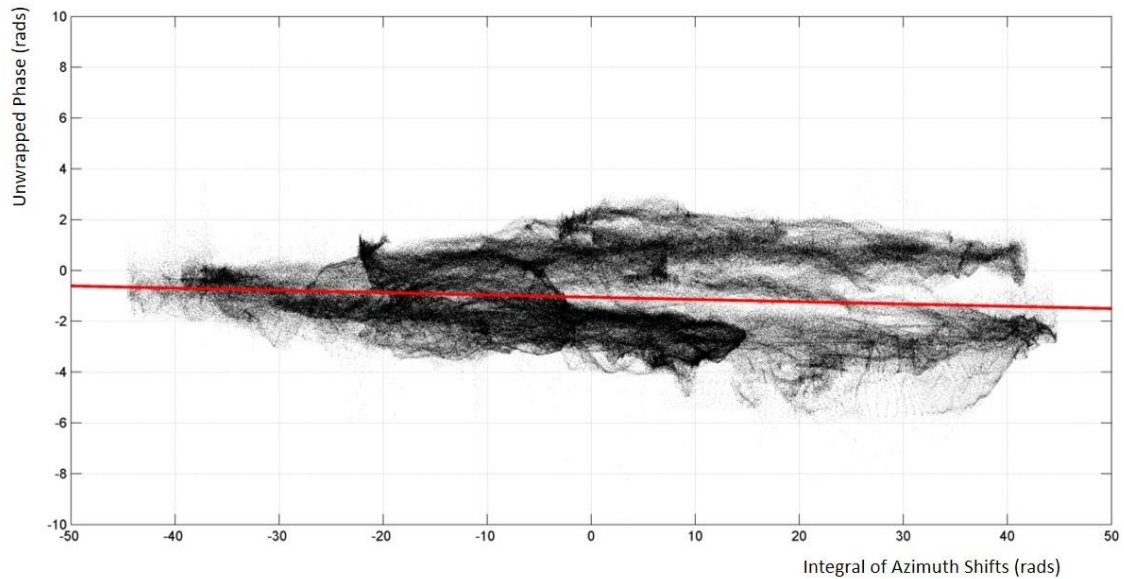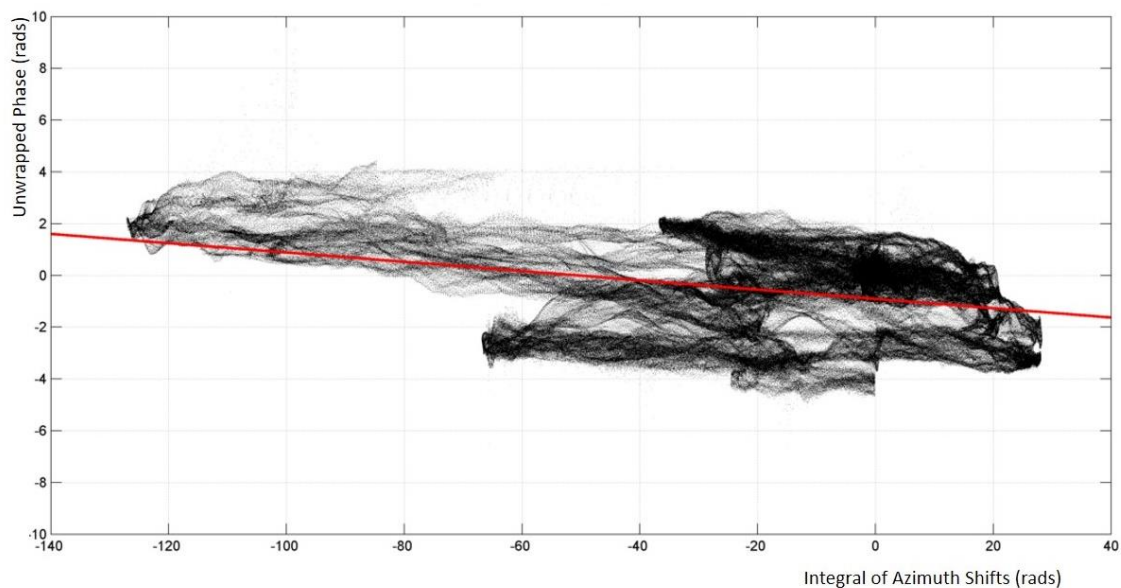
Fig. 6-30 Scatter plot of Integral of azimuth shifts vs unwrapped phase for the fifth case study (master: May 24th, 2010 and slave: July 9th, 2010). In red, the regression line is plotted.
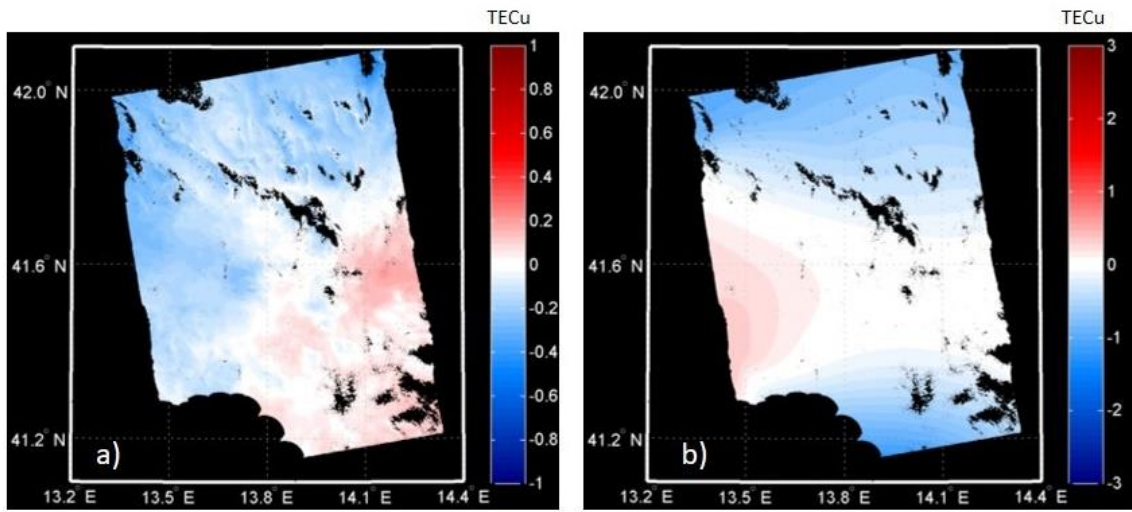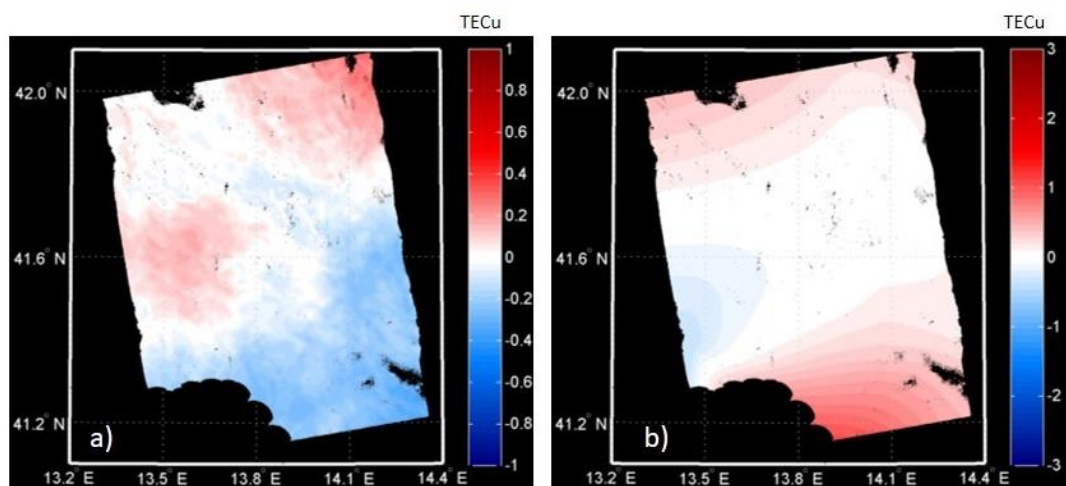

Fig. 6-31 ΔTEC_{SAR} (a) and ΔTEC_{GNSS} (b). The colorbars express, in TECu, the TEC variation between May 24th, 2010 and July 9th, 2010.
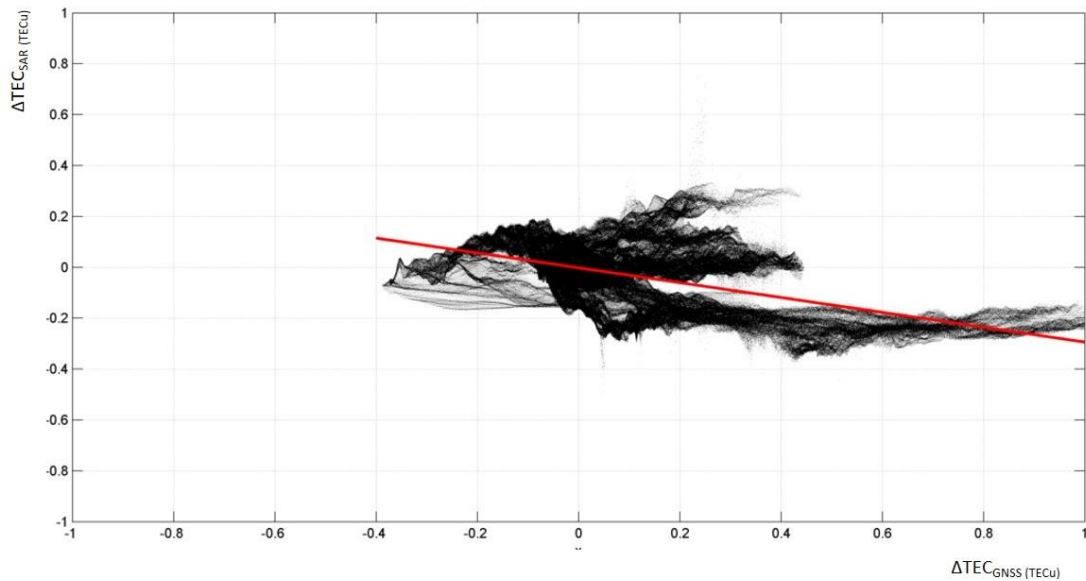
Fig. 6-32 Scatter plot of ΔTEC_{SAR} vs ΔTEC_{GNSS} for the fifth case study (master: May 24th, 2010 and slave: July 9th, 2010). In red, the regression line is plotted.

6.8. Summary

In this thesis, five case studies are analysed as listed in Table 5-1. For each case study, the characterization of the geomagnetic and ionospheric conditions are reported to assess the state of the ionosphere over the area of interest and the link with perturbing phenomena from the geospace (sections 6.1 and 6.2). A summary of the ionospheric and geomagnetic conditions plus the simultaneous occurrence of strikes on the azimuth shift maps (panel a of Fig. 6-13, Fig. 6-17, Fig. 6-21, Fig 6-25 and Fig 6-29), is reported in Table 6-1. Five days are found to be geomagnetically quiet (highlighted in green) and one day (April 8th, 2010) is along the recovery phase of a magnetic storm (highlighted in orange). In five days, an *Es* occurs during the ALOS passages with different critical frequency. It is noticeable that, when *foEs* is equal to 5 MHz or 8 MHz, the streaking effect is present on the azimuth shift images. The role of Es layer in becoming effective in creating ionospheric irregularities affecting L-band signals has been highlighted by [53]. The authors found that when Es is "dense" (not patchy) and when its critical frequency becomes larger than 4 MHz, Es might lead to scintillation effects (i.e. phase and amplitude fluctuations of the satellite received signal at ground), accompanying ionospheric irregularities. Very clear InSAR image of ionospheric plasma patches associated with daytime midlatitude Es has been described in [67] and [68]: in those works the Es frequencies (16-24 MHz) are larger than those of this thesis (5-8 MHz), for which weaker effects are found, as expected.

To check if the tropospheric phase is constant over the image, the integral of Δx (panel b, Fig. 6-13, Fig. 6-17, Fig. 6-21, Fig 6-25 and Fig. 6-29) is compared with the interferometric phase $\Delta\varphi$ (panel c ,Fig. 6-13, Fig. 6-17, Fig. 6-21, Fig 6-25 and Fig. 6-29). This is meaningful only in absence of significant movements of the ground or heavy rain events (as in these selected cases). Under such conditions, the tropospheric effect can be considered as constant if correlation between $\Delta\varphi$ and Δx stands, allowing then ΔTEC_{SAR} to be retrieved from the interferometric (eq. 5-1 and 4-7). Such condition is verified in 2 out of 5 of the analysed events. However, ΔTEC_{SAR} has been calculated for all the 5 events to

check for the correctness of the method (panel a of Fig. 6-15, Fig. 6-19 Fig. 6-23, Fig. 6-27 and Fig. 6-31).

Table 6-1. Summary of the geomagnetic and ionospheric conditions during the considered periods and their effects on the selected case studies.

Case #	Master/slave	Geomagnetic level	Es occurrence/ $foEs$	Streaks occurrence Y=yes N=no
1	July 1st, 2007		3MHz	Y
	August 16th, 2007		5 MHz	
2	July 1st, 2007		3 MHz	N
	October 1st, 2007		--	
3	August 16th, 2007		5 MHz	Y
	October 1st, 2007		--	
4	April 8th, 2010		3 MHz	Y
	May 24th, 2010		8 MHz	
5	May 24th, 2010		8 MHz	Y
	July 9th, 2010		2.2 MHz	

The "true" TEC is assumed to be the TEC from the dual frequencies GNSS receivers data, i.e. ΔTEC_{GNSS} (panel b of Fig. 6-15, Fig. 6-19 Fig. 6-23, Fig. 6-27 and Fig. 6-31). TEC values are calculated by using the RING network and by considering a time window of 5 minutes centred on the times of the ALOS passages (master and slave).

The last step of the analysis is the calculation of both the linear fit between ΔTEC_{SAR} and ΔTEC_{GNSS} and the corresponding Pearson's coefficient $R2$ (Fig. 6-16, Fig. 6-20, Fig. 6-24, Fig. 6-28 and Fig. 6-32). As already mentioned, in two cases the linear fit is quite satisfactory (Case#1 and Case#3). The corresponding values of the angular coefficient m_{rl}, of the intercept q_{rl} and of the $RMSE$ fit are summarized in Table 6-2.

Table 6-2: Case studies in which the tropospheric effect can be consider constant and the corresponding values of the angular coefficient m, of the intercept q and of the $RMSE$.

Event	Acquisition time master	Acquisition time slave	R2	m_{rl}	q_{rl} (TECu)	$RMSE$ (TECu)
Case #1	01/07/2007	16/08/2007	0.7	0.43	0.14	0.14
Case #3	16/08/2007	01/10/2007	0.8	0.24	-0.03	0.06

In both Case#1 and Case#3, ΔTEC_{SAR} is found to be lower with respect to ΔTEC_{GNSS}. Such underestimation is probably due to the plasmaspheric contribution captured from GNSS receivers at ground but no from ALOS satellite, as its orbit is at around 700 km. Yizengawa et al. [69] estimated the relative contribution of the plasmaspheric electron content to the ground based GPS TEC by using two independent observations: the TEC from ground based GPS receivers and from GPS on board of JASON-1 Satellite (satellite orbit about

1300 km). The result shown that the plasmaspheric contribution to TEC is of the order of 30% at mid-latitude during nighttime. This percentage is in agreement with the result of this thesis, for which in Case#1 and 3, ΔTEC_{GNSS} is, on the average, greater than ΔTEC_{SAR} of about 43% and 24%, respectively (Table 6-2, m_{rl} values).

To quantify the method capability in deriving ΔTEC from InSAR, ΔTEC_{SAR} for the five cases is however extracted (even when the troposphere cannot be considered as constant) and correlation between ΔTEC_{SAR} and ΔTEC_{GNSS} is evaluated. Fig. 6-33 shows the scatter plot between the Pearson's coefficients $R1$ (Δx vs. $\Delta \varphi$) and $R2$ (ΔTEC_{SAR} vs. ΔTEC_{GNSS}). Such plot clearly shows that R2 and R1 are linearly dependent with a correlation coefficient of 0.9, meaning that the assumption on Δx and $\Delta \varphi$ correlation (Section 5.1) is sufficient to allow the ΔTEC_{SAR} evaluation.
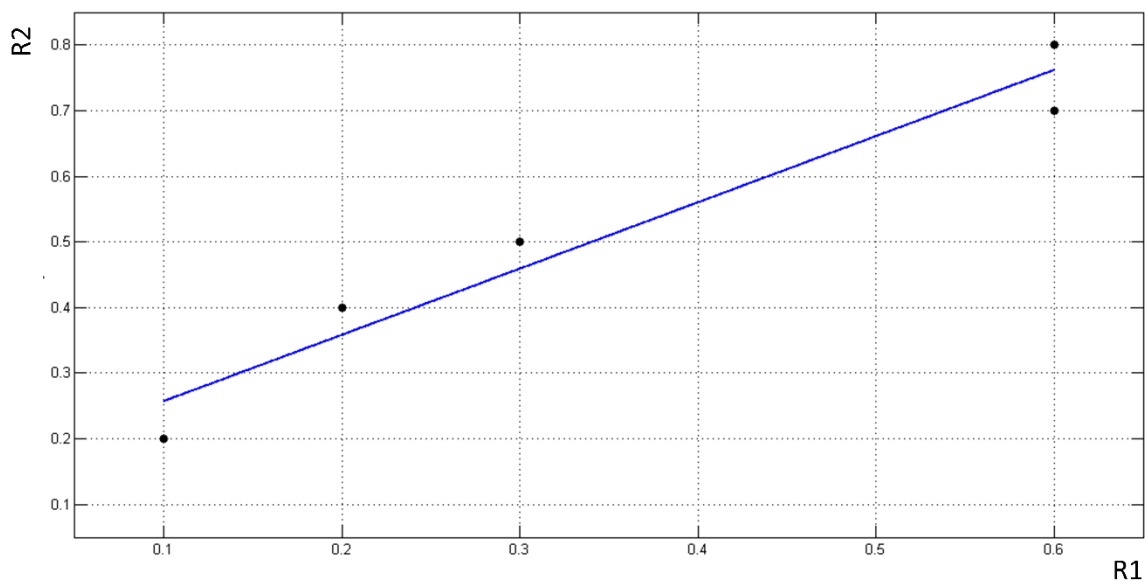
Fig. 6-33 Correlation between integral of azimuth shifts and unwrapped phase vs correlation between ΔTEC_{SAR} and $\Delta TEC_{GNSS.}$

6.9. Mitigation of the ionospheric effect in InSAR image.

As a concluding part of this thesis, a preliminary attempt at mitigating the ionospheric effect on InSAR imaging is provided, by leveraging on the method here proposed and testing it on the case events in which the tropospheric effect can be assumed as constant. It is worth noticing that an assessment based on a larger statistics is necessary, but this first results show that the proposed method can be useful to develop future mitigation techniques. The parameters of the regression lines of Case#1 and Case#3 and the measured values of ΔTEC_{GNSS} are used to derive a "mean correction value" ΔTEC_{corr}:

$$\Delta TEC_{corr} = \overline{m_{rl}} \cdot \Delta TEC_{GNSS} + \overline{q_{rl}} \pm RMSE_{Case\#1} \qquad 6\text{-}1$$

70

where $\overline{m_{rl}} = 0.33$ and $\overline{q_{rl}} = 0.05$ TECu are the averages of the m_{rl} and q_{rl} of the two case studies, respectively, and $RMSE_{Case\#1}$ is the $RMSE$ of the first case study. The ΔTEC_{corr} is then transformed into phase by considering equation 4-7 and used in equation 5-1 to obtain the corrected interferometric phase. Fig. 6-34a shows the interferometric phase of Case#1 after the application of the ionospheric correction. This map is characterized by positive values except for small areas in which blue and null values are present. The standard deviation of the interferometric phase after the correction is about 25% smaller of the non-mitigated phase. Fig. 6-34b shows the interferometric phase of Case#3 after the application of the ionospheric correction. This map is characterized by positive values in the central part of the map and negative values at the northern and southern boundaries. Also in this case the standard deviation results smaller (36%) than if no mitigation is applied. The standard deviations before and after the correction are reported in Table 6-3 together with the percentage changes. A perfectly corrected image should have a lower standard deviation, ideally reflecting only the random noise of InSAR measurement in absence of movements of the terrain and/or heavy rain [70]. Here, in the real case, the result demonstrates the goodness of the approach to mitigate the phase advance on InSAR images.
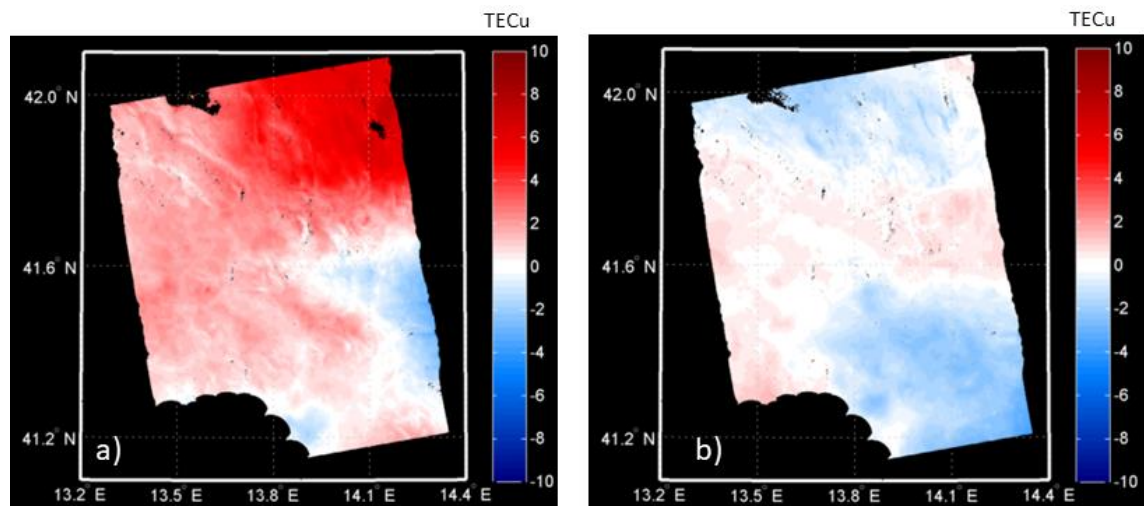
Fig. 6-34 Interferometric phase after the application of the ionospheric correction for Case#1 (a) and Case#3 (b).

Table 6-3: Summary of the standard deviations obtained before and after applying the ionospheric corrections and its percentage variations.

	$\Delta\varphi$ standard deviation (rads)	$\Delta\varphi$ standard deviation after ionospheric correction (rads)	standard deviation variation %
Case #1	2.56	1.93	-24.74%
Case #3	1.45	0.93	-35.73%

6.10. A time range of 5 minute is the best choice to freeze the ionosphere?

To verify how ΔTEC_{GNSS} map is sensible to the selection of different time intervals in which consider the ionosphere frozen and how the comparison with ΔTEC_{SAR} changes accordingly, three more time intervals around each passage of ALOS have been also investigated: 2, 10 and 15 minutes. Thus, maps of ΔTEC_{GNSS} are produced by considering TEC data in the intervals of 2, 5, 10 and 15 minutes around the two passages of ALOS. In Fig. 6-35, the correlation coefficients between ΔTEC_{SAR} and ΔTEC_{GNSS} for the different "freezing" times (time intervals in which the ionosphere is considered "frozen") and for all five cases are summarized. In the figure, the dimension of each point is proportional to the value of $R1$: the larger the value of $R1$, the larger the size of the point. The best correlation is obtained by comparing ΔTEC_{SAR} and ΔTEC_{GNSS} of Case#3 (magenta dots) when a "freezing" times of two minutes is considered. However, the correlation is almost the same considering a "freezing time" of 2, 5, and 10 minutes. The correlation significantly worsens considering the 15 minutes' interval in all cases except for the fourth one (black dots), where the worst correlation is obtained considering a "freezing" time of 10 minutes.

In Case#1 (red dots), the best correlation is obtained considering a "freezing" time of 10 minutes but if an interval of 5 minutes is considered, the correlation does not change significantly. In Case#2 (blue dots) the correlation worsens as the "freezing" time increases. The trend of the correlation in the Case#5 (green dots) is the same of Case#1: the correlation increases as the "freezing" time increases until to reach a peak at 10 minutes, then it decreases.

In conclusion, 5 minutes is a reasonable value for most the cases and only small differences among 2, 5 and 10 minutes are found in the successful Cases (#1 and #3). Fifteen minutes are found in all case to significantly violate the frozen ionosphere approximation.
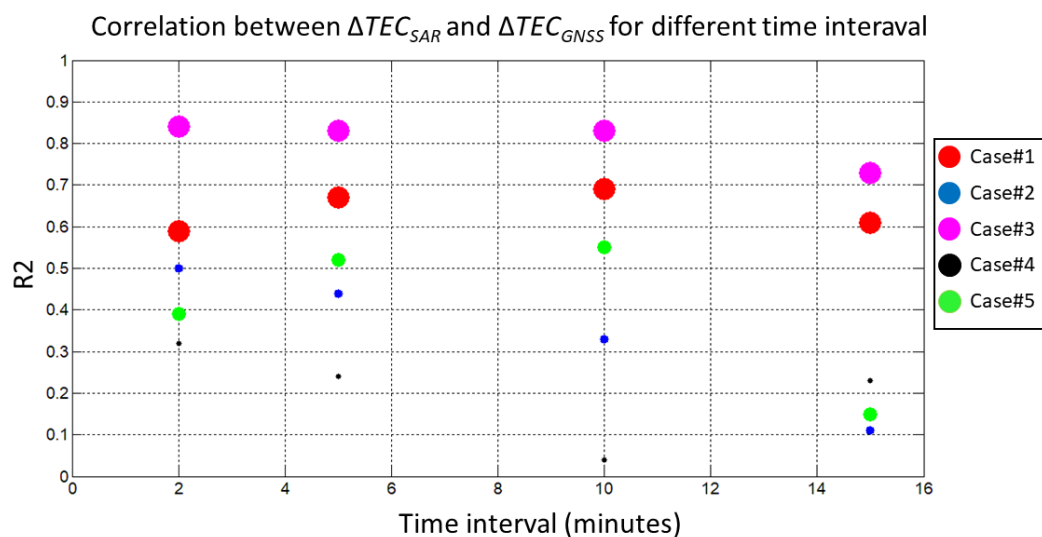

Fig. 6-35 Correlation between ΔTEC_{SAR} and ΔTEC_{GNSS} ($R2$) for different time intervals. The dimension of the points depends on the value of $R1$.

7 CONCLUSIONS

This thesis focuses on the retrieval of the ionospheric information from InSAR and on the comparison of such information with that one derived from GNSS-based technique. Measurements from InSAR are used to derive high spatial resolution ($8.33° \cdot 10^{-4}$ latitude x $8.33° \cdot 10^{-4}$ longitude) ΔTEC values that are compared with the corresponding ΔTEC values from a regional GNSS networks, considered as the reference "true" ionosphere. The results of this investigation highlight i) the potential of a method able to mitigate the ionospheric error on InSAR images and ii) the possibility of using the interferometric measurements to improve the ionospheric TEC evaluation.

SAR images acquired over central Italy by ALOS-PALSAR around 21:29 UT as listed in in table 1 are analysed. These images provide the basic information to investigate on five case events, deeply analysed and discussed. The characterization of the geomagnetic conditions around the ALOS passages suggests that, a part in a single case under slightly unsettled conditions, no significant geomagnetic disturbances can be responsible of streaking effects on the images. Instead, a correspondence between strikes and the occurrence of Es with $foEs \geq 5$ MHz is found (Table 6-1).

In two out of five case studies, the interferometric phase is reasonably assumed to be due to the ionosphere and the tropospheric effects can be assumed as constant. So, ΔTEC_{SAR} is derived from interferometric phase and tested against ΔTEC_{GNSS}, evaluated by assuming the ionosphere as: 1) a thin ionized layer at 350 km above the Earth's surface and 2) "frozen" within a 5-minutes' window around the SAR passages. The resulting ΔTEC_{SAR} and ΔTEC_{GNSS} maps are quite well correlated being the correlation coefficients $R2=0.7$ (Case#1) and $R2=0.8$ (Case#3), although the ΔTEC_{SAR} values are on the average underestimated of about 30% in respect to ΔTEC_{GNSS}. This difference is probably due to the plasmaspheric contribution (expected to range between 10% and 30%) in ΔTEC_{GNSS} measurement, absent in the ΔTEC_{SAR} as for the SAR orbit.

A mitigation technique for Case#1 and Case #3 is developed based on the regression line parameters between ΔTEC_{SAR} and ΔTEC_{GNSS} (formula 6-1). The results are quite encouraging showing that, after the ionospheric correction, the standard deviation of the interferometric phase decreases of about 25% for the Case#1 and of about 36% for the Case#3. Formula 6-1 not only provides the empirical mitigation of the ionospheric impact on InSAR imaging, but also relates ionospheric information as derived from the two independent measurements of the ΔTEC. This enable the possible simultaneous use of both InSAR and GNSS for ionospheric monitoring purposes.

Analysis of further case events are necessary to consolidate the outcomes from this thesis addressed to the Es effects on SAR and to the ionospheric mitigation technique. Improvements of TEC_{GNSS} is expected by using a more severe elevation angle cut off (here equal to 20°), balanced with the need of high spatial resolution maps. The limitation due to the GNSS satellite–receivers geometry will also be faced by investigating the possibility to use the slant TEC information from selected ray paths matching the SAR signals paths.

Such selection of the slant paths is expected to reduce the number of usable information from GNSS.

REFERENCES

[1] X. Zhou, N.-B. Chang e S. Li, «Applications of SAR interferometry in earth and environmental science research,» *Sensors,* vol. 9, n. 3, pp. 1876-1912, 2009.

[2] R. F. Hanssen, Radar interferometry: data interpretation and error analysis (Vol. 2), Springer Science & Business Media., 2001.

[3] M. Mendillo, «Storms in the ionosphere: Patterns and processes for total electron content,» *Reviews of Geophysics,* vol. 44, n. 4, 2006.

[4] J. Liu, Y. Kuga e A. Ishimaru, «Simulations of ionospheric effects on SAR at P-band,» *Geoscience and Remote Sensing Symposium, 1999. IGARSS'99 Proceedings. IEEE 1999 International,* vol. 3, pp. 1842-1844, 1999.

[5] A. L. Gray, K. E. Mattar e N. Short, «peckle tracking for 2-dimensional ice motion studies in polar regions,» *Proceedings of the 2nd International Workshop on ERS SAR inter] erometry" Fringe'99, Liège, Belgium,, November 10-12, ESA SP,* vol. 478, pp. 1-6, 1999.

[6] A. L. Gray, K. E. Mattar e G. Sofko, «Influence of ionospheric electron density fluctuations on satellite radar interferometry,» *Geophysical Research Letters,* vol. 27, n. 10, pp. 1451-1454, 2000.

[7] K. E. Mattar e A. L. Gray, «Reducing ionospheric electron density errors in satellite radar interferometry applications,» *Canadian Journal of Remote Sensing,* vol. 28, n. 4, pp. 593-600, 2002.

[8] J. S. Kim, A. Danklmayer e K. Papathanassiou, «Correction of ionospheric distortions in low frequency interferometric SAR data,» *Geoscience and Remote Sensing Symposium (IGARSS), 2011 IEEE International ,* pp. 1505-1508, 2011.

[9] A. C. Chen e H. A. Zebker, «Reducing ionospheric effects in InSAR data using accurate coregistration,» *EEE Transactions on Geoscience and Remote Sensing,* vol. 52, n. 1, pp. 60-70, 2014.

[10] F. Meyer, R. Bamler, N. Jakowski e T. Fritz, «The potential of low-frequency SAR systems for mapping ionospheric TEC distributions,» *IEEE Geoscience and Remote Sensing Letters,* vol. 3, n. 4, pp. 560-564, 2006.

[11] P. A. Rosen, S. Hensley e C. Chen, «Measurement and Mitigation of the Ionosphere in,» *Radar Conference, 2010 IEEE,* pp. 1459-1463, 2010.

[12] R. Brcic, A. Parizzi, M. Eineder, R. Bamler e F. Meyer, «Ionospheric effects in SAR interferometry: An analysis and comparison of methods for their estimation,» *Geoscience and Remote Sensing Symposium (IGARSS), 2011 IEEE International ,* pp. 1497-1500, 2011.

[13] G. Gomba, A. Parizzi, F. De Zan, M. Eineder e R. Bamler, «Toward Operational Compensation of Ionospheric Effects in SAR Interferograms: The Split-Spectrum Method,» *Transactions on Geoscience and Remote Sensing,* vol. 54, n. 3, pp. 1446-1461, 2016.

[14] R. Brcic, A. Parizzi, M. Eineder, R. Bamler e F. Meyer, «Estimation and compensation of ionospheric delay for SAR interferometry,» *In Geoscience and Remote Sensing Symposium (IGARSS), 2010 IEEE International,* pp. 2908-2911, 2010.

[15] Z. Liu, H.-S. Jung e Z. Lu, «Joint correction of ionosphere noise and orbital error in L-band SAR interferometry of interseismic deformation in southern California,» *IEEE Transactions on Geoscience and Remote Sensing,* vol. 52, n. 6, pp. 3421-3427, 2014.

[16] X. Pi, «Ionospheric effects on spaceborne synthetic aperture radar and a new capability of imaging the ionosphere from space,» *Space Weather,* vol. 13, n. 11, pp. 737-741, 2015.

[17] P. Dominici, «Radiopropagazione ionosferica,» *Annali di Geofisica,* vol. 2, 1971.

[18] J. K. Hargreaves, The solar-terrestrial environment: an introduction to geospace-the science of the terrestrial upper atmosphere, ionosphere, and magnetosphere, Cambridge University Press., 1992.

[19] W. Dieminger, G. K. Hartmann e R. Leitinger, The upper atmosphere: data analysis and interpretation, Springer Science & Business Media., 2012.

[20] G. Didebulidze , G. Dalakishvili, L. Lomidze e G. Matiashvili, «Formation of sporadic-E (Es) layers under the influence of AGWs evolving in a horizontal shear flow,» *Journal of Atmospheric and Solar-Terrestrial Physics,* vol. 136, p. 163–173, 2015.

[21] Handbook of Geophysics and the Space Environment. Ionospheric Radio Wave Propagation, Scientific Editor Adolph Juisa, Air Force Geophysics Laboratory, Air Force, 1985.

[22] P. M. Kintner, A. J. Coster, T. Fuller-Rowell, A. J. Mannucci, M. Mendillo e R. Heelis, «Midlatitude Ionospheric Dynamics and Disturbances: Introduction,» *Geophysical Monograph Series,* n. 181, pp. 1-7, 2008.

[23] B. N. Gershman e G. I. Grigor'ev, «Traveling ionospheric disturbances—A review,» *Radiophysics and Quantum Electronics ,* vol. 11, n. 1, pp. 1-13, 1968.

[24] J. Whitehead, «The formation of the sporadic-E layer in the temperate zones,» *Journal of Atmospheric and Terrestrial Physics,* vol. 20, pp. 48-58, 1961.

[25] M. Pietrella e C. Bianchi, «Occurrence of sporadic-E layer over the ionospheric station of Rome,» *Advances in space research,* vol. 44, pp. 72-81, 2009.

[26] J. Mathews, «Sporadic E: current views and recent progress,» *Journal qf Almospherrc and Solar-Terreslrial Physrcs,* vol. 60, n. 4, pp. 413-435, 1998.

[27] A. Pignalberi, M. Pezzopane e E. Zuccheretti, «Sporadic E layer at mid-latitudes: average properties and influence of atmospheric tides,» *Annals of Geophysics,* vol. 32, p. 1427–1440., 2014.

[28] J. Laštovička, «Observations of tides and planetary waves in the atmosphere-ionosphere system,» *Advances in Space Research,* vol. 20, n. 6, pp. 1209-1222, 1997.

[29] A. Pignalberi, M. Pezzopane e E. Zuccheretti, «A spectral study of the mid-latitude sporadic E layer characteristic oscillations comparable to those of the tidal and the planetary waves,» *Journal of Atmospheric and Solar-Terrestrial Physics,* vol. 122, pp. 34-44, 2015.

[30] G. Didebulidze e L. N. Lomidze, «Double atmospheric gravity wave frequency oscillations of sporadic E formed in a horizontal shear flow,» *Physics Letters A,* vol. 374, n. 7, p. 952–959, 2010.

[31] T. Tsuda, «Characteristics of atmospheric gravity waves observed using the MU (Middle and Upper atmosphere) radar and GPS (Global Positioning System) radio

occultation,» *Proceedings of the Japan Academy Series B, Physical and Biological Sciences,* vol. 90, n. 1, pp. 12-27, 2014.

[32] J. D. Whitehead, «Recent work on mid-latitude and equatorial sporadic-E,» *Journal of Atmospheric and Terrestrial Physics,* vol. 51, n. 5, pp. 401-424, 1989.

[33] C. Cesaroni, L. Alfonsi, M. Pezzopane, C. Martinis, J. Baumgardner, J. Wroten, M. Mendillo, E. Musicò, M. Lazzarin e G. Umbriaco, «The first use of coordinated ionospheric radio and optical observations over Italy: Convergence of high and low latitude storm-induced effects?,» *Journal of Geophysical Research: Space Physics,* vol. 122, 2017.

[34] S. H. Francis, «A theory of medium-scale traveling ionospheric disturbances,» *.Journal of Geophysical Research,* vol. 79, n. 34, pp. 5245-5260, 1974.

[35] M. Pezzopane, M. Pietrella, A. Pignalberi e R. Tozzi, «20 March 2015 solar eclipse influence on sporadic E layer,» *Advances in Space Research ,* vol. 56, p. 2064–2072, 2015.

[36] A. Saito, M. Nishimura, M. Yamamoto, S. Fukao,, M. Kubota, K. Shiokawea, Y. Otsuka, T. Tsugawa, T. Ogawa, M. Ishii, T. Sakanoi e S. Miyazaki, «Traveling ionospheric disturbances detected in the FRONT campaign,» *Geophysical research letters,* vol. 28, n. 4, pp. 689-692, 2001.

[37] G. Crowley e F. S. Rodrigues, «Characteristics of traveling ionospheric disturbances observed by the TIDDBIT sounder,» *Radio Science,* vol. 47, n. 4, 2012.

[38] A. Ferretti, A. Monti-Guarnieri, C. Prati, F. Rocca e D. Massonet, «InSAR Principles: Guidelines for SAR interferometry Processing and Interpretation,» Karen Fletcher, The Netherlands, 2007.

[39] G. Picardi, Elaborazione del segnale radar: metodologie ed applicazioni, Franco Angeli, 2000.

[40] A. Marino, A new target detector based on geometrical perturbation filters for Polarimetric Synthetic Aperture Radar (POL-SAR), Springer Science & Business Media., 2012.

[41] R. Scheiber e A. Moreira, «Coregistration of interferometric SAR images using spectral diversity,» *IEEE Transactions on Geoscience and Remote Sensing,* vol. 38, n. 5, pp. 2179-2191, 2000.

[42] N. B. D. Bechor e H. A. Zebker, «Measuring two-dimensional movements using a single InSAR pair,» *Geophysical research letters,* vol. 33, n. 16, p. L16311, 2006.

[43] P. Teunissen e O. Montenbruck, Springer handbook of global navigation satellite systems, Berlin: Springer, 2017.

[44] E. D. Kaplan e C. J. Hegarty, Understanding GPS: Principles and Applications, Artech House, 2006.

[45] J. Böhm e H. Schuh, Atmospheric Effects in Space Geodesy, Springer, Berlin, Heidelberg, 2013.

[46] U. Wegmüller, C. Werner, T. Strozzi e A. Wiesmann, «Ionospheric electron concentration effects on SAR,» in *Geoscience and Remote Sensing Symposium, IGARSS*, Denver, CO, USA, 2006.

[47] F. J. Meyer e J. Nicoll, «The impact of the ionosphere on interferometric SAR processing,» *Geoscience and Remote Sensing Symposium, 2008. IGARSS 2008. IEEE International,* vol. 2, pp. II-391 - II-394, 2008.

[48] R. M. Goldstein e C. L. Werner, «Radar interferogram filtering for geophysical applications,» *Geophysical Research Letters,* vol. 25, n. 21, pp. 4035-4038, 1998.

[49] C. L. Werner, U. Wegmüller, T. Strozzi e A. Wiesmann, «Processing strategies for phase unwrapping for INSAR applications,» in *Proceedings.EUSAR 2002*, Cologne,, 2002.

[50] A. Rosenqvist, M. Shimada e M. Watanabe, «ALOS PALSAR: Technical outline and mission concepts,» in *4th International Symposium on Retrieval of Bio-and Geophysical Parameters from SAR Data for Land Applications*, Innsbruck, Austria, 2004.

[51] C. Cesaroni, L. Spogli, L. Alfonsi, G. De Franceschi, L. Ciraolo, J. Francisco, G. Monico, C. Scotto, V. Romano, M. Aquino e B. Bougard, «L-band scintillations and calibrated total electron content gradients over Brazil during the last solar maximum,» *Journal of Space Weather and Space Climate,* vol. 5, n. A36, 2015.

[52] A. J. Mannucci, B. D. Wilson e D. N. Yuan, «A global mapping technique for GPS-derived ionospheric total electron content measurement,» *Radio science,* vol. 33, n. 3, pp. 565-582, 1998.

[53] L. Alfonsi, L. Spogli, M. Pezzopane, V. Romano, E. Zuccheretti, G. De Franceschi, M. A. Cabrera e R. G. Ezquer, «Comparative analysis of spread-F signature and GPS scintillation occurrences at Tucumán, Argentina,» *Journal of Geophysical Research: Space Physics,* vol. 118, n. 7, p. 4483–4502 , 2013.

[54] C. Bianchi, J. A. Baskaradas, M. Pezzopane, U. Sciacca e E. Zuccheretti, «Fading in the HF ionospheric channel and the role of irregularities,» *Advances in Space Research ,* vol. 52, n. 3, p. 403–411, 2013.

[55] H. Rishbeth e . O. K. Garriot, «Introduction to Ionospheric Physics,» New York, Academic Press, 1969.

[56] R. Sibson, «A brief description of natural neighbor interpolation (Chapter 2),» in *V. Barnett. Interpreting Multivariate Data*, Chichester: John Wiley, 1981, pp. 21-36.

[57] C. Cesaroni, «A multi instrumental approach to the study of equatorial ionosphere over South-America,» PhD dissertation, DIFA, Bologna, Italy, 2015b.

[58] P. Mayaud, «Derivation, meaning and use of geomagnetic indices,» in *geophysical monograph 22. America Geophysical Union*, Washington, DC, 1980.

[59] L. Perrone e G. De Franceschi, «Solar, ionospheric and geomagnetic indices,» *Annals of Geophysics,* vol. 41, n. 5-6, p. 843–855, 1998.

[60] W. Baumjohann e R. A. Treumann, Basic space plasma physics, World Scientific Publishing Company, 2012.

[61] L. R. Cander e S. J. Mihajlovic, «Ionospheric spatial and temporal variations during the 29–31 October 2003 storm,» *Journal of atmospheric and solar-terrestrial physics,* vol. 67, n. 12, pp. 1118-1128, 2005.

[62] O. Troshichev e A. Janzhura, «Relationship between the PC and AL indices during repetitive bay-like magnetic disturbances in the auroral zone,» *Journal of Atmospheric and Solar-Terrestrial Physics,* vol. 71, n. 12, pp. 1340-1352, 2009.

[63] J. A. Richards, Radio Wave Propagation: An introduction for the non-specialist, Springer Science & Business Media, 2008.

[64] I. A. Galkin e B. W. Reinisch, «The new ARTIST 5 for all digisondes,» *Ionosonde Network Advisory Group Bulletin,* vol. 69, n. 8, 2008.

[65] C. Scotto, «Electron density profile calculation technique for Autoscala ionogram analysis,» *Advances in Space Research,* vol. 44, n. 6, p. 756–766, 2009.

[66] M. Pezzopane e C. Scotto, «Automatic scaling of critical frequency foF2 and MUF (3000) F2: A comparison between Autoscala and ARTIST 4.5 on Rome data,» *Radio Science,* vol. 42, n. 4, 2007.

[67] J. Maeda e K. Heki, «Two-dimensional observations of midlatitude sporadic E irregularities with a dense GPS array in Japan,» *Radio Science,* vol. 49, n. 1, pp. 28-35, 2014.

[68] J. Maeda, T. Suzuki, M. Furuya e K. Heki, «Imaging the midlatitude sporadic E plasma patches,» *Geophysical Research Letters,* vol. 43, p. 1419–1425, 2016.

[69] E. Yizengaw, M. Moldwin, D. Galvan , B. Iijima, A. Komjathy e A. J. Mannucci, «Global plasmaspheric TEC and its relative contribution to GPS TEC,» *Journal of Atmospheric and Solar-Terrestrial Physics,* vol. 70, n. 11, pp. 1541-1548., 2008.

[70] Y. Reuveni, Y. Bock, X. Tong e A. W. Moore, «Calibrating interferometric synthetic aperture radar (InSAR) images with regional GPS network atmosphere models,» *Geophysical Journal International,* vol. 202, n. 3, pp. 2106-2119., 2015.